



POST AWARD ADMINISTRATION OFFICE

January 28, 2016

**Office of Naval Research  
Attn: Dr. Airan Perez  
875 North Randolph Street  
Arlington, VA 22203-1995**

**SUBJECT: Final Technical Report on Grant Number N00014-12-1-0506  
(UVA PTAO #140116-GG11530)**

Dear Dr. Perez,

Enclosed is the Final Technical Report under the direction of Dr. J. R. Scully on Grant Number N00014-12-1-0506. This project is entitled "Assessing Heat-to-Heat Variations Affecting Mechanism Based Modeling of Hydrogen Environment Cracking (HEAC) in High Strength Alloys for Marine Applications: Monel K-500" for the period of March 15, 2012 through December 31, 2015. If you have any questions, you may contact Dr. Scully by e-mail at [irs8d@virginia.edu](mailto:irs8d@virginia.edu) or by phone 434-982-5786. We appreciate your support under this grant.

Sincerely,

A handwritten signature in black ink, appearing to read "Sherry Fitzgerald".

**Sherry Fitzgerald  
Administrative Assistant**

Enclosure: Final Technical Report

**Cc : ONR Regional Administration Atlanta – N66020  
100 Alabama Street, SW Suite 4R15  
Atlanta, GA 30303-3104**

**Naval Research Laboratory  
Attn: code 5596  
4555 Overlook Ave., SW  
Washington, D.C. 20375-5320**

**J. R. Scully, MSE  
Ms. F. B. Cline, SEAS**

Defense Technical Information Center ✓  
8725 John J Kingman Road, Ste 0944  
Fort Belvoir, Virginia 22060-6218

REPORT DOCUMENTATION PAGE				Form Approved OMB No. 0704-0188	
<p>The public reporting burden for this collection of information is estimated to average 1 hour per response, including the time for reviewing instructions, searching existing data sources, gathering and maintaining the data needed, and completing and reviewing the collection of information. Send comments regarding this burden estimate or any other aspect of this collection of information, including suggestions for reducing the burden, to the Department of Defense, Executive Service Directorate (0704-0188). Respondents should be aware that notwithstanding any other provision of law, no person shall be subject to any penalty for failing to comply with a collection of information if it does not display a currently valid OMB control number.</p> <p><b>PLEASE DO NOT RETURN YOUR FORM TO THE ABOVE ORGANIZATION.</b></p>					
1. REPORT DATE (DD-MM-YYYY) 28-01-2016		2. REPORT TYPE Final		3. DATES COVERED (From - To) from 15-03-2012 to 31-12-2015	
4. TITLE AND SUBTITLE Assessing Heat-to-Heat Variations Affecting Mechanism Based Modeling of Hydrogen Environment Cracking (HEAC) in High Strength Alloys for Marine Applications: Monel K-500			5a. CONTRACT NUMBER N00014-12-1-0506		
			5b. GRANT NUMBER N/A		
			5c. PROGRAM ELEMENT NUMBER N/A		
6. AUTHOR(S) John R. Scully			5d. PROJECT NUMBER N/A		
			5e. TASK NUMBER N/A		
			5f. WORK UNIT NUMBER N/A		
7. PERFORMING ORGANIZATION NAME(S) AND ADDRESS(ES) University of Virginia Office of Sponsored Programs P.O. Box 400195 Charlottesville, Virginia 22904-4195			8. PERFORMING ORGANIZATION REPORT NUMBER 140116-101-GG11530-31340		
9. SPONSORING/MONITORING AGENCY NAME(S) AND ADDRESS(ES) Office of Naval Research 875 North Randolph Street Arlington, Virginia 22203-1995			10. SPONSOR/MONITOR'S ACRONYM(S) N/A		
			11. SPONSOR/MONITOR'S REPORT NUMBER(S) N/A		
12. DISTRIBUTION/AVAILABILITY STATEMENT Approved for public release, distribution unlimited.					
13. SUPPLEMENTARY NOTES N/A					
14. ABSTRACT The objective of the proposed work was to inform, refine, and validate a recently developed mechanism based predictive model of Hydrogen Environment Cracking (HEAC) in high strength Alloys with a focus on Monel K-500. In this proposal, laboratory based material hydrogen environment assisted cracking (HEAC) data & hydrogen interaction data will be developed based on testing of material obtained from field returned heats of aged Monel K-500 bolts or studs documented to have HEAC issues compared to such data on unfailed or commercially procured material all satisfying the QQ-N-286 specification. This comparison will serve to determine whether a recently developed & emerging predictive model of embrittlement for aged Monel K-500 fasteners subjected to cathodic polarization in marine environments must be modified to consider strong dependencies of the heat-to-heat or lot-to-lot variations in material when attempting to assess SCC lifetimes or whether the model is robust in this regard & instead should focus on general material, environmental and geometric factors such as applied electrochemical potential, remote stress, geometry and surface roughness.					
15. SUBJECT TERMS hydrogen environment cracking, high strength alloys, monel K-500 fasteners, grain boundary microchemistry, material microchemistry					
16. SECURITY CLASSIFICATION OF:			17. LIMITATION OF ABSTRACT  UU	18. NUMBER OF PAGES	19a. NAME OF RESPONSIBLE PERSON Scully, John R.
a. REPORT Unclassified	b. ABSTRACT Unclassified	c. THIS PAGE Unclassified			19b. TELEPHONE NUMBER (Include area code) 434-982-5786

**Final Report**  
**ONR Grant N00014-12-1-0506**

**Assessing Heat-to-Heat Variations Affecting Mechanism Based Modeling of Hydrogen  
Environment Cracking (HEAC) in High Strength Alloys for Marine Applications: Monel  
K-500**

Submitted to:

Office of Naval Research  
Ballston Center Tower One  
800 North Quincy Street  
Arlington, VA 22217-5660

Attention:

Dr. Airan Perez  
Program Officer  
Office of Naval Research  
airan.perez@navy.mil

Submitted by:

John R. Scully (PI) <sup>+</sup> and James T. Burns\* (Co-PI)

<sup>+</sup>Charles Henderson Chaired Professor of Materials Science and Engineering/Co-director Center  
for Electrochemical Science and Engineering

\*Department of Materials Science and Engineering  
School of Engineering and Applied Science  
University of Virginia  
Charlottesville, VA 22904

Jrs8d@virginia.edu  
434.982.5786  
434.982.5799

For investigations over the the period 3/15/12 to 12/31/16  
ONR Grant N00014-12-1-0506

20160202054

## **PROJECT ABSTRACT**

The objective of the proposed work was to inform, refine, and validate a recently developed mechanism based predictive model of Hydrogen Environment Cracking (HEAC) in high strength Alloys with a focus on Monel K-500. In this proposal, laboratory based material hydrogen environment assisted cracking (HEAC) data and hydrogen interaction data will be developed based on testing of material obtained from field returned heats of aged Monel K-500 bolts or studs documented to have HEAC issues compared to such data on unfailed or commercially procured material all satisfying the QQ-N-286 specification. This comparison will serve to determine whether a recently developed and emerging predictive model of embrittlement (*under Award #: N00014-10-1-0552 focusing on development of the scientific concepts and inputs for the stress corrosion life prediction program, SCCrack, developed to predict crack growth rate and life time to failure*) for aged Monel K-500 fasteners subjected to cathodic polarization in marine environments must be modified to consider strong dependencies of the heat-to-heat or lot-to-lot variations in material when attempting to assess SCC lifetimes or whether the model is robust in this regard and instead should focus on general material, environmental and geometric factors such as applied electrochemical potential, remote stress, geometry and surface roughness. In addition, the need for and treatment of statistical variations in input parameters will become better defined. The approach would be to test failed bolt material from the field in comparison to unfailed bolt or commercial material using cutting edge world-class crack growth and hydrogen-metal interaction characterization methods. In addition, grain boundary microchemistry would be examined via Auger or other surface science approaches to determine whether material microchemistry and intrinsic susceptibility vary from lot to lot. This work was accomplished via a research team led by Professors J. R. Scully and James T. Burns, students, one graduate students, post-doctoral researchers as well as UVA characterization facility microscope experts. The payoff from this project was improved insight into on-going questions regarding whether predictive computational models of component SCC lifetime must strongly consider heat to heat variations. Ultimately this will contribute to the development and refinement of a predictive tool that could be transitioned to DoD labs to anticipate and manage SCC lifetimes as a function of many user controlled inputs such as cathodic protection design, use of low voltage anodes, bolt load, bolt roughness etc. by providing significant input regarding whether heat-to-heat or lot-to-lot variability in material must be strongly considered and incorporated into such models. An unprecedented opportunity was exploited which combined field information with cutting edge computational modeling to refine models of stress corrosion cracking optimize model outputs. The work described herein lead to two peer reviewed publications, numerous talks, and the production of one M.S. in Materials Science and Engineering with subsequent employment in the DOD sector



## ONR TECHNICAL BACKGROUND

### Introduction

A range of hydrogen assisted cracking problems currently limits use of high strength alloys in the marine environment. These interactive processes are highly localized at the crack tip and apply to Monel K-500.

The alloy of focus is Monel K-500 (63Ni-27Cu-3Al-0.5Ti).<sup>1</sup> Monel K-500 (UNS N05500) is a precipitation-hardenable nickel-copper alloy that combines the corrosion resistance of MONEL Alloy 400 with greater strength and hardness. It is strengthened by a combination of cold work and aging to form fine Ni<sub>3</sub>(Ti,Al) phases. The alloy is used for pump shafts, oil-well tools and instruments, surgical blades and scrapers, springs, valve trim, fasteners, and marine propeller shafts. These Ni-based alloys differ considerably from quenched and tempered steels which derive strength from a body-centered martensite crystal structure and secondary age hardening. A range of properties differ from H-metal interactions to physical properties. However, a common feature is that cracking is dominated by crack tip hydrogen concentration and that HEAC leads to intergranular fracture that can be developed in cold worked and aged Monel K-500 in near neutral NaCl solution polarized to -1.0 V vs. SCE and subjected to slow-rising crack mouth opening displacement.

### Seawater HAC susceptibility of Monel K-500

In the early 1960s, Monel Alloy K-500 (UNS N05500) was believed to be relatively immune to hydrogen environment embrittlement and stress corrosion cracking<sup>2</sup>. Stress corrosion cracking in H<sub>2</sub>S environments under high stress, high pressure and temperature steam and HF vapors and Hg were noted (for Monel alloy 400 or Monel Alloy K-500 (UNS N05500)).<sup>3</sup> Reports in the 60s through 80s began to indicate susceptibility to room temperature hydrogen environment embrittlement<sup>4,5,6</sup> mainly seen as a low in tensile ductility and notch strength ratio. Scully noted that embrittlement on SHT and aged Monel Alloy K-500 (UNS N05500) (Rockwell C 25-35) occurred in seawater at room temperature when coupled to zinc and that hydrogen levels increased over an 8 week period to 50 wppm. A strain rate effect was also observed even in pre-charged material.

---

<sup>1</sup> 1. Special Metals product data sheet on Monel Alloy K-500 (UNS N05500), [www.specialmetals.com](http://www.specialmetals.com)

<sup>2</sup> 2. R. Copson and C. F. Cheng, Corrosion, vol. 12 (1956): p. 647.

<sup>3</sup> 3. K. D. Efind, Materials Performance, vol. 24 (1985): p. 37-40.

<sup>4</sup> 4. J. A. Harris, C. D. Stephens and Scarberr.Rc, Corrosion, vol. 28 (1972): p. 57.

<sup>5</sup> 5. C. E. Price and R. S. Fredell, Metallurgical Transactions a-Physical Metallurgy and Materials Science, vol. 17 (1986): p. 889-898.

<sup>6</sup> 6. J. R. Scully and M. G. Vassilaros, DTNSRDC SME 84-69, (1984): p. 1-28.

Since these initial reports, nickel-copper alloy bolt failures have also been observed numerous times in age hardened Monel Alloy K-500 (UNS N05500) subjected to normal cathodic polarization when coupled to aluminum anodes in seawater.<sup>7</sup> Failures by intergranular cracking have been attributed to hydrogen production, uptake and embrittlement as a result of cathodic polarization and was first attributed to high thread root hardness of HRC 39 due to age hardening after threading. It was recommended that first annealing and then age hardening be conducted after threading to limit hardness below the acceptable hardness (HRC 35) of Monel Alloy K-500 (UNS N05500). This was a suggested hardness limit in sour systems. This hardness limit was also suggested by a Military specification. However, additional failures have occurred in roll-threaded Monel Alloy K-500 (UNS N05500) bolts annealed at 980-1050°C, water quenched, and precipitation age hardened at 500-600°C for 16 h producing a Rockwell C hardness of only 25.<sup>7</sup> Embrittlement failures occurred in bolts after about one year under load to about 59% of the tensile yield strength and continuously cathodically protected with anode grade aluminum. These failures have continued. Intergranular cracking could be reproduced under slow strain rate testing in air after 8 day pre-charging when coupled to Al or charged potentiostatically (annealed and aged Monel Alloy K-500 (UNS N05500)) and to a lesser extent when coupled to steel or potentiostatically polarized to -800 mV vs. Ag/AgCl (only seen for aged Monel Alloy K-500 (UNS N05500)) in ASTM artificial ocean water.

The hydrogen embrittlement assisted cracking (HEAC) behavior of other Ni-based superalloys in gaseous H<sub>2</sub> and aqueous exposure has been reviewed in detail elsewhere.<sup>2</sup> The severity of this cracking problem is apparent in many nickel base alloys such as Alloy 718.<sup>2</sup> However, few studies have documented the threshold stress intensity for hydrogen environment embrittlement cracking in Monel Alloy K-500 (UNS N05500) and there were no reports on crack growth rate in controlled testing prior to ONR funded work under the prior projects N00014-06-1-0366 and N00014-10-1-0552 and work at LUNA. Raymond noted using the step rising load method that the threshold stress intensity of aged Monel Alloy K-500 (UNS N05500) (Rockwell C hardness = 30) decreased from >69 MPa√m at -0.7 V<sub>SCE</sub> to <18 MPa√m at -1.0 V<sub>SCE</sub> in room temperature NaCl solution.<sup>8</sup> Moreover, little was known about hydrogen uptake, transport and trapping behavior in this alloy until projects N00014-06-1-0366 and N00014-10-1-0552. The effective hydrogen diffusion coefficient in pure single crystal Ni was 8.4 x 10<sup>-10</sup> cm<sup>2</sup>/sec with an activation energy of 39.5 kJ/mole. In contrast, diffusion was faster in copper at 1.29 to 1.95 x 10<sup>-9</sup> cm<sup>2</sup>/sec with an activation energy from 36-38 kJ/mole. Harris as well as Scully suggested from the limited depth of intergranular cracking in cylindrical specimens charged with hydrogen that hydrogen diffusion rates must be on the order of 10<sup>-10</sup> cm<sup>2</sup>/sec.<sup>8,10</sup> However, these estimates are indirect. A Ni-30 at. % Cu alloy had a hydrogen diffusivity of 3x10<sup>-10</sup> cm<sup>2</sup>/sec and an effective activation energy for diffusion of 41 kJ/mole.<sup>9</sup> Only one paper reports data for Monel Alloy K-

<sup>7</sup> L. H. Wolfe and M. W. Joosten, SPE Production Engineering, 1988): p. 382-386.

<sup>8</sup> L. Raymond, LRA report # CTC'071024,(2008): p. 1-16.

<sup>9</sup> D. J. Mitchell and E. M. Edge, Journal of Applied Physics, vol. 57 (1985): p. 5226-5235.

500 (UNS N05500). The material was SHT at 900°C and radiatively cooled. The microstructure and hardness were not reported but minimal aging is suggested by this treatment.  $D_{eff}$  was reported to be  $7.6 \times 10^{-11} \text{ cm}^2/\text{sec}$ .<sup>10</sup> In recently completed work under our previous ONR grant,  $D_{eff}$  at 25 °C was suggested to be 1 to  $3.3 \times 10^{-10} \text{ cm}^2/\text{sec}$  for aged Monel K-500. However, it was felt that this value was uncertain by a factor of 2 to 4. This difference is crucial to predictions of stage II crack growth as will be discussed below  $[da/dt]_{II}$ .

Moreover, hydrogen assisted cracking susceptibility in aqueous environments is controlled by and increases (to a theoretical upper bound) with the crack tip diffusible hydrogen concentration which is, in turn, controlled by the hydrogen overpotential and production rate.<sup>10</sup> Metallurgical trap states are important and either serve as benign sinks for hydrogen, function as the crack initiation sites and the crack propagation path itself or function as a reservoir of hydrogen that can be supplied to the tensile triaxial stress field of the stationary or moving crack tip.

Additionally, stage II environmental crack velocities at the upper bounds of hydrogen uptake rates where cracking is not surface uptake limited is often controlled by the effective diffusion rate of hydrogen at the crack tip.<sup>16</sup> These parameters may differ between SHT, cold worked and aged Monel K-500 and may help explain observed differences in susceptibility of aged Monel K-500 from heat to heat. For all these reasons,  $C_{H,diff}$ , the diffusible hydrogen concentration absorbed in the nickel base alloy as a function of cathodic potential, and the effective hydrogen diffusion coefficient  $D_{eff}$  are critical parameters of interest in order to predict  $[da/dt]_{II}$  and  $K_{th}$  in UNS N05500. However,  $C_{H,diff}$  behavior as a function of hydrogen overpotential or cathodic hydrogen production rate has only recently been established in Monel Alloy K-500 (UNS N05500) in previous ONR grants. These values were uncertain by a factor of 2-3. Moreover,  $D_{eff}$  and trapping behavior have just been explored over a range of technologically significant conditions such as the solution heat treated, cold worked as well as the age hardened conditions. Refinement of these parameters is crucial to not only the accurate prediction of  $K_{th}$  and  $[da/dt]_{II}$  but assessment of heat to heat variations.

#### Prediction of Stage II crack velocity $[da/dt]_{II}$ and $K_{th}$ in recent work under ONR N00014-06-1-0366 and N00014-10-1-0552

In addition to the threshold stress intensity factor for HEAC, is it important to understand and model predict the Stage II crack growth rate as mentioned above. This information will be crucial to the prediction of component lifetimes. Figure 1 shows  $[da/dt]$  vs  $K_{app}$  for aged Monel K-500 (Allvac). The upper bound crack growth rate is  $\sim 2 \times 10^{-1} \text{ um/sec}$  or  $2 \times 10^{-4} \text{ mm/sec}$ .

<sup>10</sup> B. A. Kehler and J. R. Scully, Corrosion, vol. 64 (2008): p. 465-477.



A substantial correlation of the fastest rates of HEAC were obtained from past experiments at UVA, using a common experimental method, and from literature results for high strength alloys stressed during exposure in chloride solutions HEAC experiments are challenging and costly, and should be augmented by modeling. Diffusion-based models were developed to describe  $da/dt_{II}$  for HEAC based on FPZ supply from the concentration of H on the crack tip surface and in equilibrium with the local environment ( $C_S$ ), as reviewed and implemented for steel.<sup>2,11</sup> In general models of this type are of varying complexity depending on whether the H-diffusion field is: (a) concentration and/or stress driven, (b) transient or steady state, (c) ahead of a stationary or moving crack, (d) modeled in one or two dimensions (e) emanating from environment-sensitive  $C_S$ , (f) microstructure-trap affected, (g) plastic strain-trap affected, and (h) coupled with a H-failure criterion. The results of diffusion modeling are of the general form:

$$\frac{da}{dt_{II}} = \frac{D_{Heff}}{\chi_{CRIT}} \left[ \xi \left( \frac{C_O}{C_{CRIT}}, D_{Heff}, \chi_{CRIT}, \sigma_{YS}, t \right) \right]$$

Where:  $\chi_{CRIT}$  is the critical distance for H diffusion ahead of the crack tip,  $D_{Heff}$  is trap modified H diffusivity,  $C_O$  is the concentration of H and governed by crack electrochemistry (equilibrium or surface reaction rate limited)  $\sigma_{YS}$  is alloy tensile strength,  $t$  is time, and  $\xi$  is a function of the indicated variables (equaling between 4.0 and 0.01 depending on diffusion boundary condition). The observed and predicted proportionality between Stage II crack growth rate and  $D_{Heff}$  in Fig. 2 supports H-diffusion control of HEAC. An upper bound  $\chi_{CRIT}$  can be determined from these data. The highest-reasonable value of  $\xi$  is 3 and constant, provided that the  $da/dt_{II}$  are not sensitive to  $C_O$  for the various chloride solutions and if cracking is governed by constant  $C_{CRIT}/C_S$  of order 2. These assumptions result in  $\chi_{CRIT} = 0.7 \mu m$  for the trend line in Fig. 4, independent of alloy. The data for aged Monel K-500 are consistent with the trend curve assuming a  $D_{eff}$  of  $\sim 2 \times 10^{-10} \text{ cm}^2/\text{sec}$ .

<sup>11</sup> Yongwon Lee and Richard. P. Gangloff, "Measurement and Modeling of Hydrogen Environment Assisted Cracking of Ultra-High Strength Steel", Metallurgical and Materials Transactions, A, vol. 38, pp. 2174-2190 (2007).

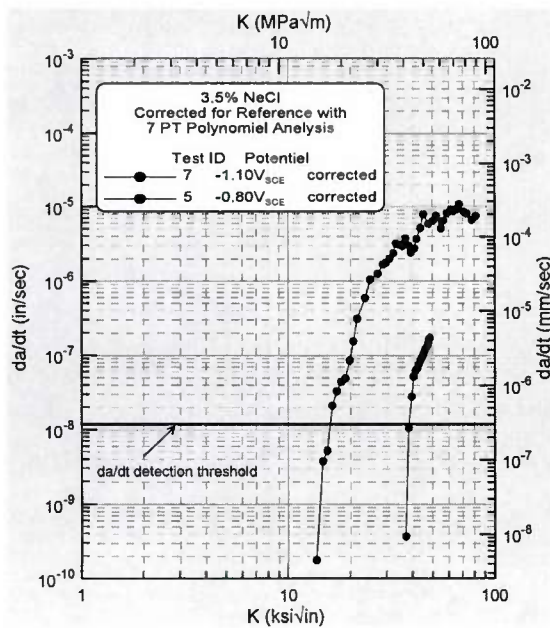


**Figure 1.** Slow rates of IG SCC in Monel K-500 (ST-A) accurately measured in 6 day experiment with slow-rising CMOD; consistent with H-diffusion limited Stage II SCC. (Allvac Monel K-500 tested at FTA in 2011).

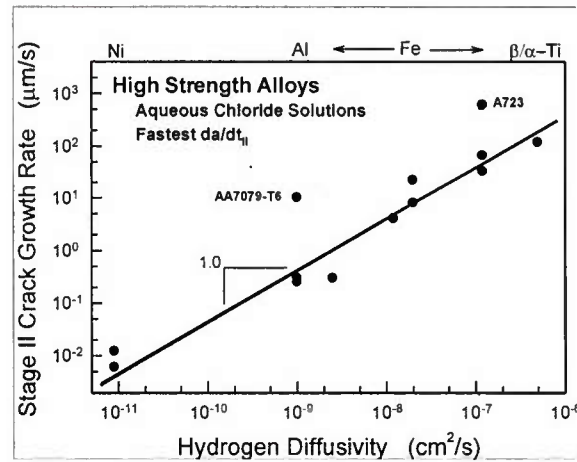


**Figure 2.** Diffusion-based upper bound level of  $da/dt_{II}$  for HEAC based on FPZ supply from the concentration of H on the crack tip surface and in equilibrium with the local environment ( $C_s$ ), as reviewed and implemented for steel. The data for aged Monel K-500 are consistent with the trend curve assuming a  $D_{eff}$  of  $2 \times 10^{-10} \text{ cm}^2/\text{sec}$

#### Application of Approach to Monel K-500 under cathodic polarization in seawater

Under a previously funded project, ONR N00014-06-1-0366,  $[da/dt]_{II}$  and  $K_{IH}$  were measured and modeled. Examples of the application of this proposed approach to Monel K-500 are shown in Figure 2 where hydrogen uptake law was explored on planar electrodes as a function of hydrogen overpotential and charging current density in an alkaline solution designed to represent a cathodically polarized crack tip. This hydrogen concentration can be connected to crack geometry through Figure 6 where hydrogen overpotential has been predicted as a function of the crack geometry parameter  $x^2/G$  and applied potential at the crack mouth. These data were obtained for a rescaled crevice and based on cathodic reaction kinetics measured for steel and will be redone for Monel K-500 in the proposed work. Crack tip hydrogen concentration must be predicted and measurements were calibrated against LECO measurements. A refined assessment of the diffusible hydrogen content as a function of applied external potential and crack depth was undertaken for Refinements include updated determination of  $C_{H,diff}$  (probably lowered) which should raise predicted values of  $K_{IH}$  towards experimentally determined values. Additional crucial pieces of information required as input to  $da/dt$  modeling include  $D_{Heff}$ ,  $X_{crit}$  and  $C_{Crit}$ .  $D_{Heff}$  was determined via the TDS method in N00014-06-1-0366. To refine estimates of  $D_{eff}$ , these measurements are corroborated using some other independent method in the current work.

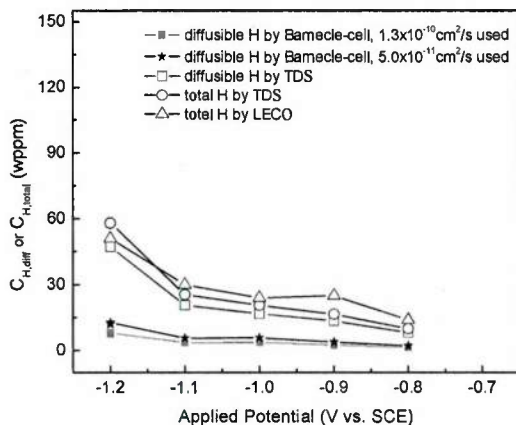


**Figure 3.**  $C_{H,diff}$  and  $C_{TOT}$  for hot finished and age-hardened, Monel K-500 ALLVAC (63%Ni – 33%Cu – 3.2%Al – 2%Fe) [UNS N05500].

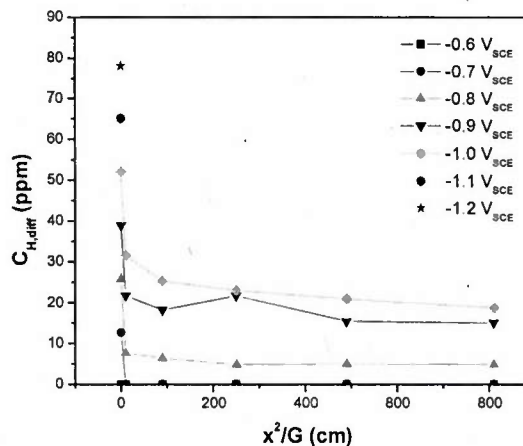


**Figure 4.**  $C_{H,diff}$  versus applied potential for various  $x^2/G$  values. The data applies to Allvac aged Monel K-500 analyzed after 300 sec with hydrogen analysis from TDS.

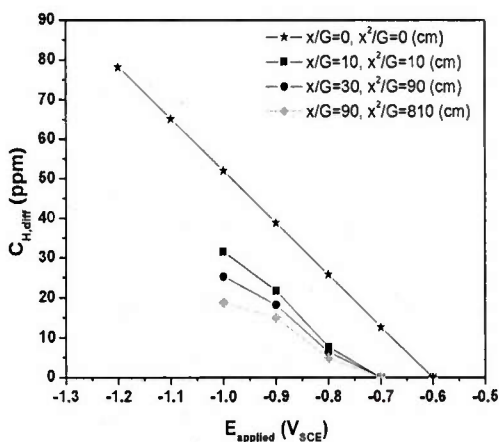


**Figure 5.** Predicted  $C_{H,diff}$  from TDS versus applied potential for SHT/aged Monel K-500 (ALLVAC) at various  $X^2/G$  values.

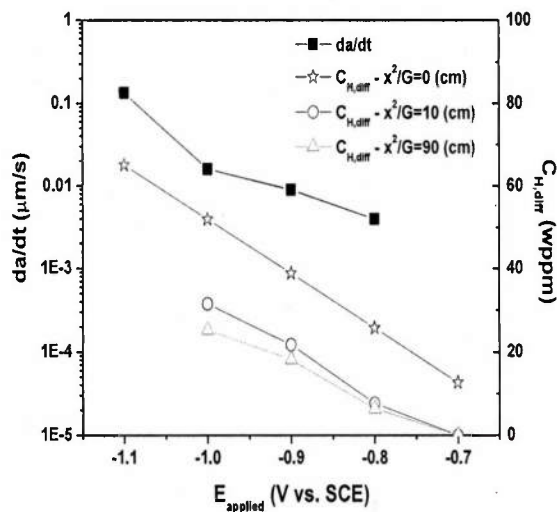


**Figure 6.** Experimental data for the potential dependence of  $[da/dt]_{II}$  for hot finished and aged Monel K-500 (ALLVAC) stressed in 3.5% NaCl solution. Hydrogen levels were obtained from TDS measurements.

In crack growth studies under work under ONR N00014-06-1-0366 and N00014-10-1-0552, the following findings were obtained. The crack growth rate was found to be a strong function of

electrochemical potential (Figure 6) and therefore crack tip hydrogen concentration. In fact, a substantial increase in crack growth rate is predicted as a function of  $E_{app}$  and thus crack tip hydrogen concentration as seen in Figures 7 and 8 and seen experimentally in aged Monel K-500 (Figure 8). This means that:

- HEAC of aged Monel K-500 will be a strong function of applied potential and will likely be extremely sensitive to applied cathodic potential, local potential, geometry, materials and stress state.
- Any metallurgical variable or heat-to-heat variable not captured by gross changes in material hardness that might change the trajectory of  $[da/dt]_{II}$  with  $E_{app}$  as seen in Figures 6-8 could significantly change the HEAC lifetime of components exposed to hydrogen embrittlement.

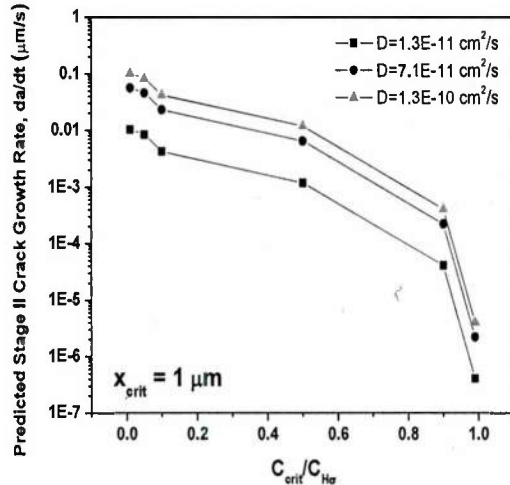


**Figure 7.** Prediction of crack growth rate in SHT-aged K500 as a function of reduced hydrogen concentration.  $Y_s = 783 \text{ MPa}$  aged Monel K-500.  $V_h = 1.73 \text{ cm}^3/\text{mole H}$  from Moody, Baskes for Nickel see Ha spreadsheet.  $\sigma_{ys} = 783 \text{ MPa}$   $\sigma_H = 6 \sigma_{ys}$   $V_H = 1.73 \text{ cm}^3/\text{mole H}$

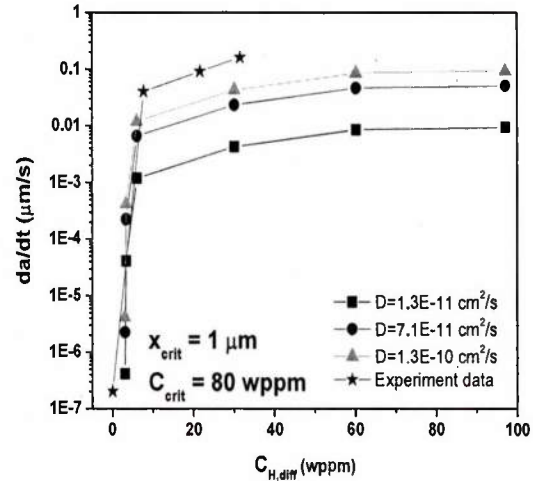


**Figure 8.** Crack Growth rate in SHT-aged K-500: Experiment vs. Calculation Using TDS data(ALLVAC) to calculate  $C_{H,diff}$  at  $E_{applied}$  at  $x^2/G = 10 \text{ cm}$ . The first experimental data point ALLVAC) is at  $-700 \text{ mV}$  vs. SCE. The last is at  $-1100 \text{ mV}$  vs. SCE. These data indicate the effect of potential.



## **SUMMARY BASED ON FINDINGS UNDER ONR N00014-06-1-0366 and N00014-10-1-0552**

The crack propagation perspective provides a framework to quantify subcritical cracking phenomena for component life assessment in a marine application. Improvements to H cracking models were achieved in prior work by developing new understanding of crack tip electrochemistry and mechanics, as guided by the existing interdisciplinary experience base. The Monel K-500 alloys system provides an ideal case, of both practical and scientific relevance, to extend understanding of HEAC modeling. By coupling with external definition of the mechanics condition, the lifetime of the component can be estimated as long as the state of stress, material, geometry, electrochemical conditions, and temperature are defined. However, this work fills a crucial gap. Specifically, assessing how heat to heat variations affect model inputs and how statistical variations should be treated with a rational technical basis inside of the SCCcrack model.

### **OBJECTIVES**

The overall objective of this interdisciplinary research program is to implement quantitative-predictive models of hydrogen environment assisted cracking (HEAC) of Monel K-500 in a pseudo-application specific situation.

The objective of this work was to inform, refine, and validate recently developed mechanism based predictive model of Hydrogen Environment Cracking (HEAC) in High Strength Alloys with a focus on Monel K-500. Lab based material cracking data and hydrogen interaction data were developed based on testing of material obtained from failed heats of Monel K-500 bolts or studs as compared to such data on unfailed material all satisfying the QQ-N-286 specification. This comparison served to determine whether the UVA recently developed and emerging predictive model of embrittlement *must* be modified to consider strong dependencies of the heat-to-heat variations in material on SCC lifetimes or whether the model is robust in this regard and instead should focus on general material, environmental and geometric factors such as applied electrochemical potential, remote stress, geometry and surface roughness.

The specific objectives of this work were to ascertain from field failed as well as commercial purchased Monel K-500:

- Quantitative characterization of the HEAC susceptibility of several heats of aged Monel K-500 over a range of cathodic potentials relevant to cathodic protection in seawater via state-of-the-art crack growth assessment techniques.



- Characterization of basic metallurgical properties of several heats of aged Monel K-500 material as well as the grain boundary microchemistry that may control variations in intergranular HEAC susceptibility.
- Characterization of the number of traps and the trap binding energies and other hydrogen related properties of several heats of aged Monel k-500 material.
- Determination of the heat to heat and within heat statistical variations in hydrogen concentrations and  $[da/dt]_{II}$  rates over a range of pertinent cathodic potentials.

## **TECHNICAL APPROACH**

The objectives were met by study of six separate lots of aged Monel K-500 each of which meet the QQ-N-286 specification that governs procurement of this material. One of the material heats was obtained from a commercial supplier (Allvac) and 5 separate material lots were supplied by NSWC-CD from field returned aged Monel K-500 components. The research effort was divided into three main thrusts.

- First a detailed characterization of the metallurgy and baseline material properties of each lot was performed to identity the microstructural differences between each lot of material.
- Second, the HEAC susceptibility of each lot of material was established for various environment via both slow-strain rate tensile testing and state-of-the-art fracture mechanics based characterization of the crack growth behavior as a function of the applied stress intensity (K).
- Third, the H-metal interactions were assessed for each material lot. The data from each of these efforts were interpreted in the context of previously developed and validated micro-mechanical models to quantitatively evaluate how the observed changes in microstructure would result in the measured changes in HEAC susceptibility.

Detailed motivation, experimental methods, results, discussion and conclusions for the efforts in each of the three thrust areas are reported in the following two chapters. Figures are numbered in each section chronologically.

- **Chapter 1** details the materials used, the microstructural characterization relevant to the HEAC behavior, the LEFM fracture process and results, and the micro-mechanical modeling.
- **Chapter 2** details the H-metal interaction analysis, slow-strain rate results, Auger analysis, and further micro-mechanical modeling.

## **SUMMARY OF FINDINGS**

The detailed findings of this work are incorporated in each chapter. However, three at-large findings traced to the above primary objectives were met. Approaches for incorporating heat to heat variations in fracture modeling from either the fracture mechanics perspective and notched tensile bar perspectives were proposed. Possible additions to the federal specification based on beneficial and detrimental elements and a possible equation for trace element composition were proposed. Lastly a few test methods were proposed that can be used to elucidate relative susceptibility. Specifically, the slow strain rate method may be utilized to rapidly assess alloys prone to intergranular hydrogen cracking at intermediate cathodic protection levels.

## **TRANSITIONS**

The long range payoff of this research for the USN will be the ability to predict the environmental cracking threshold stress intensity and crack growth rate for any nickel based alloy such as Monel K-500 fasteners in a marine environment, as a function of applied electrochemical potential, defect geometry, alloy metallurgy and state of stress with an assessment of heat to heat variations. The question of whether and how predictive computational models of component SCC lifetime can consider heat to heat variations was addressed. Ultimately this work will enhance the development, refinement and the use of a predictive tool that could be transitioned to Navy labs to anticipate and manage SCC lifetimes as a function of cathodic protection design, low voltage anodes, bolt loads, bolt roughness etc. with significant input on whether heat-to-heat or lot-to-lot variability in material must be strongly considered and incorporated into such models. An unprecedented opportunity combine field information with cutting edge computational modeling was undertaken.

For instance these alloys are used in flooded spaces and experience various degrees of cathodic protection. Such predictions will be sufficiently quantitative for direct use in component-level analysis including time to failure. The output will be suitable for a range of components but including high strength fasteners, rods and studs in wetted marine environments. The models produced to achieve this capability will ultimately be sufficiently simple to be implemented on a desktop computer in the engineering environment.

Insight might also be provided leading to the further refinement of QQ-N-286 standard leading to an enhanced ability to weed out HEAC susceptible tempers of Monel K-500 when subjected to cathodic protection in seawater.

## CHAPTER 1

### **The Effect of Microstructure Variation on the Hydrogen Environment-Assisted Cracking of Monel K-500**

Zachary D. Harris, Justin D. Dolph, Greger L. Pioszak, Brendy C. Rincon Troconis, John R. Scully, and James T. Burns

Center for Electrochemical Science and Engineering

Department of Materials Science and Engineering

University of Virginia

Charlottesville, VA 22904

#### **Abstract**

The influence of microstructure variation on hydrogen environment-assisted cracking (HEAC) of Monel K-500 was evaluated using five nominally peak-aged lots of material tested under slow-rising stress intensity loading while immersed in NaCl solution under cathodic polarizations. Minimal variation in HEAC resistance amongst material lots was observed for an applied potential of  $-950 \text{ mV}_{\text{SCE}}$  ( $E_{\text{app}}$ , vs. saturated calomel), while significant differences in both fracture morphology and HEAC resistance were observed at the less negative potential of  $-850 \text{ mV}_{\text{SCE}}$ , suggesting that relatively severe H environments produce sufficient crack-tip H to minimize the impact of metallurgical differences. Sensitivity analyses accomplished by varying the inputs used in decohesion-based, micromechanical models imply significant variations in HEAC resistance are possible for realistic changes in grain boundary toughness, hydrogen uptake behavior, and yield strength. Grain size, impurity segregation (including the effects of gettering elements), grain boundary character/connectivity, and crack path tortuosity are also considered in the context of HEAC susceptibility. Yield strength, global hydrogen content, as well as impurity segregation to grain boundaries, especially boron and sulfur, are speculatively considered to be the dominant contributions in determining HEAC resistance. Modifications that would incorporate the effects of grain boundary segregation are proposed for the  $K_{\text{TH}}$  model; detailed validation of such changes require high fidelity and quantitative inputs for the degree of grain boundary segregation. Regardless, fracture mechanics-based HEAC results, detailed microstructure characterization, and micromechanical modeling were successfully coupled to gain insights into the influences governing the microstructure-dependent HEAC susceptibility of Monel K-500.

## Introduction

Monel K-500 is a Ni-Cu-Al superalloy commonly used in marine applications due to its excellent combination of corrosion resistance, strength, and fracture toughness. For such applications, environment-assisted cracking (EAC) is historically evaluated via a wide- and diverse-range of testing approaches (e.g. NACE MR0175 and ASTM G30, G39, G129, E1681, and F1624 [1–6]). Material selection engineers will often use data from such tests in a “go/no-go” paradigm where the long-term EAC resistance is inferred by empirical material testing. Specifically, if testing indicates that the service environment and loading conditions are below a threshold level of severity, it is then assumed that cracking will not occur over the lifetime of the component. Such an approach is codified in NACE MR0175 which outlines guidelines for the selection of “cracking resistant materials” in  $H_2S$  environments (of note is that this specification does state that materials meeting this standard are “not necessarily” immune under all service conditions). The inadequacy of this “go/no-go” approach is demonstrated by isolated long-time ( $\sim 10$  year) service failures of Monel K-500 components on North Sea oil and gas platforms, deep gas wells, and US Navy sea vessels [7–13]. In each of these cases, the Monel K-500 components were immersed in seawater and cathodically polarized to protect adjacent carbon and low alloy steel structures. This service environment, combined with the observation of fracture surfaces that exhibited intergranular (IG) with small amounts of transgranular (TG) crack growth [7,8,11–13], suggests that the failure of these components can be attributed to EAC – an assessment corroborated by laboratory testing of Ni-based superalloys [14–18].

These service failures expose critical, non-conservative flaws in the existing approach to EAC management for current- and next-generation materials. Specifically, current EAC characterization techniques, material selection criteria, and structural integrity prognosis approaches fail to fully account for conditions where slow sub-critical crack propagation occurs over a significant portion of component life. This deficiency demonstrates the need for high-fidelity linear elastic fracture mechanics-based (LEFM) material characterization of both the threshold stress intensity for EAC ( $K_{TH}$ ) and the steady state (stage II) sub-critical crack growth kinetics ( $da/dt_{II}$ ) for the pertinent service environment [19]. Additionally, if slow crack propagation dominates the total service life of the component, then sub-critical crack growth kinetics can be coupled with LEFM-based life prediction methods (e.g. *SCCrack*, recently developed for EAC modeling [20]) to provide a powerful tool for structural design, material/coating/cathodic protection selection, and/or structural life management. An analogous approach is well established in the fatigue community where LEFM-based programs are commonly used to aid structural life management [21–23]. Ultimately, the rigor of the LEFM approach is critically dependent



on the applicability of the crack growth kinetics data to the relevant environment, loading conditions, and material of interest. An initial study evaluated the influence of the former two variables on EAC behavior in Monel K-500 [18], but the effect of lot-to-lot metallurgical variation on HEAC susceptibility is not known.

Crack growth kinetics for environment/cathodic polarization combinations pertinent to marine service conditions were established in prior work using direct current potential difference (dcPD) [24] to monitor crack progression during slow-rising displacement testing of single-edge notched (SEN) specimens from a single lot of Monel K-500 [18]. The resulting data quantitatively demonstrated that decreasing the applied potential from  $-750 \text{ mV}_{\text{SCE}}$  to  $-1100 \text{ mV}_{\text{SCE}}$  in 0.6 M NaCl solution will decrease the EAC threshold ( $K_{\text{TH}}$ ) and increase the stage II crack growth rate ( $da/dt_{\text{II}}$ ). In addition to their engineering relevance, these data provided the basis for micromechanical modeling of potential-dependent EAC in the context of a decohesion-based hydrogen (H) embrittlement mechanism. Estimates of the overpotential for H production at the crack-tip were established as a function of bulk applied potential via rescaled crevice experiments [18]. These data were coupled with effective H solubility measurements versus H overpotential to establish that the crack-tip diffusible H concentration ( $C_{\text{H-Diff}}$ ) rises with decreasing applied potential from  $-750$  to  $-1100 \text{ mV}_{\text{SCE}}$  [25]. As the level of cathodic polarization increases, the increase in EAC susceptibility directly scales with increasing crack-tip diffusible H concentration, thereby suggesting that H environment-assisted cracking (HEAC) is the governing mechanism for sub-critical cracking in Monel K-500. This finding is consistent with a wide literature that supports the H-embrittlement phenomenon in Ni-based alloys [26–31]

While several viable mechanisms for hydrogen embrittlement in Ni-based alloys exist [32–34], hydrogen-enhanced decohesion-based (HEDE) models provide a means to quantitatively relate the stress-enhanced H concentration ( $C_{\text{H-}\sigma}$ ) in the fracture process zone (FPZ) to the relevant HEAC metrics ( $K_{\text{TH}}$  and  $da/dt_{\text{II}}$ ) [35–38]. Critically,  $C_{\text{H-}\sigma}$  can be calculated from the empirically determined  $C_{\text{H-Diff}}$ , thereby establishing  $C_{\text{H-}\sigma}$  as the key environmental variable in the HEDE models for  $K_{\text{TH}}$  and  $da/dt_{\text{II}}$ . Prior work argued that this relationship (Eqn 1) can be described with Fermi-Dirac statistics by reasonably assuming a single dominant reversible trap site and low lattice H concentrations [18].

$$C_{\text{H-}\sigma} = C_{\text{H-Diff}} \exp \left[ \frac{\sigma_{\text{H}} V_{\text{H}}}{R T} \right] \quad (\text{Eqn 1})$$

where  $V_{\text{H}}$  is the partial molar volume of hydrogen in a nickel lattice ( $1.73 \text{ cm}^3/\text{mol H}$ ) [18],  $R$  is the gas constant,  $T$  is temperature, and  $\sigma_{\text{H}}$  is the hydrostatic stress located a distance of  $x_{\text{crit}}$  ahead of the crack-tip. Depending on the approach (discrete dislocation models, blunted crack finite element models, or



strain gradient plasticity models), crack-tip mechanics estimates of  $\sigma_H$  vary from 3 to 20 times the yield strength of the alloy [39].

$K_{TH}$  for HEAC is predicted using the decohesion-based, micromechanical model proposed by Gerberich *et al.* [32,35,38] (Eqn 2) to describe the near crack-tip stress state:

$$K_{TH} = \frac{1}{\beta'} \exp \left[ \frac{(k_{IG} - \alpha C_{H\sigma})^2}{\alpha'' \sigma_{YS}} \right] \quad (\text{Eqn 2})$$

where  $\beta'$  ((MPa $\sqrt{m}$ )<sup>-1</sup>) and  $\alpha''$  (MPa-m) are constants from modeling the dislocation shielding of the crack-tip elastic stress,  $k_{IG}$  (MPa $\sqrt{m}$ ) is the intrinsic Griffith toughness of the grain boundary,  $\alpha$  (MPa $\sqrt{m}(\text{atom fraction of hydrogen})^{-1}$ ) is a weighting factor which defines the decrease in  $k_{IG}$  per unit H concentration, and  $\sigma_{YS}$  (MPa) is the yield strength [18,32,35]. The steady-state (stage II) sub-critical HEAC growth behavior is limited by the diffusion of H from the crack-tip surface to the location of maximum stress within the FPZ [18,37]. As such, a HEDE-based model for H-diffusion ahead of a discontinuously propagating crack results in the relationship given in Eqn 3.

$$\left( \frac{da}{dt} \right)_{II} = \frac{4 D_{eff}}{x_{crit}} \left( \text{erf}^{-1} \left( 1 - \frac{C_{H\sigma-crit}}{C_{H\sigma}} \right) \right)^2 \quad (\text{Eqn 3})$$

where  $D_{eff}$  is the effective diffusivity of hydrogen which accounts for the presence of trap sites in the alloy (reported values are bounded by  $5.0 \times 10^{-11}$  cm<sup>2</sup>/s and  $1.3 \times 10^{-10}$  cm<sup>2</sup>/s for Monel K-500 [25]),  $x_{crit}$  is the critical distance ahead of the crack-tip where discontinuous H-assisted crack advance nucleates, and  $C_{H\sigma-crit}$  is the critical concentration of hydrogen necessary to activate decohesion at  $x_{crit}$  [18]. The parameter  $x_{crit}$  is on the order of 1  $\mu\text{m}$  for many high strength alloys and is related to the position of maximum hydrostatic stress in front of the crack tip [40]. Prior work demonstrated that using a single experimentally calibrated parameter and the empirically derived applied potential versus  $C_{H-Diff}$  relationship gave predictions from Eqn 2 and 3 that showed excellent agreement with measured HEAC parameters for applied potentials ranging from -700 to -1100 mV<sub>sce</sub> in a single lot of Monel K-500 [18]. The success of these HEDE-based micromechanical modeling paradigms, along with the high fidelity of the dcPD technique for measuring crack growth, justify the extension of these approaches to understand the effect of metallurgical variation on HEAC behavior.

The effect of lot-to-lot variations in metallurgy on HEAC susceptibility is especially relevant for Monel K-500. The specification governing material procurement (Federal Specification QQ-N-286G) is a

property-driven document that specifies benchmarks for composition, mechanical properties, IG susceptibility, and grain size uniformity [41]. However, while there are suggested heat treatments, the specification allows for age hardening to “be accomplished by any process proved adequate to meet the mechanical property requirements” [41]. This flexibility in production can lead to vast variations in strength and metallurgical features and their effects are unlikely to be captured by the rudimentary testing mandated by QQ-N-286G for determining IG failure susceptibility. Changes in the grain size, the distribution of grain boundary misorientation angles, the bulk impurity concentration, the degree of impurity segregation, the precipitate morphology, and the post-processing dislocation density will vary with material lot/processing route. Critically, these changes can influence the HEAC behavior by modifying the material strength, slip behavior, grain boundary cohesion characteristics, crack path connectivity/tortuosity, and/or H-metal interactions. The micromechanical models detailed in Eqn. 2 and 3 provide a quantitative framework to link these metallurgy variations with the HEAC behavior by speculating how lot-to-lot differences vary the pertinent input parameters ( $k_{IG}$ ,  $\alpha$ ,  $\sigma_{YS}$ ,  $x_{crit}$ ,  $C_{H,Diff}$ ,  $C_{H-\sigma}$ ,  $D_{eff}$ , and  $C_{H\sigma-crit}$ ). However, a systematic characterization and analysis of the relative influence of changes in these metallurgical features on the HEAC behavior is lacking for Monel K-500.

The objective of this paper is to evaluate the extent to which the HEAC behavior varies for Monel K-500 lots that meet the QQ-N-286G specification. First, HEAC susceptibility is assessed through fracture mechanics testing in both an inert environment and in full immersion NaCl solution under mild and aggressive cathodic polarizations. Second, a detailed characterization of the microstructure is performed to identify the variation in metallurgical features for each tested lot of Monel K-500. Third, several aspects of the H-metal interactions are investigated. Finally, the results of these analyses are coupled with the micromechanical model for  $K_{TH}$  (Eqns 1 and 2) to quantitatively evaluate how observed changes in the microstructure may relate to the resulting HEAC behavior.

## Experimental Methods

### 2.1 Material

Monel K-500 is composed of an austenitic Ni-Cu solid solution matrix ( $\gamma$ ) that is precipitation-hardened by the intermetallic  $\gamma'$  ( $Ni_3(Al,Ti)$ ) phase. The  $\gamma'$  precipitates are homogeneously distributed and highly coherent (<0.1% misfit strain) with an ordered  $L1_2$  structure composed of Ni atoms at the faces and Al (or Ti) atoms on the corners of the unit cell [42–44]. Due to this low misfit, these precipitates form as spherical particles – a morphology that is maintained even after prolonged aging [43]. Dislocation interactions with  $\gamma'$  are generally controlled by the size of the  $\gamma'$  precipitates, with a noted shift from

dislocation cutting to Orowan looping for larger particle radii [43,44]. A heterogeneous distribution of MC-type carbides (typically TiC) are also found in this alloy, but this distribution does not change with aging and their contribution to the strength of Monel K-500 is considered to be minimal [43].

Five lots of Monel K-500 were evaluated in this work. The first lot was obtained from ATI Allvac (termed Allvac) as a 15.9 mm diameter bar that was hot worked and then age hardened as follows: 16 h at 866K, cooled at 14K/h to 755K, and then air cooled to ambient temperature. Three lots of Monel K-500 were harvested from retired engineering components (intact components that were roughly 305 x 51 x 38 mm in size). The exact service conditions for the components are not known, but are estimated as roughly 10-15 years of full immersion in seawater with exposure to applied potentials likely ranging from -1000 to -750 mV<sub>sce</sub>. These lots are termed Component 1 (TR 1), Component 2 (TR 2), and Component 3 (TR 3) and have an unknown processing history.<sup>12</sup> The final lot of Monel K-500 was received from the U.S. Naval Research Laboratory (NRL) with thermal processing designed to capture the upper-bound strength requirement of QQ-N-286. This material (termed NRL-High Strength (NRL-HS)), was processed from a 114 mm diameter bar procured from Special Metals that was direct-aged at 866 K for 16 h, furnace cooled at 14 K/h to 811 K, held for 1 h, furnace cooled at 14 K/h to 755 K, held for 1 h, and air cooled to ambient temperature. Table 1 presents both the QQ-N-286 composition requirements and the measured bulk chemical compositions for each lot; concentrations of trace elements S, P, Sn, Zr, Mg, Hf, and Pb were determined using glow discharge mass spectrometry. Measured mechanical properties are reported in Table 2; the yield strength and Ramberg-Osgood flow rule constants were determined from compression loading of cylindrical specimens to 2% total strain.

## 2.2 Fracture Mechanics-Based HEAC Testing

### 2.2.1 Mechanical Loading and Crack Monitoring

Single edge notch tensile (SEN(T)) specimens were machined from each of the material lots with gauge sections of 12.5 mm (10.6 mm for Allvac) in width (W), and 2.68 mm in thickness (B). Specimens were loaded parallel to the bar/component longitudinal axis with the Mode I crack growth occurring in the radial direction. An initial  $200 \pm 10 \mu\text{m}$  notch was placed in the center of the gauge section using

---

<sup>12</sup> HEAC testing of the component specimens were performed in the as-received conditions. A companion study suggests that H-charging that occurred during field service may lead to a total internal H-concentration,  $C_{\text{H-total}}$ , on the order of 5 wppm which is similar to the 6 wppm at the crack tip at -850 mV<sub>sce</sub> for the Allvac material lot [18]. The effects of the precharged hydrogen is discussed in more detail elsewhere [124]. However, HEAC testing of the component specimens in an inert environment did not show H-enhanced IG cracking due to the precharged H-content.

electrical discharge machining (EDM). Specimens were fatigue precracked in laboratory air using the following protocol: (1) constant maximum load (12.5 kN) at  $R = 0.1$  from the initial notch to a crack length of  $\sim 0.4$  mm (ending  $K_{\max} \approx 15$  MPa $\sqrt{\text{m}}$ ) and (2) constant  $R = 0.1$  with  $K_{\max}$  decreasing from 15 MPa $\sqrt{\text{m}}$  to a final value of 13 MPa $\sqrt{\text{m}}$  at a crack length of approximately 1 mm. All specimens were loaded in clevis grips to allow for free rotation in compliance with K-solution boundary conditions [45].

Active crack length feedback coupled with software-controlled servo-hydraulic actuator displacement enabled fracture mechanics testing at a constant increasing elastic  $K$  ( $dK/dt$ ). Testing in NaCl solution was conducted at a constant  $dK/dt = 0.33$  MPa $\sqrt{\text{m/hr}}$ , which corresponds to an approximate grip velocity of  $2 \times 10^{-6}$  mm/s, while inert environment testing was completed at a constant  $dK/dt$  of either 0.33 or 1 MPa $\sqrt{\text{m/hr}}$  to limit test duration. Crack progression was monitored via dcPD and the grip velocity was adjusted every 5 seconds to maintain the desired  $dK/dt$ . This procedure included current-polarity reversal to eliminate thermally-induced voltages, crack potential difference normalization by a remote reference, and active-normalized potential values averaged in groups of 50. Each potential measurement was converted to a crack length via Johnson's equation [46], where the potential associated with the initial notch depth ( $a_0$ ) is the adjustable constant ( $V_0$ ) [47]. The resolvable average crack extension,  $\Delta a$ , for this technique is 0.5  $\mu\text{m}$ , based on the ability to resolve 0.1  $\mu\text{V}$  changes in measured potential for a constant applied current of  $4.000 \pm 0.005$  A. Post-test initial crack length measured via electron microscopy typically varied  $<5\%$  from the dcPD-based calculated value. If necessary, the initial crack length was corrected to match the measured value from fractography and all subsequent crack measurements were recalculated using the measured voltage at each time step. The crack growth rate ( $da/dt$ ) at each crack length and time combination was determined using the incremental ( $n=3$ ) polynomial method described in ASTM E647-13 Appendix X1 [48]. High-resolution crack growth monitoring for environment-material combinations that are resistant to HEAC is complicated by plasticity-based resistivity increases, which establish a functional resolution limit of 0.2 to 1 nm/s, depending on the applied  $K$  and  $dK/dt$  [18]. False  $da/dt$  were observed at low  $K$  due to crack surface electrical contact enabled by the cathodic polarization-induced destabilization of the surface oxide film; a post-test analysis protocol (as detailed elsewhere [18]) was used for data correction. The effects of specimen plasticity are accounted for using the J-integral procedure to calculate a total stress intensity ( $K_J$ ). Remaining ligament plasticity was evaluated via analytical solutions for a stationary crack in a material that deforms according to the Ramberg-Osgood flow rule and the effective crack length ( $a_{\text{eff}}$ , taken as the physical crack length plus the plain strain plastic zone correction). Full details of this approach are presented elsewhere [49].

Testing and material response complexities can cause deviations from the classic  $da/dt$  vs.  $K$



behavior, i.e. an initial absence of crack growth below  $K_{TH}$  that is followed by a steep rise in  $da/dt$  with increasing  $K$ , ultimately reaching a  $K$ -independent (Stage II) growth rate ( $da/dt_{II}$ ). As such, it is necessary to assign conditions for determining  $K_{TH}$  and  $da/dt_{II}$ . For the current study,  $K_{TH}$  is defined as the  $K$  at which the growth rate exceeds the plasticity-based resolution limit of the dcPD system (as discussed in [18]) and the Stage II crack growth rate is defined as the  $da/dt$  at  $K = 60 \text{ MPa}\sqrt{\text{m}}$ .

### 2.2.2 Testing Environment

Three test environments were investigated at 23°C: full immersion in an aqueous chloride electrolyte with an applied potential of either  $-950$  or  $-850 \text{ mV}_{SCE}$  and dry  $N_2$  gas ( $RH < 5\%$ ). Prior efforts suggest that the HEAC susceptibility in these environments is aggressive, mild, and inert, respectively [18]. To contain the environment, the gauge section of the SEN(T) specimens was placed inside a 340 mL cylindrical Plexiglass cell. Immersion testing was completed by circulating 0.6 M non-deaerated NaCl solution from a 4L reservoir at  $\sim 20 \text{ mL/min}$  in ambient conditions. Testing was completed at constant applied potentials of  $-850$  and  $-950 \text{ mV}$ , referenced to a standard calomel electrode (SCE) controlled by a potentiostat operated in floating mode (to avoid a ground loop). The SEN(T) specimen was grounded through grip attachment to the testing machine. A platinum-coated Nb mesh counter-electrode and the SCE were placed in the cell, with the counter-electrode surrounding the specimen. Prior to onset of mechanical testing, the open circuit potential of the specimen was monitored for 1 hour, followed by the specimen being polarized to the selected test potential. The bulk solution pH was found to rise from 6.0 to between 6.2-6.5 during an experiment. Only a 1 mm window surrounding the Mode I crack path from the notch to an  $a/W$  of 0.7 was exposed to solution; all other surfaces within the cell were masked with 3M Electroplating Tape 470 and a butyl rubber-based lacquer (Tolber Micro XP-2000 Stop-off Lacquer). Gas testing was completed by flowing  $N_2$  into the environmental cell at a rate that maintained a measured relative humidity of less than 5% for the duration of loading. Upon test completion, each specimen was rinsed with deionized water, sonicated in acetone and methanol for 10 minutes each, and then stored in a desiccator.

### 2.3 Characterization

Scanning electron microscopy (SEM) was performed to identify the final precrack length and to examine the fracture morphology. Orientation imaging microscopy (OIM) was completed for each lot using electron backscatter diffraction (EBSD) with a 30 kV accelerating voltage and a 7.6 nA probe current. EBSD samples were extracted from the non-gauge portion of the SEN(T) specimens, mechanically polished to  $0.10 \mu\text{m}$ , and then vibratory polished using  $0.05 \mu\text{m}$  alumina suspension. A  $0.5 \mu\text{m}$  step size was employed to ensure  $>10$  steps for the smallest grains observed. The resulting OIM maps



were then analyzed using the Tango post-processing software (Oxford Instruments) to evaluate grain boundary misorientation character and average grain size.

Hydrogen interactions were characterized through determination of hydrogen evolution reaction kinetics,  $C_{H,diff}$ ,  $C_{H,tot}$ , and trap binding energy using well-developed procedures [25,50,51]. Specifically, the hydrogen evolution reaction kinetics (HER) were studied through electrochemical interrogation [25,50–52] and the total and diffusible hydrogen concentrations, hydrogen diffusion rates ( $D_{eff}$ ), and trap binding energies were determined using electrochemical, thermal emission (LECO) and thermal desorption methods, respectively [51].

## Results

### 3.1 Quantification of Cracking Behavior

#### 3.1.1 Inert Environment Testing

The  $da/dt$  versus  $K_I$  results for Allvac, TR1, TR2, TR3, and duplicate NRL-HS tests in a dry nitrogen gas environment ( $RH < 5\%$ ) are shown in Figure 1. Consistent with prior results for Allvac material [18], each lot demonstrated two regimes of behavior. First,  $da/dt$  was found to increase linearly with increasing  $K_I$  over a range of low  $K_I$  ( $10 < K_I < 35 \text{ MPa}\sqrt{\text{m}}$ ). This behavior has been attributed to a crack tip plasticity-induced change in resistivity that scales with applied  $K$  and increases the dcPD-measured potential [18]. Thus, it is possible to establish a false  $da/dt$  “resolution limit”, as discussed elsewhere [18], which is described by the following relationship for Allvac tested at a  $dK/dt$  of  $1 \text{ MPa}\sqrt{\text{m/hr}}$  (solid line in Figure 1):  $\log[da/dt_{FALSE} (\text{mm/s})] = -6.3009 + 0.0127 K_I (\text{MPa}\sqrt{\text{m}})$ . Since the plastic zone size depends on both  $K$  and yield strength [53], it is expected that the magnitude of false dcPD rise due to crack tip plasticity effects will be independent of the applied loading rate. Therefore, the resolution limit should scale linearly with applied  $dK/dt$ , with a  $dK/dt$  of  $0.33 \text{ MPa}\sqrt{\text{m/hr}}$  simply being a three-fold reduction of the  $1 \text{ MPa}\sqrt{\text{m/hr}}$  resolution limit. Despite lot-to-lot differences in yield strength, this is shown to be reasonably accurate by comparing tests conducted at a constant  $dK/dt$  of  $0.33 \text{ MPa}\sqrt{\text{m/hr}}$  in dry nitrogen with the predicted  $0.33 \text{ MPa}\sqrt{\text{m/hr}}$  resolution limit (dashed line in Figure 1). Subsequent plots will report the resolution limit specific to the  $dK/dt$  used for data generation.

The second regime of behavior is typified by crack growth above the plasticity-induced resolution limit at  $K_I$  values greater than  $35 \text{ MPa}\sqrt{\text{m/hr}}$ . For all material lots, SEM fractography confirmed 100-200  $\mu\text{m}$  of real sub-critical transgranular/ductile crack extension isolated to the center, high-constraint portion of the specimens, as shown for inert environment-tested TR2 in Figure 2a. This extension occurs well

below the reported ranges of  $K_{IC}$  for Monel K -500 (198-340 MPa $\sqrt{m}$  [18]) and significantly exceeds the  $\sim 25 \mu m$  that would be expected for crack tip blunting (calculated at a  $K_I$  of 80 MPa $\sqrt{m}$  [18]). The dimpled, ductile crack progression in the center of the specimen (Figure 2b, right) was distinct from the morphology in the precrack region (left). High magnification imaging of the dimple features associated with the slow sub-critical cracking on the Allvac and TR2 fracture surfaces (Figure 2c and 2d, respectively) demonstrates that the microvoid-based failure initiated at precipitates. Though compositional analysis of the precise particle composition via energy-dispersive X-ray spectroscopy (EDS) is complicated by the particle size being less than the probe interaction volume, comparing EDS data from the particles to that of the base material demonstrated a clear increase in Ti and C, suggesting that these particles are TiC-type carbides [43,44]. Dey *et al.* observed a roughly 300 nm  $\gamma'$ -precipitate free zone (PFZ) proximate to the TiC precipitates that is facilitated by local Ti and vacancy depletion [43]. It has been postulated that the observed sub-critical ductile crack advance is governed by a thermally-activated dislocation glide mechanism in the PFZ [54]. Analysis of a deformation-mechanism map for pure Ni suggests that, at ambient temperature (23°C) and high stresses (as pertinent to a crack tip), enhanced dislocation glide (which is not true time-dependent creep behavior) is active [55]. This enhanced dislocation mobility becomes increasingly important as the flow stress decreases with loading rate. Furthermore, this mechanism may be augmented by an H-contribution from either residual internal H or low levels of crack tip production due to residual moisture in the dry  $N_2$  and/or H production at mild cathodic polarizations [54].

### 3.1.2 Aqueous Chloride Electrolyte Testing

#### 3.1.2.1 Applied Potential of $-950 \text{ mV}_{SCE}$

The  $da/dt$  versus  $K_I$  data for Allvac, TR1, TR2, TR3, and duplicate NRL-HS tests in 0.6 M NaCl at an applied potential of  $-950 \text{ mV}_{SCE}$  are presented in Figure 3. The Allvac, TR 1, TR 2, TR 3, and NRL-HS material lots show measured  $K_{TH}$  values of 29, 14, 18, 19, and 15/17 MPa $\sqrt{m}$ , respectively. All  $K_{TH}$  values are closely clustered together for this testing condition, with the exception of Allvac, whose higher threshold value suggests an increased resistance to HEAC. This threshold stress intensity is similar to a previous reported value of 30 MPa $\sqrt{m}$  at  $-934 \text{ mV}_{SCE}$  for the Allvac lot [18]. Stage II crack growth rates (at  $K = 60 \text{ MPa}\sqrt{m}$ ) of  $7.2 \times 10^{-6}$ ,  $3.8 \times 10^{-6}$ ,  $2.7 \times 10^{-6}$ ,  $4.6 \times 10^{-6}$ , and  $2.6 \times 10^{-6}/2.8 \times 10^{-6} \text{ mm/s}$  were observed for Allvac, TR 1, TR 2, TR 3, and NRL-HS, respectively. The variation by a factor of 3 between lots is within the expected growth rate scatter established via five replicate tests of a single lot of Monel K-500 in 0.6 M NaCl at  $-1000 \text{ mV}$ ; specifically, a 4-fold variation in  $da/dt_{II}$  was observed [56]. The current growth rates are lower than the previously reported  $da/dt_{II}$  of  $1.9$  to  $2.3 \times 10^{-5} \text{ mm/s}$  at  $-1000$

$mV_{SCE}$  and  $1.1 \times 10^{-5}$  mm/s at  $-900 mV_{SCE}$  for Allvac [18]. However, the current  $da/dt_{II}$  data is reported at  $K_I$  of 60 MPa $\sqrt{m}$  for a  $dK/dt$  of 0.33 MPa $\sqrt{m/hr}$ , whereas prior work reported values for  $K_I$  of 50 MPa $\sqrt{m}$  for a  $dK/dt$  of 1.1 MPa $\sqrt{m/hr}$  [18]. While observed slower growth rates for Allvac in the current work may be attributed to test-to-test scatter, they are directionally consistent with prior results in H-producing environments that show increasing  $dK/dt$  can enhance HEAC susceptibility in Ni-based alloys [18], steels [57], and Ti-6Al-4V [58].

Fractography (each at roughly a  $K_I$  of 40 MPa $\sqrt{m}$ ) shown in Figure 4 demonstrates that flat IG cracking is the dominant fracture morphology for each material during slow-rising displacement testing in 0.6M NaCl at an applied potential of  $-950 mV_{SCE}$ . However, NRL-HS also showed distinct transgranular (TG) features, along with dimpling on some IG facets (Figure 4e-f). Each image was taken at the same magnification, therefore different feature sizes reflect differences in grain size between material lots. High magnification images (Figure 5) reveal slip traces on the fracture surface IG features for each material. A detailed study of the density, spacing, and surface step height was not performed for each specimen, but a coarse observation suggests that the features were generally similar between materials. The slip behavior for Monel K-500 (and the resulting strength and hardening behavior) is largely governed by the size of the homogeneously-distributed  $\gamma'$  precipitates and is critically dependent on the processing history [43,44]. Furthermore, prior efforts have shown a correlation between the spacing of the slip traces on the IG fracture feature with TEM characterization of the dislocation cell structure underneath the fracture surface, suggesting a potentially critical effect of bulk slip behavior on the controlling HEAC damage mechanism [31,59]. Despite the differences in the yield strength reported in Table 2, this coarse observation of similarity in the IG facet slip traces does not suggest a strong variation in the  $\gamma'$  and slip interaction (i.e. the relative amount of shearing and looping). A detailed study of the effect of  $\gamma'$  morphology on the HEAC behavior is ongoing, but in the context of the current effort, similar bulk slip behavior amongst the material lots is inferred from the morphology in Figure 5 and similar hardening behavior (Table 2).

### 3.1.2.2 Applied Potential of $-850 mV_{SCE}$

Severe H-producing environments will give rise to sufficiently high crack tip H-concentrations ( $C_{H-\sigma}$ ) such that any effect of lot-to-lot variation in metallurgy on HEAC susceptibility may be masked by the strong propensity for IG-HEAC. Therefore, it is advantageous to investigate the effect of metallurgy-based variations in the HEAC behavior by testing at applied potentials that produce a lower level of  $C_{H-diff}$ . Prior work established an empirical relationship between diffusible hydrogen concentration and the applied potential for Monel K-500 by utilizing artificial crevice geometries pertinent to current LEFM

experiments. These experiments demonstrated that, for an applied potential of  $-850 \text{ mV}_{\text{SCE}}$ , the value of  $C_{\text{H-Diff}}$  generated in the crack tip environment is  $<10 \text{ wppm}$  [18,25]. As such, the HEAC kinetics were established at this less negative potential ( $-850 \text{ mV}_{\text{SCE}}$ ) in  $0.6 \text{ M NaCl}$  for each material lot.

The  $da/dt$  versus  $K_I$  data for duplicate Allvac, TR1, TR2, TR3, and duplicate NRL-HS tests in  $0.6 \text{ M NaCl}$  at an applied potential of  $-850 \text{ mV}_{\text{SCE}}$  are presented in Figure 6. The TR1, TR 2, and TR 3 material lots all had similar  $da/dt_{II}$  crack growth rates of  $2.2 \times 10^{-6} \text{ mm/s}$ ,  $4.0 \times 10^{-6} \text{ mm/s}$ , and  $3.8 \times 10^{-6} \text{ mm/s}$  at a  $K_I$  of  $60 \text{ MPa}\sqrt{\text{m}}$  with  $K_{\text{TH}}$  values of 17, 42, and  $24 \text{ MPa}\sqrt{\text{m}}$ , respectively. Macroscale fractography of TR 2 shows the smooth EDM notch (Figure 7a, far left), the in-air fatigue precrack region that consisted of TG-slip based cracking ending at the dotted line, transitioning to mixed IG/TG crack progression along the entire crack front during the slow-rising displacement testing to the solid line, followed by final ductile failure. The mixed IG/TG morphology observed during loading at an applied potential of  $-850 \text{ mV}_{\text{SCE}}$  in  $0.6 \text{ M NaCl}$  is shown at a  $K_I$  of roughly  $40 \text{ MPa}\sqrt{\text{m}}$  in Figure 7b, 7c, and 7d, for TR1, TR 2, and TR 3, respectively. This morphology is consistent with slow-rising displacement testing of Monel K-500 where mild cathodic polarizations resulted in identical IG/TG crack growth [18]. The  $da/dt$  vs.  $K_I$  data for Allvac (replicate tests) and NRL-HS (replicate tests) specimens show growth rate behavior that is similar to the inert dry  $\text{N}_2$  results, as demonstrated in Figure 8a for NRL-HS. Furthermore, fractography confirmed the presence of the same macroscale morphology for NRL-HS and Allvac at  $-850 \text{ mV}_{\text{SCE}}$  (e.g. Figure 8b) as was observed for inert dry  $\text{N}_2$  testing (e.g. Figure 2a). A slight variations in morphology was observed between Allvac (small dimpled features) and NRL-HS (dimpled ridge-like structure, Figure 8c) at higher magnifications. Speculatively, this variation is attributed to an increased level of hydrostatic stress in NRL-HS causing secondary cracks to form perpendicular to the crack plane. Regardless, these findings suggest that no IG-HEAC occurred in these specimens, therefore  $K_{\text{TH}}$  and  $da/dt_{II}$  are not reported for the Allvac and NRL-HS lots. The inconsistency in the HEAC susceptibility amongst material lots can be interpreted as either (1) variability that is inherent to testing in a potential regime where minor changes in local crack environment result in orders of magnitude changes in HEAC susceptibility [18], or (2) metallurgy-specific characteristics that shift the critical potential where HEAC susceptibility initiates. The former is treated in a companion paper [52] and the latter will be developed in the Discussion.

### 3.2 Characterization of the Grain Structure

Orientation maps colored according to the indicated inverse pole figure are presented for each material in Figure 9a-e with grain boundaries highlighted as black lines. The results of an ASTM E112-113 grain size analysis are reported in Table 3, along with the calculated grain boundary surface area to volume ratio ( $S_v$ ;  $\text{mm}^2/\text{mm}^3$ ) [60,61]. For polycrystalline materials, the IG-HEAC behavior is influenced



by the prevalence of certain special boundaries (low angle and coincident site lattice boundaries (CSL)) and the degree of high angle boundary connectivity [62–64]. The OIM of a representative  $0.05 \text{ mm}^2$  area of each material is used to quantify the distribution of high angle ( $>15^\circ$ ), low angle ( $>5^\circ$  and  $\leq 15^\circ$ ), and CSL boundaries. The resolution of the analysis enabled characterization of orientation variations within grains (attributed to sub-grain crystal distortions and dislocation structures [65]), though for clarity in the intergrain misorientation analysis and grain size calculations, the orientation of each grain was averaged using the Tango software and misorientation angles below  $5^\circ$  were not included in the analysis. The fraction of (1) the total number of boundaries and (2) the total Sv that are low energy (including random boundaries  $<15^\circ$  and CSL boundaries) range from 53-61% and 53-64%, respectively (Table 3), with the vast majority of low energy boundaries being  $\Sigma 3$  boundaries. Despite this seemingly small range, the differences in grain size give rise to a drastic variation in the total Sv of low energy boundaries between material lots, which may be important in the context of the susceptible path connectivity [62,63]. For example, 43 and 44% of the Sv are high energy boundaries in Allvac and TR 2, but grain size differences ( $13.8$  and  $35.3 \text{ }\mu\text{m}$ , respectively) result in the total Sv of high energy boundaries being  $162 \text{ mm}^2/\text{mm}^3$  for Allvac and  $70 \text{ mm}^2/\text{mm}^3$  for TR2.

### 3.3 Quantification of Hydrogen Interaction Parameters

Evaluating the effect of hydrogen interactions requires the examination of many parameters. These include hydrogen evolution kinetics to address differences in H production and adsorption, hydrogen concentration, hydrogen diffusion rates, and trap binding energies. The segregation of trace elements to the grain boundary is also of interest due to their potential to promote increased hydrogen activity and/or lower  $C_{H,crit}$  [66], as well as lower intrinsic fracture strength or toughness [25,67,68]. The kinetics of the hydrogen evolution reaction were studied by measuring the Tafel slope and exchange current densities for water reduction (hydrogen evolution) in  $0.6 \text{ M NaCl}$  at  $\text{pH } 8.0$ . Production rates were similar among the different materials; lot-to-lot variation does not affect this parameter. Figure 10 displays the effect of hydrogen overpotential on hydrogen concentration where both concentration parameters were found to increase with increasing hydrogen overpotential. As expected, the total hydrogen concentration  $C_{H,Total}$  was larger than  $C_{H,Diff}$  [25]. In terms of lot-to-lot variation, there was limited difference between both  $C_{H,Total}$  and  $C_{H,Diff}$ , except for the Allvac material, which consistently exhibited hydrogen concentration near the lower bound of all other heats or statistically lower hydrogen levels based on repeat measurements at some potentials. Variation in diffusible hydrogen concentrations could arise from hydrogen interacting with low and high binding energy traps, such as: dislocations [69,70], grain boundaries, carbides [71], microvoids, age hardening precipitates (e.g.  $\gamma'$ ) [25,69,72], among others. Two trap binding states were found in all the heats tested; these results are



in agreement with previous information reported on solution heat treated (SHT), aged and SHT, cold worked, aged Monel K-500 materials [25]. The average values for the binding energies for  $\gamma'$  were found in the range 7.8 to 17.7 kJ/mol in the following ascending order: NRL-HS < TR 2 < Allvac. Changes in trap binding energy would result in lot-to-lot differences in the hydrogen diffusion coefficient, which would critically affect the proposed HEAC behavior (as quantified in Eqn 3). However, prior analysis found similar hydrogen diffusion coefficients (in the range  $0.9\text{-}3.9 \times 10^{-14} \text{ m}^2/\text{s}$ ) for all materials, suggesting a secondary role of trapping/diffusion on lot-dependent HEAC behavior [25,52].

## Discussion

The crack growth kinetics (Figure 1, 3, 6) and cracking morphologies (Figure 4, 8) demonstrate that, in both inert (dry  $\text{N}_2$  gas) and aggressive (0.6 M NaCl polarized to  $-950 \text{ mV}_{\text{SCE}}$ ) environments, the sub-critical cracking behavior shows little variation in HEAC susceptibility between different lots of Monel K-500. However, at mildly aggressive environments (0.6 M NaCl polarized to  $-850 \text{ mV}_{\text{SCE}}$ ) where low crack tip H-uptake is expected [18], a noticeable change in fracture morphology is observed. Specifically, the Allvac and NRL-HS lots demonstrate a ductile transgranular (TG) cracking morphology in the high constraint center of the specimen, while TR1, TR2, and TR2 show both a mixed TG/IG morphology and crack growth kinetics consistent with a HEAC-based mechanism. This discussion will augment the fracture mechanics testing results with detailed materials characterization data and mechanism-based modeling to provide insight into three primary questions: (1) Can the potential dependence of the observed lot-to-lot variation be rationalized in the context of a hydrogen embrittlement mechanism? (2) To what extent do various material lot-dependent characteristics (yield strength, composition, grain boundary character, H-metal interactions, and impurity segregation) correspond with the observed changes in the HEAC susceptibility for mildly aggressive environments? (3) Can the differences in microstructure be incorporated into micromechanical modeling to capture the observed variation in HEAC susceptibility?

### 4.1 Effect of Microstructure Variations at Mild and Aggressive Applied Potentials

Decohesion-based micromechanical models (Eqn. 2 and 3) provide a quantitative framework for understanding the extent to which variations in material properties will influence HEAC metrics ( $K_{\text{TH}}$  and  $da/dt_{\text{II}}$ ) at different applied potentials. Specifically, this framework can be utilized to inform why all material lots demonstrate similar HEAC susceptibility at  $-950 \text{ mV}_{\text{SCE}}$ , while significant differences are observed for materials tested at  $-850 \text{ mV}_{\text{SCE}}$ . The justification and validation of the micromechanical modeling approach was established in prior work [18] and has been recently refined [54]. For current

modeling, the input parameters for  $K_{TH}$  modeling are  $\sigma_{YS} = 786$  MPa (Allvac),  $\alpha'' = 0.0002$  MPa $\sqrt{m}$ , and  $\beta' = 0.20$  (MPa $\sqrt{m}$ )<sup>-1</sup> (based on dislocation-shielding simulations of the near crack tip stress field [32,73] and validated by experimental data on IN718 [37,54]).  $C_{H-\sigma}$  is calculated from Eqn. 1, where  $\sigma_H = 9\sigma_{YS}$  and an empirical relationship relates the applied potential to  $C_{H-Diff}$  for the Allvac material [18].  $k_{IG}$  is the Griffith toughness of the IG interface, calculated to be 0.88 MPa $\sqrt{m}$  using the Griffith relation and theoretical values of the surface energy of Ni [54].  $\alpha$  represents the potency of the local H in decreasing  $k_{IG}$  and is set to 4.078 (MPa $\sqrt{m}$  per atom fraction H) to fit the model to the average of three Allvac  $K_{TH}$  values (established from previous work as 18 MPa $\sqrt{m}$  [18]) at an applied potential of  $-1000$  mV<sub>SCE</sub>. The model-predicted effect of applied potential on the  $K_{TH}$  of Allvac is reported in Figure 11a-c (solid black lines) using the parameters detailed above.

The relative influence of microstructural variation at different applied potentials can be evaluated by systematically varying input parameters that may exhibit lot-to-lot differences. Though details regarding the link between the modeling parameters and microstructure features will be established later in the discussion, a sensitivity analysis is useful to demonstrate the effect of such changes on HEAC behavior. Three modeling parameters are varied in the current  $K_{TH}$  modeling. First, the sensitivity of the models to variations in H uptake behavior is evaluated by multiplying and dividing the calculated  $C_{H-Diff}$  by 2.5 (corresponding to a 250% increase and a 60% decrease). This 250% increase in uptake behavior is physically realistic for Monel K-500 [18] and is supported by the present analysis (Figure 10) which indicates lower  $C_{H-Diff}$  in Allvac for a given applied potential [52]. Figure 11a clearly demonstrates that increasing/decreasing  $C_{H-Diff}$  results in a more pronounced variation in  $K_{TH}$  as the applied potential is increased from  $-950$  to  $-850$  mV<sub>SCE</sub>. For example, increasing  $C_{H-Diff}$  by 250% (Figure 11a, thick solid blue line) results in a decrease of  $K_{TH}$  by 61 MPa $\sqrt{m}$  at  $-850$  mV<sub>SCE</sub> whereas a decrease of only 15 MPa $\sqrt{m}$  is calculated for  $-950$  mV<sub>SCE</sub>. Similarly, the changes in  $K_{TH}$  are again more severe at  $-850$  mV<sub>SCE</sub> when the intrinsic grain boundary toughness ( $k_{IG}$ ) is varied  $\pm 25\%$  with all other inputs at the baseline levels, as shown in Figure 11b. Physically, such variations in grain boundary toughness could result from differences in the fraction of high energy boundaries or boundaries containing significant concentration of deleterious impurity atoms. Decreasing  $k_{IG}$  from 0.88 to 0.66 MPa $\sqrt{m}$  (Figure 11b, thick solid blue line) results in a  $K_{TH}$  decrease of 62 and 14 MPa $\sqrt{m}$  for  $-850$  and  $-950$  mV<sub>SCE</sub>, respectively. Finally, the  $-850$  mV<sub>SCE</sub> condition is significantly more sensitive to a  $\pm 15\%$  change in  $\sigma_{YS}$  (Figure 11c, thick solid blue line); an increase in  $\sigma_{YS}$  from 786 to 904 MPa results in a 65 and 16 MPa change in  $K_{TH}$  for  $-850$  and  $-950$  mV<sub>SCE</sub>, respectively. Critically, this variation in yield strength represents the difference between the Allvac and NRL HS lots, as shown in Table 2, illustrating the large change in HEAC resistance that could be expected in this alloy.

A similar micromechanical modeling-based sensitivity analysis was performed to understand how changes in microstructure may influence  $da/dt_{II}$  at different applied potentials. The baseline parameters for current modeling mimic those in prior work [18,54], where  $D_{eff} = 1 \times 10^{-10} \text{ cm}^2/\text{s}$ ,  $x_{crit} = 1 \text{ }\mu\text{m}$ ,  $C_{H-\sigma}$  is calculated in the same manner as in the  $K_{TH}$  modeling, and  $C_{H-Crit}$  is set to 647 wppm [54]. The baseline model (Figure 12a-b; black solid line) demonstrates HEAC growth rates increase several orders of magnitude as the potential is decreased from approximately -840 to 900  $\text{mV}_{SCE}$ ; however, further reduction of the potential from -900 to -1100  $\text{mV}_{SCE}$  results in a minimal increase in  $da/dt$ . This behavior is understood in the context of the abundant supply of crack-tip H at the low potentials, whereas at higher potentials there is insufficient supply of H to enable embrittlement. The sensitivity of this behavior to varying metallurgical features can be quantitatively evaluated by varying the hydrogen uptake behavior and yield strength inputs in Eqn 3; the  $D_{eff}$  and  $x_{crit}$  parameters are considered invariant with regards to microstructure [18,25]. To evaluate the sensitivity of the model to variations in hydrogen uptake, the diffusible hydrogen concentration was again increased 250% and decreased 60% (Figure 12a-b, thick solid blue line and dashed line, respectively). As demonstrated by Figure 12a, the difference in  $da/dt_{II}$  significantly increases amongst the three calculated curves when moving from -950 to -850  $\text{mV}_{SCE}$ , suggesting that the effect of metallurgical variations is more discernible at higher potentials. This same behavior is noted when varying the yield strength  $\pm 15\%$ ; specifically, the effect of yield strength variation on  $da/dt_{II}$  is more pronounced at less negative applied potentials. These observations can be rationalized in the context of strong cathodic polarizations leading to a level of crack-tip H that greatly exceeds the critical value required for cracking (i.e.  $C_{H-crit}$ ). Therefore, any variation in material HEAC resistance will only marginally influence the cracking behavior at -950  $\text{mV}_{SCE}$ , while HEAC susceptibility becomes more material-dependent as the applied potential increases to -850  $\text{mV}_{SCE}$ .

*In toto*, a sensitivity analysis using previously validated models for  $K_{TH}$  and  $da/dt_{II}$  (Eqn 2 and 3, respectively) clearly establishes that microstructure-based changes in material properties are expected to have an increasing effect on HEAC susceptibility at applied potentials that produce lower crack-tip H concentrations. These results are consistent with experimental observations of minimal lot-to-lot variation in the HEAC behavior at -950  $\text{mV}_{SCE}$  (Figure 3-5) and significant lot-dependent HEAC behavior at -850  $\text{mV}_{SCE}$  (Figure 6-8). Taken together, these experimental and micromechanical modeling results demonstrate that microstructural influences can alter HEAC susceptibility with the caveat that these deviations are attenuated when environmental conditions become severe. Furthermore, these finding reinforce the need to accurately capture environmental conditions when performing engineering-scale modeling so as to ensure reliable predictions.

#### 4.2 Correlation of Microstructure Features with HEAC Susceptibility

The susceptibility of Ni-based alloys to IG H-embrittlement has been found to scale with yield strength [74], grain size [75–77], grain boundary (GB) character [30,62,78], and composition [79–81]. Isolating the relative influence of each feature is challenging for complex engineering alloys, especially when the material processing history is uncertain. Quantitative characterization of each characteristic enables correlation of measured properties with observed HEAC behavior, thereby providing an opportunity to elucidate dominant features. The following section seeks to connect the measured variation in material properties with the observed HEAC susceptibility found for each material lot.

#### 4.2.1 Material Composition

The basic composition of Monel K-500 consists of roughly 66 wt% Ni and 30 wt% Cu, augmented by the addition of ~3 wt% Al and 0.6 wt% Ti to enable further strengthening via precipitation of the  $\gamma'$ -phase [82]. Trace impurity elements can have significant effects on creep resistance, weldability, corrosion resistance, and mechanical properties in Ni-based alloys and must be controlled to optimize material performance [79,80,83]. Specifically, impurity elements (e.g. O, H, N, Ar, He, S, P, Pb, Bi, Sb, As, Se, Ag, Cu, Tl, Te) have been broadly characterized as deleterious to the material properties of Ni and/or Ni-based alloys [79,84]. For the current work, no clear trend of trace S, P, Pb, Ag, or Sb content and HEAC resistance was observed, though higher levels of As (and marginally Bi and Te) were found in the more susceptible TR 1, TR2, and TR3 materials. These subtle differences are likely not sufficient to deleteriously influence properties, especially considering the minute bulk impurity levels [79,84]. However, there is a broad literature which demonstrates that elements such as Bi, Te, Pb, S, B, C, Zr, Hf, P, Mg, and Ta have an affinity for segregating to GBs, giving rise to local concentrations well above what is observed in the bulk [80,85,86]; this segregation can magnify the influence of variations in the trace element content. The degree of segregation is dependent on the element and the grain boundary misorientation [63,87,88], as well as the concentration of intentionally added getter elements (e.g. Mg, Zr, Hf, C) which retard the segregation of deleterious elements to the GB. Of critical importance to the IG-HEAC behavior is the (direct or indirect) effect of these impurity and trace elements on the grain boundary susceptibility to (chemo-)mechanical failure.

While elemental C segregation to GBs has been shown to be innocuous [89] or even beneficial [90] in Ni alloys, Natishan *et al.* suggest that a semi-continuous, thin film of unalloyed C may contribute to the IG failure of Monel K-500 in hydrogen [91,92]. This film was sporadically observed along grain boundaries and is likely in the form of graphite, similar to what has been reported for Nickel 200 after prolonged exposures to 425–650°C [93]. In the context of present results, Table 1 demonstrates that the more susceptible TR1 and TR2 have increased levels of C, but this is conflicted by HEAC-



susceptible TR3 having less C content than the immune Allvac lot. However, prior researchers found that the prevalence of the film does not scale with the bulk carbon content, but instead is dependent on applied thermal processing [92]. In this paradigm, a composition/processing variation that failed to produce a graphite film would then be responsible for the lack of IG cracking in Allvac and NRL-HS. Therefore, the mixed IG/TG features observed for TR1, TR2, and TR3 (Figure 7) at  $-850 \text{ mV}_{\text{SCE}}$  could be due to this graphite film-induced IG failure as opposed to HEAC. However, this conjecture is not consistent with the ductile/transgranular morphology that is observed for all alloys in the dry  $\text{N}_2$  environment or other low H environment testing presented in companion work [54]. According to Natishan *et al.*, the graphite film-enhanced IG susceptibility of Monel K-500 was most pronounced at low H conditions, while inhibiting HEAC susceptibility at higher H concentrations [91,92], which directly contradicts the current experimental results (Figures 3-6). As such, this graphite film-based mechanism is not considered to be a source of the current lot-to-lot variation.

Sulfur (where segregation can give rise to GB concentrations over 2000-fold higher than bulk levels [79,94,95]) is widely considered to be the dominant deleterious segregant for Ni-based alloys [64,79,96]. Similar deleterious behavior was postulated for P, which also strongly segregates to GBs [79], however experimental [97] and theoretical [89] results establish that P is either inert or even beneficial in Ni-based alloys [80]. Using either quantum mechanical cluster calculations [89,98] or a local spin density atomic cluster model [99], researchers have postulated that the electronegativity of S changes the local chemical bonding structure to decrease the GB cohesive properties [64]. Additionally, the embrittling effect of sulfur has been found to be synergistic with that of H [66,90,96,100], which suggests that lot-to-lot variations in sulfur segregation/gettering may impact HEAC susceptibility. There is a modest correlation between increased bulk S content (Table 1) and HEAC susceptibility (Figures 6-8), though it is complicated by the HEAC-resistant NRL-HS material having 5 times the S content (17 wppm) of the susceptible TR1 material (3.1 wppm). However, the rigor of correlating bulk S content to the GB cracking susceptibility is compromised by: (1) the presence of getter elements that will strongly influence the concentration of S available for segregation, (2) the grain boundary surface area available for segregation, and (3) the presence of trace elements that are known to increase the cohesive strength of the GB interface.

Since getter elements have a high affinity to react with S [101], they will preferentially form sulfides (Mg, Ca, Zr [79,102]) and/or sulfo-carbides (Zr, Hf [86,103]), which reduce the S available for segregation to the grain boundaries. Thus, to quantify the influence of these getter elements on the HEAC resistance, it is critical to understand the degree to which they reduce the sulfur available for segregation. Yamaguchi *et al.* developed a relationship to describe the reduction of available sulfur for minor additions

of getter elements (Ca, Mg, Y, and Zr) [104]; this relationship was scaled to experimental measurements of hot-workability and Auger analysis of grain boundary S for a variety of Ni-based superalloys. Rigorously applying this model to Monel K-500 to quantify the reduction of tramp residual S concentration is complicated by alloy differences and focus on the hot-workability in model development. However, the Yamaguchi approach can be used to qualitatively evaluate the influence of the variation in getter element composition (Table 1) on HEAC resistance. The original relationship proposed by Yamaguchi is modified in two ways to calculate the effective gettering power (via a total weighted composition,  $C_{\text{Get}}$ ) of each alloy. First, Hf is included with the same weighting factor as Zr based on the proposed similarity of solubility product for Hf and Zr [101]. Second, the Ca term is eliminated since the Yamaguchi study (and others that report a gettering effect of Ca [105]) explicitly doped the Ni-based alloys with elemental Ca, whereas the Ca concentration reported in Table 1 is likely in the form of residual CaO (or potentially CaS) not removed with the slag during the desulphurization process [106]. While at molten conditions, CaO will effectively remove elemental S, but CaO is chemically stable at all known processing temperatures and is not expected to act as a getter of tramp residual S [107]. The resulting relationship is:

$$C_{\text{Get}} = 0.3\text{Mg} + 0.1\text{Zr} + 0.1\text{Hf} \quad (\text{Eqn 4})$$

where elemental designations represent the respective bulk concentrations in a consistent unit (e.g. wt%, wppm, etc). The resulting  $C_{\text{Get}}$  values are 49, 75, 73, 72, and 77 wppm for Allvac, TR1, TR2, TR3, and NRL-HS, respectively. Higher values of  $C_{\text{Get}}$  are found to not scale with decreased HEAC susceptibility, thereby suggesting that an additional influence outside of getter element composition exists.

For a given bulk impurity level, the concentration of GB segregants will decrease with shrinking grain size due to the increase in available surface area per volume of grain boundary; this behavior has been experimentally established for Ni-based alloys [76,85]. Normalizing the bulk S values listed in Table 1 by the lot specific GB surface area per volume values (Table 3) results in nominally lower values for materials that are more HEAC resistant (0.0046 (Allvac) and 0.042 (NRL-HS) wppm/(mm<sup>2</sup>/mm<sup>3</sup>)) and higher values for more susceptible materials (0.074 and 0.075 wppm/(mm<sup>2</sup>/mm<sup>3</sup>) for TR2 and TR3, respectively). This suggests that grain size may play a tangible role in determining HEAC susceptibility, even though TR1 (0.012 wppm/(mm<sup>2</sup>/mm<sup>3</sup>)) does diverge from that trend. One plausible explanation for this deviation is that the effect of the high S content of NRL-HS may be offset by having the highest effective gettering power; specifically, the high  $C_s/S_v$  would be mitigated by gettering elements. Regardless, these tentative observations are supported by preliminary Auger analysis of fracture surface GB features from H-charged slow strain rate testing of notched bar samples, where S enhancement was

observed for all materials, but grain size per volume and gettering element concentrations vary [52]. A more thorough Auger analysis is ongoing to quantitatively evaluate the interaction of bulk S composition, grain size, and gettering elements on the deleterious GB segregation of S.

GB segregants can also have the beneficial effect of raising HEAC resistance. In particular, B has been experimentally [108] and theoretically [64,85,89,99,109] shown to increase the cohesive strength of the GB. It has also been postulated that Zr will have a beneficial intrinsic effect on GB cohesion [103], however such a beneficial effect (above the gettering efficiency of Zr) is not widely accepted [79,80]. The materials that have the highest bulk B levels (Allvac; 3.8 wppm, NRL-HS; 2.0 wppm) in Table 1, correlate with higher observed HEAC resistance (Figure 6); this trend also holds true for bulk Zr concentrations (Allvac; 370 wppm, NRL-HS; 650 wppm). However, no correlation is found with observed HEAC resistance when the bulk B concentration is normalized by  $S_v$ , as the susceptible TR2 and TR3 lots have a higher value than that observed for NRL HS. The unknown potency and the relative concentration of B that segregates to the GB (rather than forming borides [108]) precludes conclusive and quantitative understanding of the extent to which such small changes (0.5-1.5 wppm) in bulk B content will impact the HEAC resistance.

*In toto*, the compositional analysis above demonstrates that the materials that exhibit enhanced HEAC resistance (Allvac and NRL-HS) have the lowest bulk S content per surface area/volume of GB and the highest bulk B (and Zr) levels, however there is no clear trend with the combined calculated gettering power of Mg, Zr, and Hf. These qualitative trend comparisons reasonably suggest a potentially important role of S segregation differences and/or segregation of GB-strengthening elements in determining HEAC susceptibility. A full compositional analysis of the observed GB particles, complete Auger analysis of the GB composition, and establishing the potency of each trace element to either getter, embrittle, or enhance properties are needed, but outside the scope of the current effort. Regardless, this analysis provides a reasonable basis to conclude that changes in impurity and trace element concentrations likely contribute to (but do not dominate) the varying HEAC susceptibility between different lots of Monel K-500.

#### 4.2.2 Grain Boundary Characteristics

##### 4.2.2.1 Grain Size

The current data (Table 3 and Figure 9) demonstrate that materials with larger grains (TR1, TR2, TR3) are more susceptible to HEAC cracking than smaller grained materials (Allvac and NRL-HS). There are varying reports of the effect of grain size on HEAC behavior; increasing grain size has been

reported to decrease susceptibility [110,111], while others report HEAC behavior being independent of size variation [112]. Isolation of the intrinsic effect of grain size is complicated by the interdependence of other properties with grain dimensions; specifically, strength, H-trapping/solubility behavior [77,113], GB impurity segregation [76], crack path dependent mechanics [114], and/or susceptible crack path connectivity [111].

Stress intensity reductions due to increasing crack deflection away from the Mode I path with increasing grain size have been shown to increase fatigue cracking thresholds and decreased crack growth rates in the slow cracking (less than  $10^{-6}$  mm/ cycle) [114–116]. The following relationship was proposed to describe the effective stress intensity of a deflected crack ( $K_{Def}$ ):

$$K_{def} = K \frac{D \cos^2\left(\frac{\theta}{2}\right) + S}{D + S} \quad (\text{Eqn 5})$$

where D is the distance over which the tilted crack advances, S is the span of the non-deflected Mode I crack, and  $\theta$  is the angle of deflection [114]. Large grain sizes would reasonably lead to increased D and S values, resulting in a  $K_{def}/K$  ratio of less than 1. Average values of D and S were measured from the random, high angle grain boundary maps of each material lot (except NRL HS) and are listed in Table 3. The maximum angle of deflection was found to be 60 degrees and was similar for all materials, which results in a measured  $K_{def}/K$  of 0.82, 0.82, 0.77, and 0.81 for Allvac, TR1, TR2, and TR3, respectively. As was expected, the largest grain size material (TR2, 35.3  $\mu\text{m}$ ) had the largest amount of deflection and the lowest  $K_{def}/K$  ratio. When the magnitude of decrease in K is evaluated amongst the material lots, the lot-to-lot variation in  $K_{TH}$  is too large to be solely due to crack deflection. Specifically, accounting for deflection results in an approximate 20% reduction of  $K_{TH}$  in each lot, which is insignificant given the large difference in measured  $K_{TH}$  for Allvac and TR1 at -950 mV<sub>SCE</sub> and the total lack of IG-HEAC for Allvac and NRL-HS at -850 mV<sub>SCE</sub>. Therefore, crack deflection-induced differences in K are not considered to be the dominant source of lot-to-lot variation in HEAC susceptibility.

#### 4.2.2.2. Grain Boundary Connectivity

Researchers have established that the grain boundary character (misorientation, interface energy, and structure) will significantly influence the IG cracking susceptibility in a wide range of structural metals by influencing the cohesive strength, segregation/depletion behavior, and slip behavior [62,63,113]. Critically, certain low-energy “special” boundaries are more resistant to the failure mechanisms pertinent to HEAC; these boundaries include grain boundaries of low misorientation ( $15^\circ$  or less) and coincident site lattice (CSL) boundaries of  $1 < \Sigma < 29$  [75,117]. Both the number and  $S_v$  fraction of low energy (CSL and low angle  $<15^\circ$ ) GBs are similar for all materials, ranging from 53-62% with no



discernable trend regarding HEAC. Percolation theory has been used in the context of IG stress corrosion cracking (SCC) to correlate the prevalence of susceptible boundaries to the probability of having a fully connected, continuous susceptible crack path [62,118]. Such an approach assumes a binary distribution of either fully susceptible (high angle) or immune GBs (low angle or CSL), based on the misorientation angle, thereby ignoring any gradients in susceptibility due to other microstructural considerations. Regardless, percolation analysis estimates that the threshold fraction of resistant grains necessary to disrupt a connected path are >11% for IG/TG mix and >77% for fully ductile TG (via a 3D analysis of a tetrakaidecahedron geometry [118]), 35% (unconstrained 2D analysis of a hexagonal array [119,120]), and 50% (2D analysis of both a microstructurally constrained hexagonal array [120]). Based on these percolation theory thresholds and the limited range of low energy boundaries for all materials (53-62%), there is no clear evidence to support the variation in HEAC resistance being due to differing low energy boundary interruptions of the continuous susceptible crack path.

While the percolation theory approach provides insightful correlations between the percentage of susceptible boundaries and the probability of a connected path, sole reliance on the percent of resistant boundaries fails to account for potential grain size influences. For example, despite similar percentages (43 and 44%) of the Sv being high energy in Allvac and TR 2, grain size differences (13.8 and 35.3  $\mu\text{m}$ , respectively) result in the total Sv of high energy boundaries of the two lots being drastically different: 162  $\text{mm}^2/\text{mm}^3$  for Allvac and 70  $\text{mm}^2/\text{mm}^3$  for TR2. A fractal analysis of connectivity provides a means to understand the influence of these grain size effects on the availability of a susceptible crack path by quantifying the fractal dimension ( $D_R$ ) of the path of maximum connectivity network (MCN) using a box-counting method [75].

The boundary misorientation angles are characterized via OIM analysis of each material (Figure 9); these data can be used to trace the maximum connectivity network (MCN) of random, susceptible, high angle boundaries. This process is illustrated for the Allvac material in Figure 13. Figure 13a presents the OIM map (with averaged grain orientations) and an inverse pole figure. From these data, traces of the random (black; misorientation angle  $>5^\circ$ ) and CSL (various colors) are then identified (Figure 13b). The high angle boundaries ( $>15^\circ$ ) are extracted (Figure 13c) and a computer program is used to identify the MCN (red lines in Figure 13d) for each material lot. For this MCN analysis, two data points were considered connected if they were adjacent or  $<2$  pixels apart (thus  $<1 \mu\text{m}$ ), so that short non-indexed paths along the grain boundary do not affect the connectivity analysis. This  $1 \mu\text{m}$  threshold is physically justified based on comparisons to  $x_{\text{crit}}$  (proposed to be  $\sim 1 \mu\text{m}$  [40]); specifically, an advancing crack along a random, high angle grain boundary would not likely be arrested by an anomalous segment of “special” boundary shorter than  $x_{\text{crit}}$ . The MCN is then overlaid with a square grid, each box of side

length  $\eta$  ( $\eta=12.5, 25$ , or  $50 \mu\text{m}$ ). For each box size ( $\eta$ ), the number of boxes containing part of the MCN ( $N(\eta)$ ) is quantified. The fractal dimension of the MCN ( $D_R$ ) is the metric by which the connectivity is evaluated [75] and is defined as:

$$D_R = -\frac{\log[N(\eta)]}{\log[\eta]} \quad (\text{Eqn 6})$$

Higher values of  $D_R$  reflect greater connectivity of the random, susceptible high angle grain boundaries [75]. As such, this approach enables a quantitative comparison of random, high angle grain boundary connectivity for each Monel K-500 material lot. To provide the greatest accuracy, the range of  $\eta$ -values are on the scale of the grain sizes observed for Monel K-500, consistent with prior arguments and application of this fractal analysis approach [75,121,122].

The fractal dimensions are reported in Table 3 and show no clear correlation between increased connectivity (high  $D_R$ ) and increased HEAC susceptibility, thereby suggesting that lot-to-lot differences in crack path connectivity do not govern the observed variability in HEAC behavior. For example, Allvac and NRL-HS shows the highest and third highest  $D_R$ , yet neither exhibit IG-HEAC at  $-850 \text{ mV}_{\text{SCE}}$  (Figure 8). The role of grain size on the crack path connectivity is illustrated in Figure 14 by plotting the  $D_R$  versus both the  $S_V$  fraction of low energy boundaries and the  $S_V$  value of high angle boundaries. The data do not show a correlation between increasing fraction of low angle boundaries and  $D_R$  (thus connectivity) for materials with different grain sizes. However, there is a reasonable correlation of increasing connectivity with increasing  $S_V$  of high angle boundaries. This demonstrates that, for varying grain size materials, the fractional values of resistant low energy boundaries (nor high energy susceptible boundaries) are not an accurate proxy for the degree of crack path connectivity, rather the true value of  $S_V$  is governing. It has been controversially postulated that such behavior may be caused by  $\Sigma 3$  boundaries playing a marginal role in disrupting the network of susceptible boundaries due to their formation in the grain interior, which would fail to disrupt a susceptible path [120].

#### 4.3 Hydrogen Interactions

Previous work found different diffusible hydrogen concentrations as a function of applied potential in two Monel K-500 lots, thereby suggesting that the relationship between the diffusible hydrogen concentration (thus the stress-enhanced concentration,  $C_{\text{H-}\sigma}$ , via Eqn 1) and applied potential may vary amongst the material lots [18]. This variation is confirmed by the differences in measured  $C_{\text{H-Diff}}$  found for three lots (Allvac, NRL-HS, and TR2) at hydrogen overpotentials ranging from  $-0.85$  to  $-1.1 \text{ V}_{\text{SCE}}$  (Figure 10). A lower value of  $C_{\text{H-Diff}}$  leads to a concomitant reduction of  $C_{\text{H-}\sigma}$  for a given hydrogen

overpotential. Moreover, the hydrogen coverage at grain boundaries in the fracture process zone for a heat-invariant grain boundary trap binding energy would be reduced by the lower  $C_{H,Diff}$ ; though it should be noted that grain boundary trap states are difficult to distinguish from the  $\gamma'$  trap state, which is the subject of future work [52]. A decrease in  $C_{H,Diff}$  would increase HEAC resistance (as demonstrated in Figure 10) by slowing accumulation of the H concentration required to nucleate crack growth,  $C_{H\sigma-crit}$ . This change in H-material interaction would interact with the previously discussed lot-to-lot differences (e.g. S segregation, gettering element content, and/or high grain boundary surface to volume ratio altering the  $k_{IG}$  and  $C_{H\sigma-crit}$ ) to influence the material specific HEAC behavior. These speculations could be reinforced by better assessment of elemental sulfur and gettering levels and trap binding energies for high- and low-angle boundaries.

#### 4.4 Modeling $K_{TH}$ for Lot-to-Lot Variations in Yield Strength and Composition

The results of the sensitivity analysis shown in Figure 11a-c demonstrates that significant variations in  $K_{TH}$  can arise from realistic lot-to-lot changes in yield strength, grain boundary toughness, and hydrogen uptake behavior. Furthermore, the discussion presented herein has suggested a potentially important role for impurity segregation to grain boundaries in determining a material lot's HEAC susceptibility, specifically with regards to the deleterious effect of sulfur and the beneficial effect of boron. In the following section, the  $K_{TH}$  model (Eqn. 2) is leveraged to predict the HEAC behavior of the five material lots; this effort will use previously developed modeling parameters [18] along with material lot specific inputs as a basis to propose model improvements that incorporate the effects of impurity segregation to GBs.

Predicted  $K_{TH}$  versus  $E_{app}$  results for Allvac, TR1, TR2, TR3, and NRL-HS are shown in Figure 15 using previously validated parameters for the Allvac material ( $\alpha'' = 0.0002 \text{ MPa}\sqrt{m}$ ,  $\beta' = 0.20 \text{ (MPa}\sqrt{m})^{-1}$ ,  $k_{IG} = 0.88 \text{ MPa}\sqrt{m}$ , and  $\alpha = 4.078 \text{ MPa}\sqrt{m}/(\text{atm frac H})$  [18,54]) and each material's respective yield strength (Table 2). As expected, the variation in yield strength amongst the material lots (and its effect on the local hydrostatic stress) give rise to drastic differences in calculated threshold values as the applied potential is increased. However, as shown by the experimental results plotted alongside the predicted curves, the previously validated modeling parameters are not able to fully capture the effect of microstructure changes on HEAC susceptibility. In particular, the NRL-HS is predicted to be the most susceptible of the five lots (blue dashed line), but was found to be immune to HEAC when experimentally tested at  $-850 \text{ mV}_{SCE}$ , as shown by the black arrow extending upward. This deviation from experimental results could be rooted in the influence of sulfur and boron on the grain boundary toughness,  $k_{IG}$ ; especially with regards to NRL-HS which has the highest bulk sulfur content. To further explore the

effect of impurity segregation, we make two assumptions: (1) any effect of impurity elements on  $k_{IG}$  occurs prior to H exposure and (2) sulfur and boron are the only two elements influencing the GB toughness. This leads to the following modification of Eqn. 2:

$$K_{TH} = \frac{1}{\beta'} \exp \left[ \frac{((k_{IG} - \beta C_S + \gamma C_B) - \alpha C_{H\alpha})^2}{\alpha'' \sigma_{YS}} \right] \quad (\text{Eqn 7})$$

Where  $\beta$  (MPa $\sqrt{m}/(\text{atm frac S})$ ) and  $\gamma$  (MPa $\sqrt{m}/(\text{atm frac B})$ ) are the weighting factors that define how effectively sulfur and boron alter  $k_{IG}$ ,  $C_S$  and  $C_B$  are the concentrations of sulfur and boron at the grain boundary, and all other variables are defined as in Eqn 2. To predict the concentrations of boron and sulfur at an arbitrary grain boundary, the Auger analysis of Ladna and Birnbaum were used to estimate the amplification of the bulk concentration [108]. These amplifications (48,000x and ~1,270x for S and B, respectively) were linearly scaled to reflect differences in grain size between the original and current study, resulting in final amplifications of approximately 180x and 3x in NRL-HS (for S and B, respectively).  $C_S$  and  $C_B$  were calculated for each material lot, along with the previously calculated  $C_{H\alpha}$ , and then  $\alpha$ ,  $\beta$ , and  $\gamma$  were fit to minimize the square of the difference between the calculated  $K_{TH}$  and the experimentally measured  $K_{TH}$  for each lot at  $-950 \text{ mV}_{SCE}$ , where lot-to-lot variations in metallurgy should have minimal effect. From this analysis,  $\alpha = 4.167 \text{ (MPa}\sqrt{m}/(\text{atm frac H})\text{)}$ ,  $\beta = 2.753 \text{ (MPa}\sqrt{m}/(\text{atm frac S})\text{)}$ , and  $\gamma = 4.12 \times 10^{-4} \text{ (MPa}\sqrt{m}/(\text{atm frac B})\text{)}$ , which suggests that boron has minimal effect on grain boundary toughness.

Calculated  $K_{TH}$  versus  $E_{app}$  using the newly fit parameters are shown in Figure 16 for Allvac, TR1, TR2, TR3, and NRL-HS, along with experimental results for  $-950$  and  $-850 \text{ mV}_{SCE}$ . Despite a noticeable shift in the results, especially at less cathodic potentials, a significant difference in theoretical and experimental results still exists. Critically, several deficiencies in the fidelity of the data inputs need to be addressed before the efficacy of this modeling approach can be determined, specifically: (1) inaccurate estimates of sulfur and boron concentrations at the grain boundary, (2) lack of specific data on the effect of gettering elements on sequestering sulfur in Monel K-500, and (3) lack of specific hydrogen uptake relationships for non-Allvac lots. Physically, the proposed alterations to Eqn 2 are reasonable, as sulfur and boron have been shown, both experimentally and theoretically, to impact grain boundary cohesion [79,108,109,123]. Improvements to the modeling would therefore be based on gathering data specific to the alloy of interest so as to ensure that unique factors are accurately captured. Specifically, Auger analysis of GBs in each lot as a function of applied heat treatment would provide an accurate GB amplification factor for boron and sulfur, while also addressing questions regarding the efficiency of gettering elements. Further still, understanding the specific hydrogen uptake relationship for each material



is critical to accurately estimating the stress-enhanced hydrogen concentration in the FPZ. As demonstrated in Figure 11a, realistic changes in uptake behavior can have drastic influences on the calculated threshold values.

Finally, a variation in modeling parameter dependencies, especially regarding the dependence on yield strength, has been found for different materials and should be evaluated in detail for the Ni-based alloys. Specifically, a less severe dependence of  $K_{TH}$  on yield strength was found for Mo ( $\exp(\sigma^{-1/2})$ ) as compared to the original Fe-3%Si solution ( $\exp(\sigma^{-1})$ ) [73]. However, previous efforts have shown that values predicted using Eqn 2 were in excellent agreement with experimental results [18,54], suggesting that other influences may be dominating.

## Conclusions

The influence of microstructure variation on hydrogen environment-assisted cracking of Monel K-500 are evaluated using five nominally peak-aged lots of material (all of which satisfy the QQ-N-286 specification) tested under slow-rising stress intensity loading while immersed in NaCl solution under cathodic polarizations. Quantitative HEAC parameters were established using fracture mechanics testing and were coupled with a detailed characterization of the microstructure (e.g. composition, grain character analysis, and H-metal interaction parameters.) The results of these analyses are coupled with micromechanical models to quantitatively evaluate how observed changes in the microstructure relate to the resulting HEAC behavior. The following conclusions are established.

- Limited lot-to-lot variation in HEAC susceptibility was observed in five peak-aged Monel K-500 lots when immersed in 0.6M NaCl under an applied potential of  $-950$  mVSCE during slow-rising K testing, suggesting minimal influence of metallurgical variation in severe H-producing environments.
- Extensive lot-to-lot variation in both HEAC metrics ( $K_{TH}$  and  $da/dt_H$ ) and fractography was observed amongst the material lots when immersed in 0.6 M NaCl under an applied potential of  $-850$  mVSCE during slow-rising K testing.
- The influence of metallurgical features, including grain size, impurity segregation, grain boundary character and connectivity, gettering element composition, and crack path tortuosity were evaluated. Of these, yield strength and impurity segregation are considered to be the most influential in determining HEAC resistance.

- The degree of impurity segregation is critically influenced by the grain size, inclusion of gettering elements, and the bulk concentration of both beneficial (e.g. B) and deleterious (e.g. S) elements.
- Sensitivity analysis of the decohesion-based, micromechanical models suggests that physically realistic variations in hydrogen uptake behavior, yield strength, and intrinsic grain boundary toughness give rise to large changes in HEAC susceptibility.
- Predicted values of  $K_{TH}$  did not align with experimental results when previously validated modeling parameters were employed, suggesting that the current models need to be extended to more accurately capture the effect of lot-to-lot variations in microstructure.
- A modification to  $K_{TH}$  model was proposed to incorporate the effect of impurity segregants, resulting in new modeling parameters. Correlation between experimental and predicted values were compromised by uncertain inputs regarding the degree of grain boundary segregation. Ongoing efforts will establish these parameters to provide a more rigorous evaluation.

### **Acknowledgements**

This research was sponsored by ONR Grant N00014-12-1-0506 with Dr. Airan Perez as Scientific Officer. Helpful discussions with Prof. Richard Gangloff and fracture mechanics testing by Ms. Christina Kaminsky are gratefully acknowledged.

## References

1. NACE Standard MR0175-1998. "Sulfide Stress Cracking Resistant Metallic Materials for Oilfield Equipment." Houston, TX: NACE, 1998
2. ASTM Standard G30, 1997 (2009), "Standard Practice for Making and Using U-Bend Stress-Corrosion Test Specimens," ASTM International, West Conshohocken, PA, 2009.
3. ASTM Standard G39, 1999 (2011), "Standard Practice for Preparation and Use of Bent-Beam Stress-Corrosion Test Specimens," ASTM International, West Conshohocken, PA, 2011.
4. ASTM Standard G129, 2000 (2013), "Standard Practice for Slow Strain Rate Testing to Evaluate the Susceptibility of Metallic Materials to Environmentally Assisted Cracking," ASTM International, West Conshohocken, PA, 2013.
5. ASTM Standard E1681, 2003 (2013), "Standard Test Method for Determining Threshold Stress Intensity for Environment-Assisted Cracking of Metallic Materials," ASTM International, West Conshohocken, PA, 2013.
6. ASTM Standard F1624, 2012, "Standard Test Method for Measurement of Hydrogen Embrittlement Threshold in Steel by the Incremental Step Loading Technique," ASTM International, West Conshohocken, PA, 2012.
7. R. E. Butler: in *Engineering with Copper-Nickel Alloys*, Metals Society, London, 1988, pp. 79–84.
8. C. A. Clark, S. Driscoll, and P. Guha: *Br. Corros. J.*, 1992, vol. 27, pp. 157-60.
9. G. A. Scott: in *17<sup>th</sup> Offshore Technology Conference*, Paper No. OTC 5050, Houston, 1985.
10. R. N. Tuttle and A. W. Thompson: *Control of Hydrogen Embrittlement in Deep Gas Wells*, Metallurgical Society AIME, United States, 1976.
11. L. H. Wolfe and M. W. Joosten: *SPE Prod. Eng.*, 1988, vol. 3, pp. 382-86.
12. J. R. Scully and M. G. Vassilaros: "The Hydrogen Embrittlement Susceptibility of Monel Alloy K-500," presented at the Electrochemical Society Fall 1983 Meeting, Washington, D.C., 1983.
13. R. D. Bayles, T. Lemieux, F. Martin, D. Lysogorski, T. Newbauer, W. Hyland, B. A. Green, E. Hogan, and P. Stencil: *Naval Surface Treatment Center MR2010 Proceedings Presentation*, 2010.
14. L. H. Wolfe, C. C. Burnette, and M. W. Joosten: *Mater. Perform.*, 1993, vol. 32, pp. 14-21.
15. J. A. Lillard: Ph.D Dissertation, University of Virginia, Charlottesville, VA, 1998.
16. W. K. Boyd and W. E. Berry: "Stress Corrosion Cracking Behavior of Nickel and Nickel Alloys," in *Stress Corrosion Cracking of Metals - A State Art, ASTM STP 518*, American Society for Testing and Materials, 1972, pp. 58–78.
17. R. P. Gangloff: "Hydrogen Assisted Cracking of High Strength Alloys," in *Comprehensive Structural Integrity*, I. Milne, R. O. Ritchie, and B. Karihaloo, eds., Elsevier, New York, NY, 2003, pp. 31–101.
18. R. P. Gangloff, H. M. Ha, J. T. Burns, and J. R. Scully: *Metall. Mater. Trans. A*, 2014, vol. 45, pp. 3814-34.
19. R. P. Gangloff: "Critical Issues in Hydrogen Assisted Cracking of Structural Alloys," in *Environment Induced Cracking of Metals*, S.A. Shipilov, R.H. Jones, J.-M. Olive, and R.B. Rebak, eds., Elsevier, Oxford, 2006, pp. 6337–49.
20. R. P. Gangloff: *Corrosion*, 2016, in press.
21. J. A. Harter: <http://www.afgrow.net/downloads/pdownload.aspx>, 2007.
22. W. A. Grell and P. J. Laz: *Int. J. Fatigue*, 2010, vol. 32, pp. 1042-9.
23. J. Harter: *Int. J. Fatigue*, 1999, vol. 21, pp. S181-5.
24. R. P. Gangloff, D. C. Slavik, R. S. Piascik, and R. H. Van Stone: "Direct Current Electrical Potential Measurement of the Growth of Small Cracks," in *Small-Crack Test Methods, ASTM STP 1149*, M. Larsen and J. E. Allison, eds., ASTM International, West Conshohocken, PA, 1992, pp. 116-68.
25. J. Ai, H. M. Ha, R. P. Gangloff, and J. R. Scully: *Acta Mater.*, 2013, vol. 61, 3186-99.
26. T. Boniszewski and G. Smith: *Acta Metall.*, 1963, vol. 11, pp.165-78.
27. A. H. Windle and G. C. Smith: *Met. Sci. J.*, 1970, vol. 4, 136-44.
28. D.H. Lassila and H.K. Birnbaum: *Acta Metall.*, 1986, vol. 34, pp. 1237–43.

29. D. M. Symons: *Eng. Fract. Mech.*, 2001, vol. 68, pp. 751–71.
30. S. Bechtle, M. Kumar, B. P. Somerday, M. E. Launey, and R. O. Ritchie: *Acta Mater.*, 2009, vol. 57, pp. 4148–57.
31. M. L. Martin, B. P. Somerday, R. O. Ritchie, P. Sofronis, and I. M. Robertson: *Acta Mater.*, 2012, vol. 60, pp. 2739–45.
32. W. W. Gerberich: in *Gaseous Hydrogen Embrittlement of Materials in Energy Technology*, R.P. Gangloff and B.P. Somerday, eds., Woodhead Publishing, 2012, pp. 209–46.
33. S. P. Lynch: *Metall. Mater. Trans. A*, 2013, vol. 44A, p. 1209–29.
34. S. P. Lynch: *Corros. Rev.*, 2012, vol. 30, pp. 105–23.
35. Y. Katz, N. Tymiak, and W. W. Gerberich: *Eng. Fract. Mech.*, 2001, vol. 68, pp. 619–46.
36. Y. Lee and R. P. Gangloff: *Metall. Mater. Trans. A*, 2007, vol. 38, pp. 2174–90.
37. R. P. Gangloff: in *Hydrogen Effects on Materials*, B. P. Somerday, P. Sofronis, and R. H. Jones, eds., ASM International, Materials Park, OH, 2009, pp. 1–21.
38. W. W. Gerberich, R. A. Oriani, M. Lii, X. Chen, and T. Foecke: *Philos. Mag. A*, 1991, vol. 63, pp. 363–76.
39. U. Komaragiri, S. R. Agnew, R. P. Gangloff, and M. R. Begley: *J. Mech. Phys. Solids*, 2008, vol. 56, pp. 3527–40.
40. R. P. Gangloff: in *Hydrogen Effects on Material Behavior and Corrosion Deformation Interactions*, N. R. Moody and A. W. Thompson, eds., The Minerals, Metals & Materials Society, Warrendale, PA, 2002.
41. *Nickel-Copper-Aluminum Alloy, Wrought (UNS N05500)*, QQ-N-286G: Department of the Navy, 2000.
42. J. R. Davis, ed: in *Nickel, Cobalt, and Their Alloys: ASM Special Handbook*, 2000, pp. 167–88.
43. G. K. Dey and P. Mukhopadhyay: *Mater. Sci. Eng.*, 1986, vol. 84, pp. 177–89.
44. G. K. Dey, R. Tewari, P. Rao, S. L. Wadekar, and P. Mukhopadhyay: *Metall. Trans. A*, 1993, vol. 24, pp. 2709–19.
45. H. Tada, P.C. Paris, and G.R. Irwin: *The Stress Analysis of Cracks Handbook*, Paris Productions Incorporated, St. Louis, MO, 1985.
46. H. H. Johnson: *Mater. Res. Stand.*, 1965, vol. 5, pp. 442–45.
47. K.-H. Schwalbe and D. Hellmann: *J. Test. Eval.*, 1981, vol. 9, pp. 218–21.
48. ASTM Standard E647, 2013, "Standard Test Method for Measurement of Fatigue Crack Growth Rates," ASTM International, West Conshohocken, PA, 2013.
49. V. Kumar, M. D. German, and C. F. Shih: *An Engineering Approach for Elastic-Plastic Fracture Analysis*, Electric Power Research Institute, Palo Alto, CA, 1981.
50. H. M. Ha, J. Ai, and J. R. Scully: *Corrosion*, 2014, vol. 70, pp. 166–84.
51. B. A. Kehler and J. R. Scully: *Corrosion*, 2008, vol. 64, pp. 465–77.
52. B. C. Rincon Troconis, Z. D. Harris, J. T. Burns, and J. R. Scully: *Corrosion*, in preparation 2015.
53. T. L. Anderson: *Fracture Mechanics: Fundamentals and Applications*, 3rd ed., Taylor & Francis, 2005.
54. J. T. Burns, Z. D. Harris, J. D. Dolph, and R. P. Gangloff: "Measurement and Modeling of Hydrogen Environment Assisted Cracking in a Ni-Cu-Ti-Al Superalloy," submitted to *Metall. Mater. Trans. A*, in review.
55. H. J. Frost and M. F. Ashby: *Deformation-Mechanism Maps: The Plasticity and Creep of Metals and Ceramics*, 1st ed., Pergamon Press, Oxford Oxfordshire ; New York, 1982.
56. J. Waldman, R. P. Gangloff, and J. T. Burns: Final Report, STTR Topic No. N08-T010 (Phase II Option I), Navmar Applied Sciences Corporation, Warminster, PA, 2014.
57. K. A. Nibur, B. P. Somerday, C. San Marchi, J. W. Foulk, M. Dadfarnia, and P. Sofronis: *Metall. Mater. Trans. A*, 2013, vol. 44A, pp. 248–69.



58. E. Richey and R. P. Gangloff: in *Environmentally Assisted Cracking: Predictive Methods for Risk Assessment and Evaluation of Materials*, ASTM STP 1401, R. D. Kane, ed., ASTM, West Conshohocken, PA, 2000, pp. 104–27.
59. M. L. Martin, I. M. Robertson, and P. Sofronis: *Acta Mater.*, 2011, vol. 59, pp. 3680–87.
60. ASTM Standard E112, 2013, "Standard Test Methods for Determining Average Grain Size," ASTM International, West Conshohocken, PA, 2013.
61. E. E. Underwood: *Quantitative Stereology*, Addison-Wesley Pub. Co., Reading, Mass., 1970.
62. J. R. Scully: in *Environmentally Assisted Cracking: Predictive Methods for Risk Assessment and Evaluation of Materials*, ASTM STP 1401, R. D. Kane, ed., ASTM, West Conshohocken, PA, 2000, pp. 40–69.
63. T. Watanabe: *J. Mater. Sci.*, 2011, vol. 46, pp. 4095–4115.
64. P. Lejcek: in *Grain Boundary Segregation in Metals*, P. Lejcek, ed., Springer, Berlin, 2010.
65. A. J. Wilkinson, G. Meaden, and D. J. Dingley: *Ultramicroscopy*, 2006, vol. 106, pp. 307–13.
66. C. D. Taylor, M. Neurock, and J. R. Scully: *J. Electrochem. Soc.*, 2011, vol. 158, pp. F36–44.
67. C. L. Briant, H. C. Feng, and C. J. McMahon: *Metall. Trans. A*, 1978, vol. 9, pp. 625–33.
68. G. M. Pressouyre: *Acta Met.*, 1980, vol. 28, pp. 895–911.
69. A. Turnbull, R. G. Ballinger, I. S. Hwang, and M. M. Morra: *Metall. Mater. Trans. A*, 1992, vol. 23.
70. J. P. Hirth: *Metall. Mater. Trans. A*, 1980, vol. 11, pp. 861–90.
71. D. Li, R. P. Gangloff, and J. R. Scully: *Metall. Mater. Trans. A*, 2004, vol. 35, pp. 849–64.
72. J. E. Angelo, N. R. Moody, and M. I. Baskes: *Model. Simul. Mater. Sci. Eng.*, 1995, vol. 3, pp. 289–307.
73. H. Huang and W. W. Gerberich: *Acta Metall. Mater.*, 1994, vol. 42, pp. 639–47.
74. M. R. Louthan, G. R. Caskey, J. A. Donovan, and D. E. Rawl: *Mater. Sci. Eng.*, 1972, vol. 10, pp. 357–68.
75. S. Kobayashi, T. Maruyama, S. Tsurekawa, and T. Watanabe: *Acta Mater.*, 2012, vol. 60, pp. 6200–12.
76. R. M. Latanision and H. Opperhauser: *Metall. Trans.*, 1974, vol. 5, pp. 483–92.
77. A. Oudriss, J. Creus, J. Bouhattate, C. Savall, B. Peraudeau, and X. Feaugas: *Scr. Mater.*, 2012, vol. 66, pp. 37–40.
78. J. R. Scully: *MRS Bull.*, 1999, vol. 24, pp. 36–42.
79. R. T. Holt and W. Wallace: *Int. Met. Rev.*, 1976, pp. 1–24.
80. B. Geddes: in *Superalloys: Alloying and Performance*, B. Geddes, H. Leon, and H. Huang, eds., ASTM International, West Conshohocken, PA, 2010, pp. 59–109.
81. D. A. Woodford: *Energy Mater.*, 2006, vol. 1, pp. 59–79.
82. W. F. Smith: *Structure and Properties of Engineering Alloys*, 2nd ed., McGraw-Hill, New York, 1993.
83. J. N. DuPont, J. C. Lippold, and S. D. Kiser: *Welding Metallurgy and Weldability of Nickel-Base Alloys*, John Wiley & Sons, Hoboken, N.J., 2009.
84. W. B. Kent: *J. Vac. Sci. Technol.*, 1974, vol. 11, pp. 1038–46.
85. E. S. Huron, K. R. Bain, D. P. Mourer, J. J. Schirra, P. L. Reynolds, and E. E. Montero: in *Superalloys 2004*, K. A. Green, T. M. Pollock, H. Harada, T. E. Howson, R. C. Reed, J. J. Schirra, and S. Walston, eds., TMS, 2004.
86. J. M. Walshe, K. P. Gumz, and N. P. Anderson: in *Quantitative Surface Analysis of Materials*, ASTM STP 643, N. S. McIntyre, ed., ASTM, 1978, pp. 72–82.
87. W. Swiatnicki, S. Lartigue, M. Biscondi, and D. Bouchet: *J. Phys. Colloq.*, 1990, vol. 51, pp. 341–46.
88. D. Raabe, M. Herbig, S. Sandlobes, Y. Li, D. Tytko, M. Kuzmina, D. Ponge, and P. P. Choi: *Curr. Opin. Solid State Mater. Sci.*, 2014, vol. 18, pp. 253–61.
89. R. P. Messmer and C. L. Briant: *Acta Metall.*, 1982, vol. 30, pp. 457–67.
90. A. Kimura and H. K. Birnbaum: *Acta Metall.*, 1988, vol. 36, pp. 757–66.

91. M. E. Natishan and M. Wagenhofer: in *Fatigue and Fracture Mechanics: Twenty-Ninth Volume, ASTM STP 1332*, T. L. Panontin and S. D. Sheppard, eds., ASTM, West Conshohocken, PA, 1999, pp. 384–392.
92. M. E. Natishan and W. C. Porr: in *Structural Integrity of Fasteners, ASTM STP 1236*, P. M. Toor, ed., ASTM, Philadelphia, PA, 1995, pp. 81–92.
93. T. S. F. Lee and R. M. Latanision: *Metall. Trans. A*, 1987, vol. 18, pp. 1653–62.
94. W. C. Johnson, J. E. Doherty, B. H. Kear, and A. F. Giamei: *Scr. Metall.*, 1974, vol. 8, pp. 971–74.
95. T. Miyahara, K. Stolt, D. A. Reed, and H. K. Birnbaum: *Scr. Metall.*, 1985, vol. 19, pp. 117–21.
96. R. H. Jones: in *Advances in the Mechanics and Physics of Surfaces*, R. M. Latanision and T. E. Fischer, eds., Hardwood Academic Publishers, Chur, Switzerland, 1986, pp. 1–70.
97. X. Xie, X. F. Liu, J. Dong, Y. Hu, and Z. Xu: in *Superalloys 718, 625, 706 and Various Derivatives*, E. A. Loria, ed., TMS, 1997, pp. 531–542.
98. C. L. Briant and R. P. Messmer: *J. Phys.*, 1982, vol. 43, pp. 255–69.
99. G. S. Painter and F. W. Averill: *Phys. Rev. Lett.*, 1987, vol. 58, pp. 234–37.
100. D. H. Lassila and H. K. Birnbaum: *Acta Metall.*, 1987, vol. 35, pp. 1815–22.
101. C. Sarioglu, C. Stinner, J. R. Blachere, N. Birks, F. S. Pettit, G. H. Meier, and Smiale: in *Superalloys 1996*, R. D. Kissinger, D. J. Deye, D. L. Anton, A. D. Cetel, M. V Nathal, T. M. Pollock, and D. A. Woodford, eds., TMS, 1996, pp. 71–80.
102. P. C. Banerjee and R. K. S. Raman: *Electrochim. Acta*, 2011, vol. 56, pp. 3790–98.
103. H. E. Huang and C. H. Koo: *Mater. Trans.*, 2004, vol. 45, pp. 554–61.
104. S. Yamaguchi, H. Kobayashi, T. Matsumiya, and S. Hayami: *Met. Technol.*, 1979, vol. 6, pp. 170–75.
105. J. J. deBarbadillo: in *Superalloys 1976*, TMS, 1976, pp. 95–107.
106. R. Reed: *The Superalloys Fundamentals and Applications*, Cambridge University Press, 2006.
107. R. W. Smith, W. T. Geng, C. B. Geller, R. Wu, and A. J. Freeman: *Scr. Mater.*, 2000, vol. 43, pp. 957–61.
108. B. Ladna and H. K. Birnbaum: *Acta Metall.*, 1988, vol. 36, pp. 745–55.
109. H. H. Kart and T. Cagin: *J. Achievements Mater. Manuf. Eng.*, 2008, vol. 30, pp. 177–81.
110. N. R. Moody, R. E. Stoltz, and M. W. Perra: *Scr. Metall.*, 1985, vol. 20, pp. 119–23.
111. A. Oudriss, J. Bouhattate, C. Savall, J. Creus, X. Feaugas, F. Martin, P. Laghoutaris, and J. Chene: *Procedia Mater. Sci.*, 2014, vol. 3, pp. 2030–34.
112. J. F. Lessar and W. W. Gerberich: *Metall. Trans. A*, 1976, vol. 7, pp. 953–60.
113. A. Oudriss, J. Creus, J. Bouhattate, E. Conforto, C. Berziou, C. Savall, and X. Feaugas: *Acta Mater.*, 2012, vol. 60, pp. 6814–28.
114. S. Suresh: *Metall. Trans. A*, 1983, vol. 14, pp. 2375–85.
115. R.O. Ritchie and S. Suresh: *Metall. Trans. A*, 1982, vol. 13, pp. 937–40.
116. J. E. King: *Met. Sci.*, 1982, vol. 16, pp. 345–55.
117. M. Seita, J. P. Hanson, S. Gradečak, and M. J. Demkowicz: *Nat. Commun.*, 2015, vol. 6, p. 6164.
118. D. B. Wells, J. Stewart, A. W. Herbert, P. M. Scott, and D. E. Williams: *Corrosion*, 1989, vol. 45, pp. 649–60.
119. V. K. S. Shante and K. Kirkpatrick: *Adv. Phys.*, 1971, vol. 20, pp. 325–57.
120. C. A. Schuh, R. W. Minich, and M. Kumar: *Philos. Mag.*, 2003, vol. 83, pp. 711–26.
121. A. Roy, E. Perfect, W. M. Dunne, and L. D. McKay: *J. Geophys. Res. Solid Earth*, 2007, vol. 112, pp. B12201–9.
122. J. Jabra, M. Romios, J. Lai, E. Lee, M. Setiawan, E. W. Lee, J. Witters, N. Abourialy, J. R. Ogren, R. Clark, T. Oppenheim, W. E. Frazier, and O. S. Es-Said: *J. Mater. Eng. Perform.*, 2006, vol. 15, pp. 601–7.
123. M. Yamaguchi, M. Shiga, and H. Kaburaki: *Mater. Trans.*, 2006, vol. 47, pp. 2682–9.
124. J. Dolph: Master's Thesis, University of Virginia, Charlottesville, VA, 2015.

Table 1 - Chemical Composition of Monel K-500 Lots (wt. %, except S, P, Sn, Pb, Mg, Zr, Hf, B are wppm)

Lot	Ni	Cu	Al	Fe	Mn	Si	Ti	C	Co	S	P	Sn	Pb	Mg	Zr	Hf	B
Allvac	66.12	28.57	2.89	0.80	0.81	0.08	0.45	0.17	0.01	1.60	92	2.4	2.1	39	370	2.6	3.8
NRL-HS	63.44	30.74	3.20	0.91	0.85	0.10	0.57	0.14	0.02	17.00	40	2.2	3.5	40	650	0.8	2.0
TR1	65.55	29.18	2.86	0.93	0.67	0.04	0.47	0.22	0.01	3.10	55	1.2	2.4	170	230	4.6	0.3
TR2	64.66	30.15	2.73	0.69	0.73	0.09	0.45	0.20	0.04	11.00	71	6.9	2.5	130	330	5.6	1.5
TR3	64.17	30.34	3.21	0.71	0.81	0.09	0.45	0.13	0.04	12.00	74	6.8	2.4	130	320	5.4	1.5
QQ-N-286	> 63.0	27-33	2.3-3.15	< 2.0	< 1.5	< 0.50	0.35-0.85	< 0.18	< 0.25	< 60	< 200	< 60	< 60	N/A	N/A	N/A	N/A

Table 2 - Mechanical Properties of Monel K-500 Lots

Lot	$\sigma_{ys}$ (MPa)	E (GPa)	n	$\alpha$
Allvac	786	180	20	0.39
NRL-HS	910	191	18	0.405
TR1	898	183	18	0.39
TR2	795	202	20	0.39
TR3	792	194	20	0.39

Table 3 – Grain Boundary Size and Characteristics of Monel K-500 Lots

Lot	d ( $\mu\text{m}$ )	Sv ( $\text{mm}^2/\text{mm}^3$ )	Low Angle Boundary Fraction (%)	Fractal Dimension, Dr	D ( $\mu\text{m}$ )	S ( $\mu\text{m}$ )
Allvac	13.8	341	57	1.59	10.5	10.8
NRL-HS	11.2	407	62	1.49	N/A	N/A
TR1	25.8	252	60	1.53	17.6	18.3
TR2	35.3	149	56	1.38	23.2	14.0
TR3	31.8	160	53	1.35	24.1	23.4

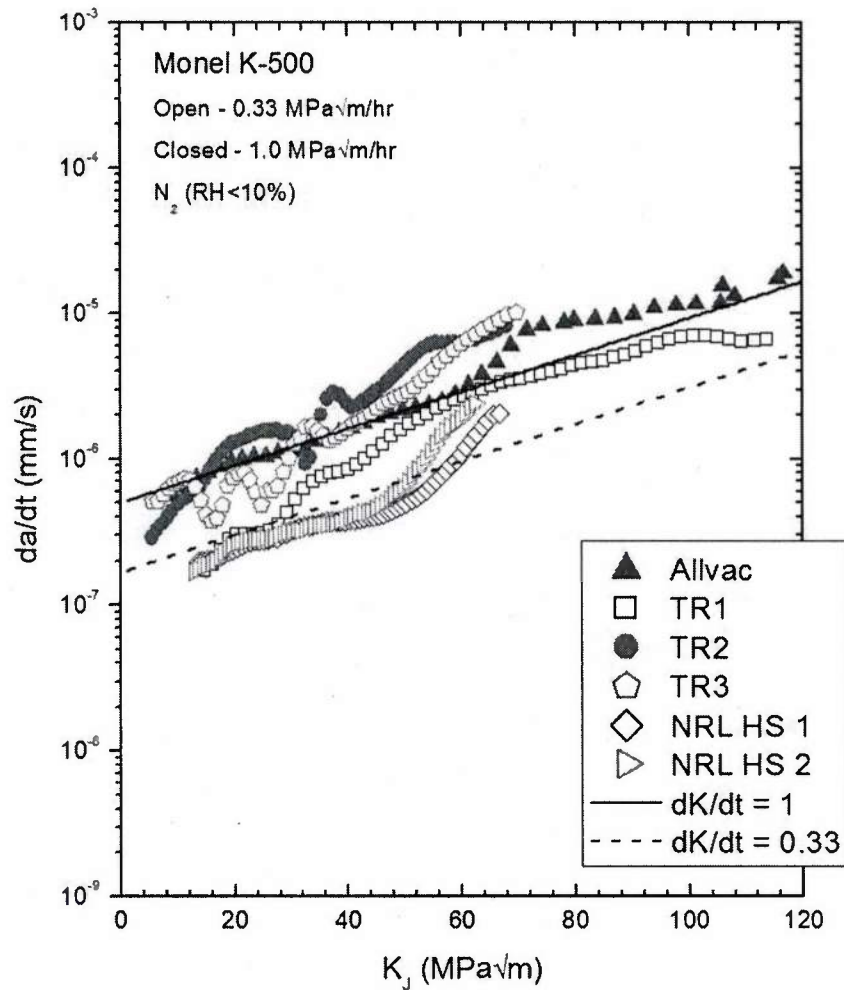


Figure 1 - Crack growth rate versus total  $K$  for five lots of peak-aged Monel K-500 stressed under two different  $dK/dt$  protocols in a dry nitrogen (RH < 5%) environment. Closed symbols represents specimens tested at  $dK/dt = 1$  MPa√m/hr, while open symbols were tested at  $dK/dt = 0.33$  MPa√m/hr. Expected false  $da/dt$  produced by crack tip plastic deformation for each  $dK/dt$  are represented by the solid (1 MPa√m/hr) and dashed (0.33 MPa√m/hr) lines.



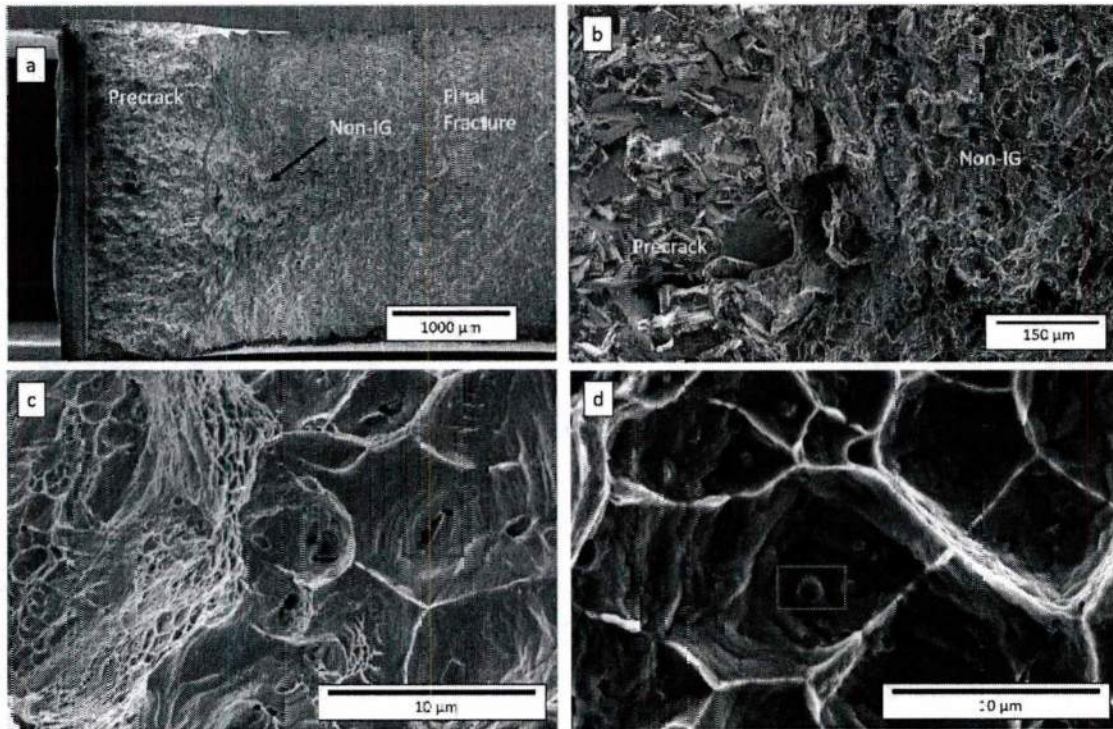


Figure 2 – Fractographs illustrating the (a) dimpled, ductile fracture morphology observed in the center (b) of inert environment-tested specimens. Additional images of (c) Allvac and (d) TR2 show the carbide precipitates (red boxes) found at the base of many microvoidic features.

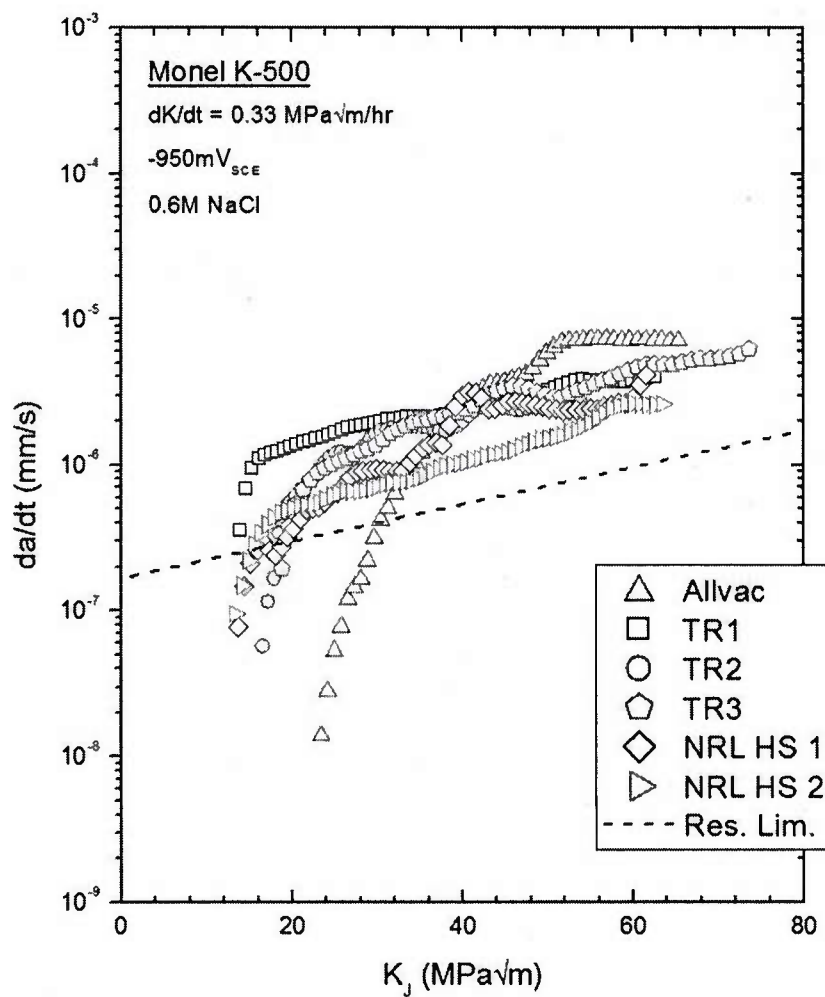


Figure 3 - Crack growth rate versus total K for five lots of peak-aged Monel K-500 stressed in NaCl solution at a constant applied potential of  $-950\text{mV}_{\text{SCE}}$ . The dashed line represents the expected false  $da/dt$  produced by crack tip plastic deformation for  $dK/dt = 0.33 \text{ MPa}\sqrt{\text{m/hr}}$ .

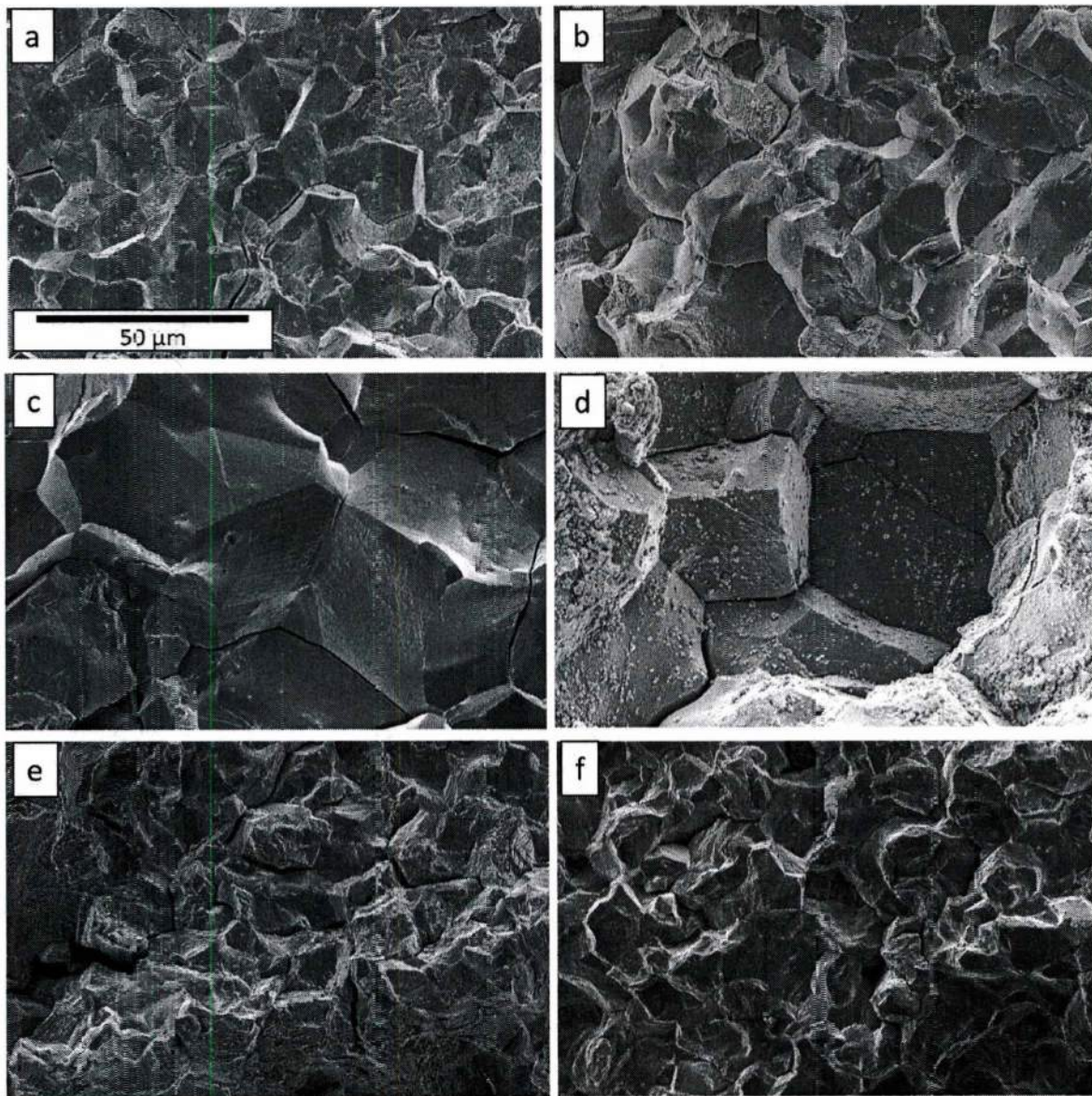


Figure 4 - Fractography of the intergranular (IG) fracture morphology observed for (a) Allvac, (b) TR1, (c) TR2, (d) TR3 and (e-f) NRL HS when tested in 0.6M NaCl solution with an applied potential of  $-950\text{mV}_{\text{SCE}}$ . In addition to the IG morphology, NRL HS (e-f) also exhibited some transgranular features.



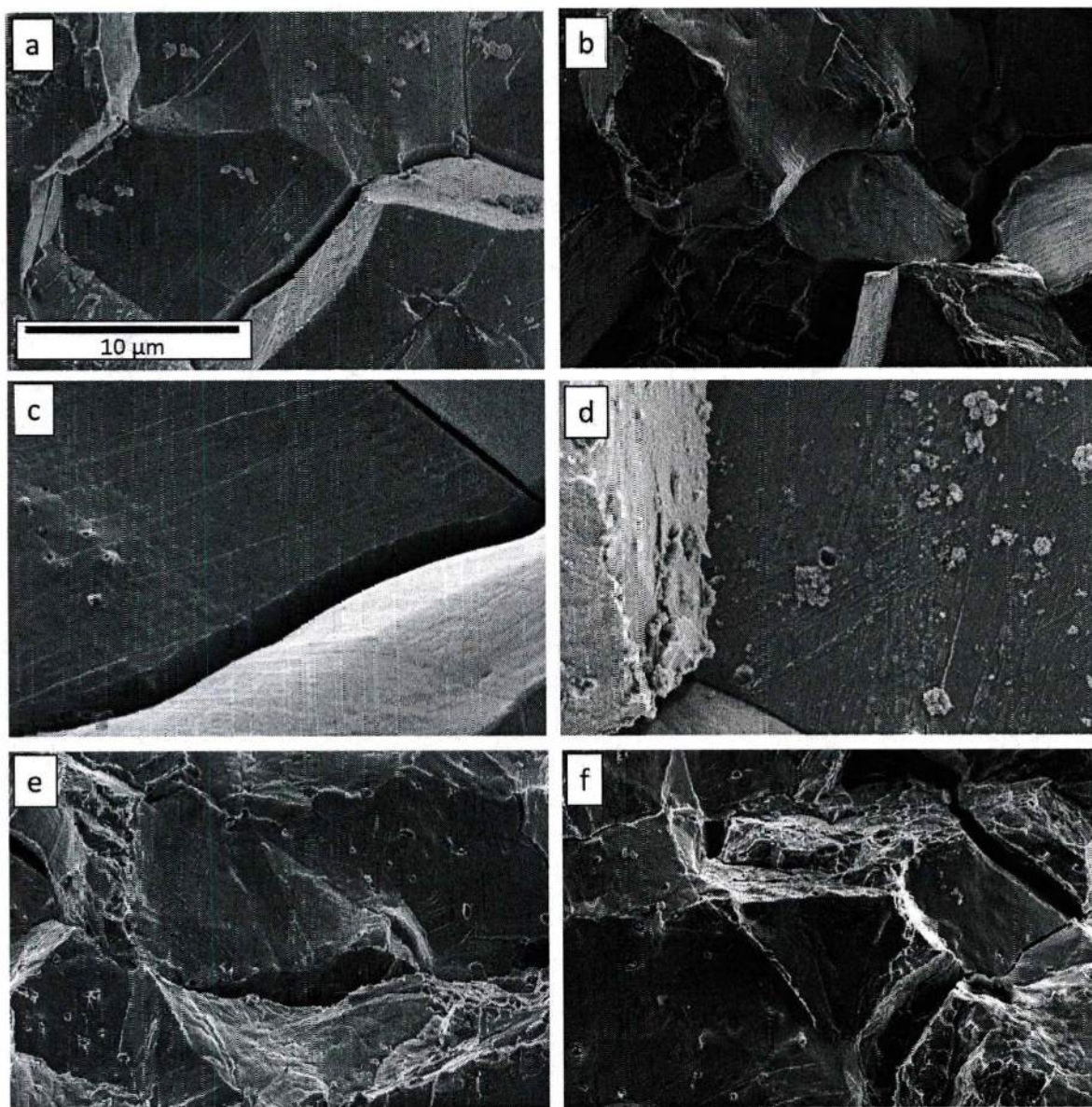


Figure 5 - Fractographs of facet slip traces for (a) Allvac, (b) TR1, (c) TR2, (d) TR3, and (e-f) NRL HS when tested in 0.6M NaCl solution with an applied potential of  $-550\text{mV}_{\text{SCE}}$ .



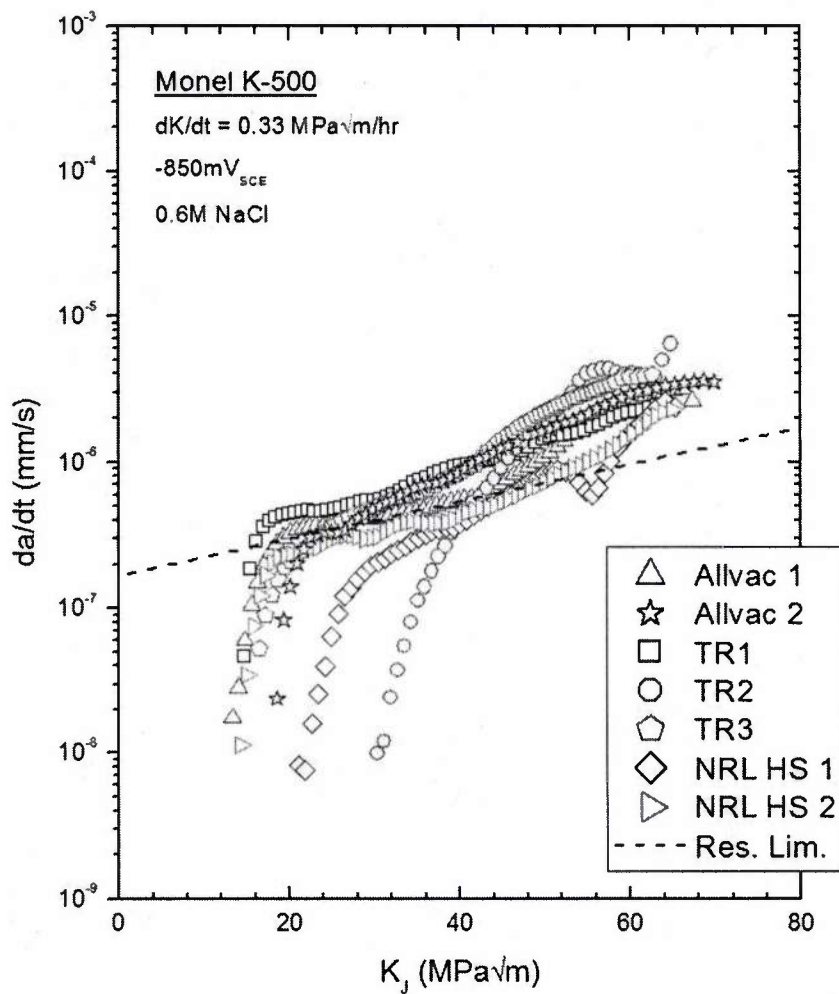


Figure 6 - Crack growth rate versus total  $K$  for five lots of peak-aged Monel K-500 stressed in NaCl solution at a constant applied potential of  $-850\text{mV}_{\text{SCE}}$ . The dashed line represents the expected false  $da/dt$  produced by crack tip plastic deformation for  $dK/dt = 0.33 \text{ MPa}\sqrt{\text{m/hr}}$ .

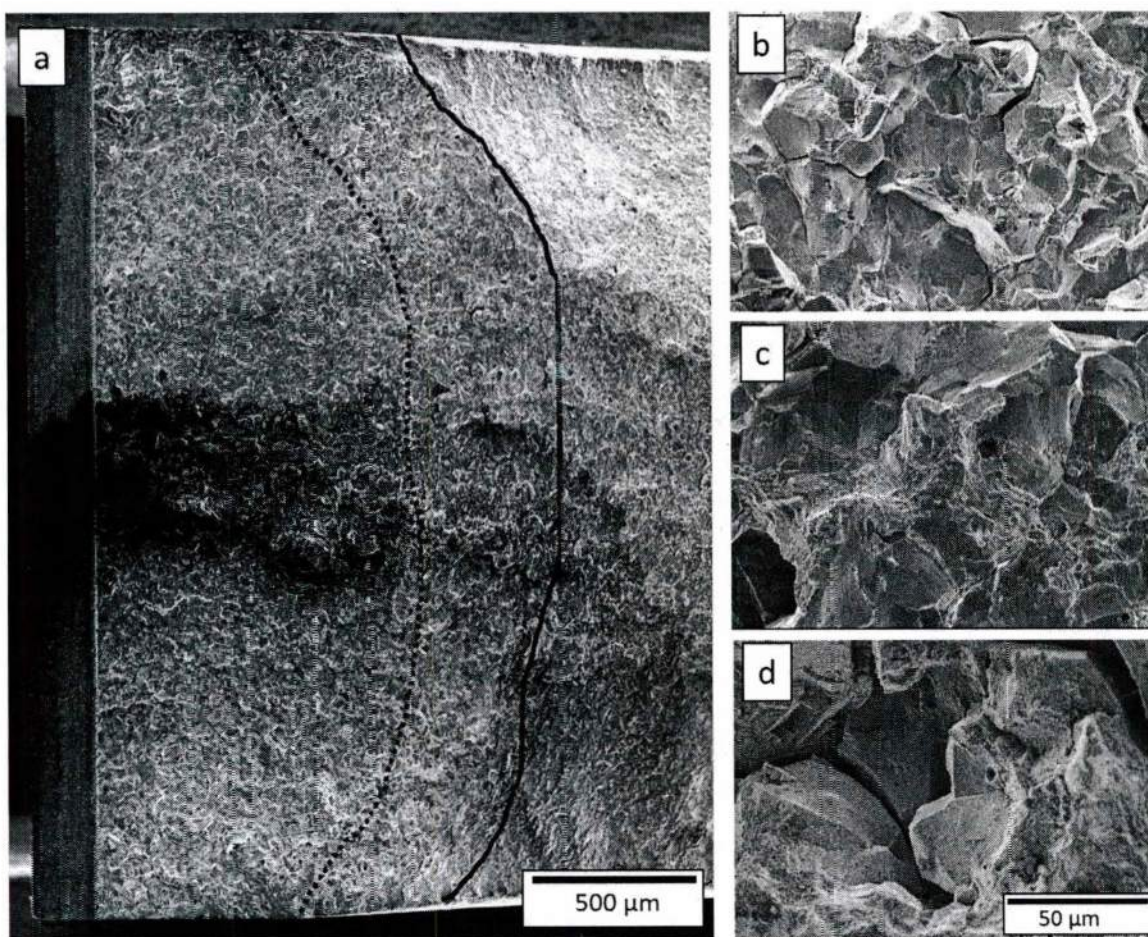


Figure 7 – Fractography of samples tested at an applied potential of  $-850 \text{ mV}_{\text{SCE}}$  in 0.6M NaCl: (a) overview of TR2 fracture surface and the fracture morphology observed at the crack length where  $K = 40 \text{ MPa}\sqrt{\text{m}}$  for (b) TR1, (c) TR2, and (d) TR3.

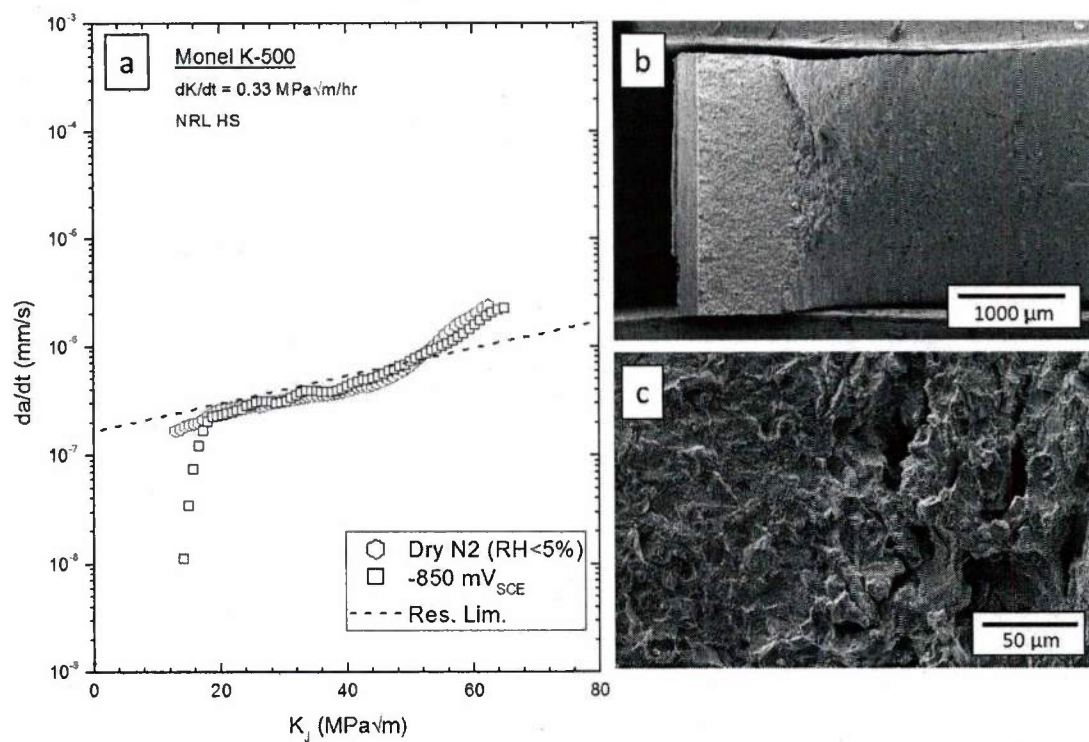


Figure 8 - Comparison of (a) crack growth kinetics data for NRL HS tested in dry N<sub>2</sub> and 0.6M NaCl at -850 mV<sub>SCE</sub> and fractographs of the (b) dimpled, ductile fracture morphology observed in the center (c) of the 0.6M NaCl at -850 mV<sub>SCE</sub> specimen.



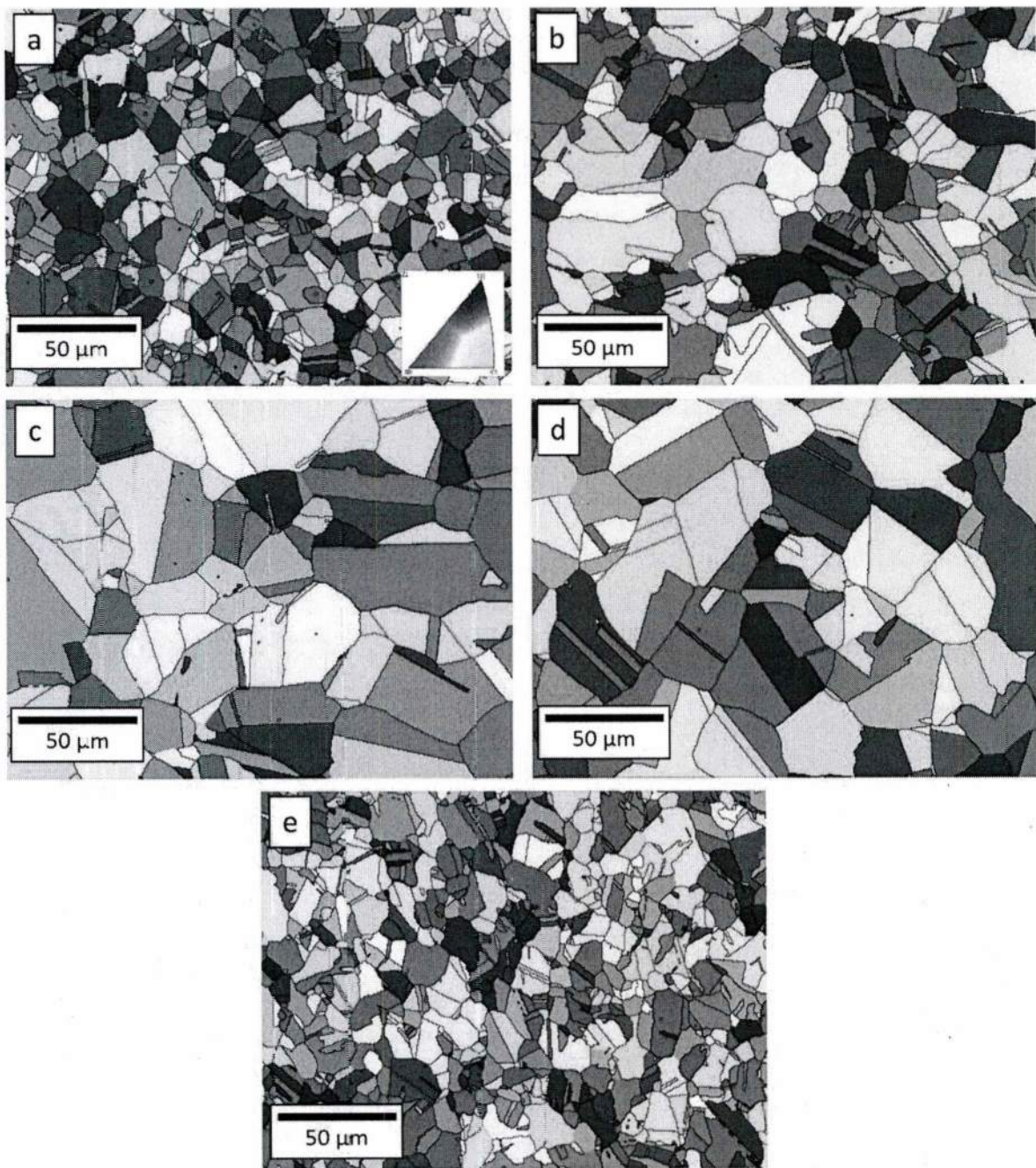


Figure 9 – Orientation maps for (a) Allvac, (b) TR1, (c) TR2, (d) TR3, and (e) NRL HS collected using electron backscatter diffraction. Grain boundaries (black lines) were defined by misorientations greater than 15°.



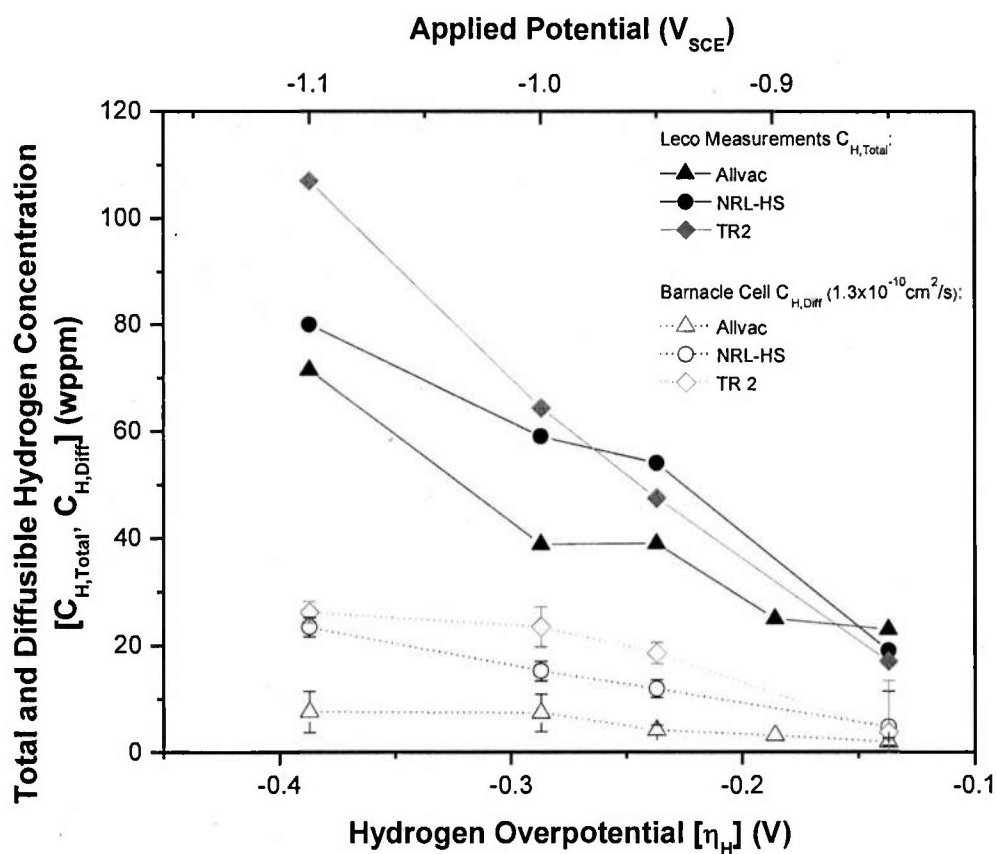


Figure 10 – Effect of hydrogen overpotential on total and diffusible hydrogen concentrations for the Allvac, TR2, and NRL-HS. Error bars represent 95% confidence interval.

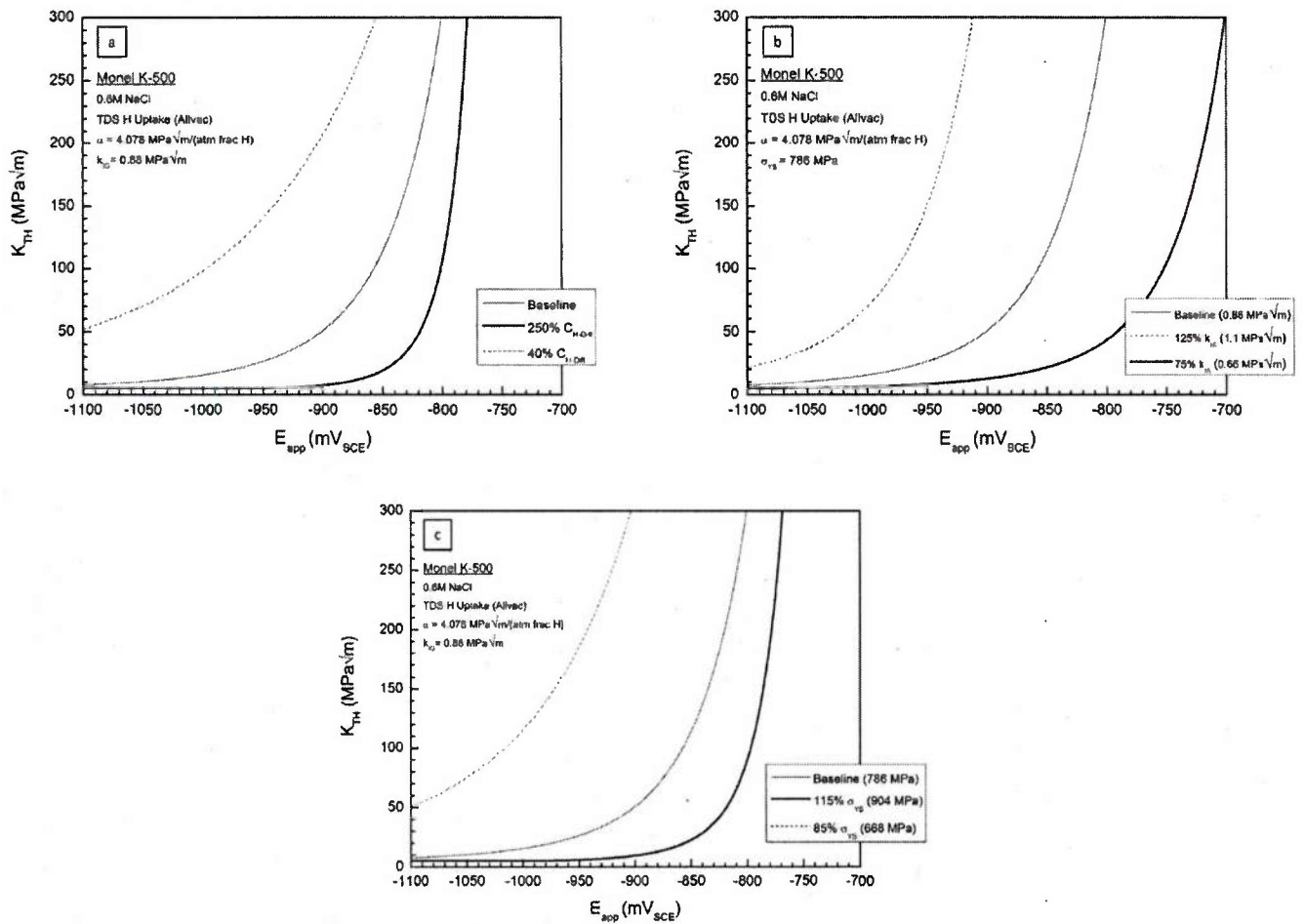


Figure 11 – Sensitivity analysis conducted on the modeling to determine the effect of (a) a  $\pm 250\%$  change in diffusible hydrogen concentration relative to the baseline value found for Allvac, (b) a  $\pm 25\%$  change in the Griffith toughness of the grain boundary ( $k_{IG}$ ) relative to the baseline value of 0.88 MPa $\sqrt{m}$ , and (c) a  $\pm 15\%$  change in the yield strength from the Allvac yield strength (786 MPa) on the calculated threshold stress intensity.

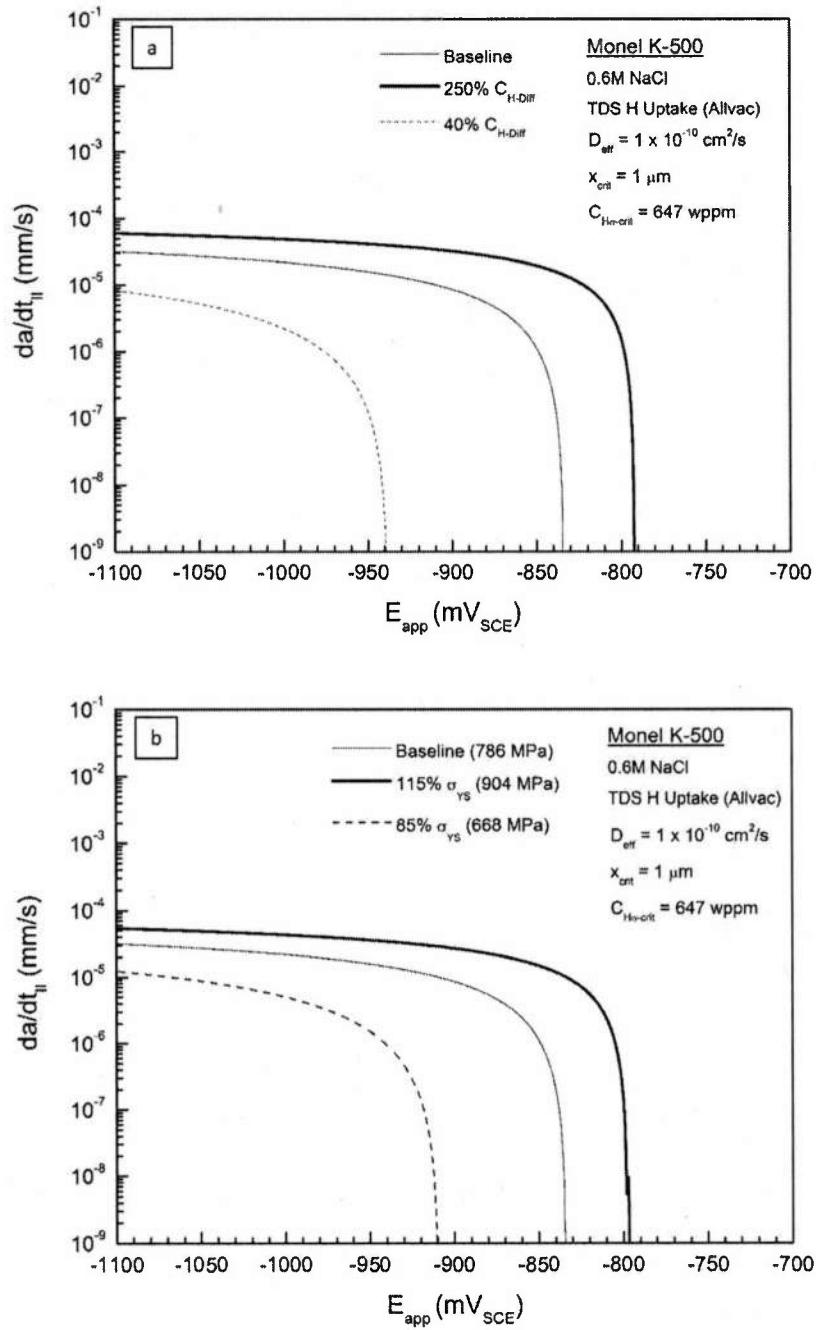


Figure 12 – Sensitivity analysis conducted on the modeling to determine the effect of (a) a  $\pm 250\%$  change in diffusible hydrogen concentration relative to the baseline value found for Allvac and (b) a  $\pm 15\%$  change in the yield strength from the Allvac yield strength (786 MPa) on the calculated H-diffusion limited crack growth rate,  $da/dt_{II}$ .

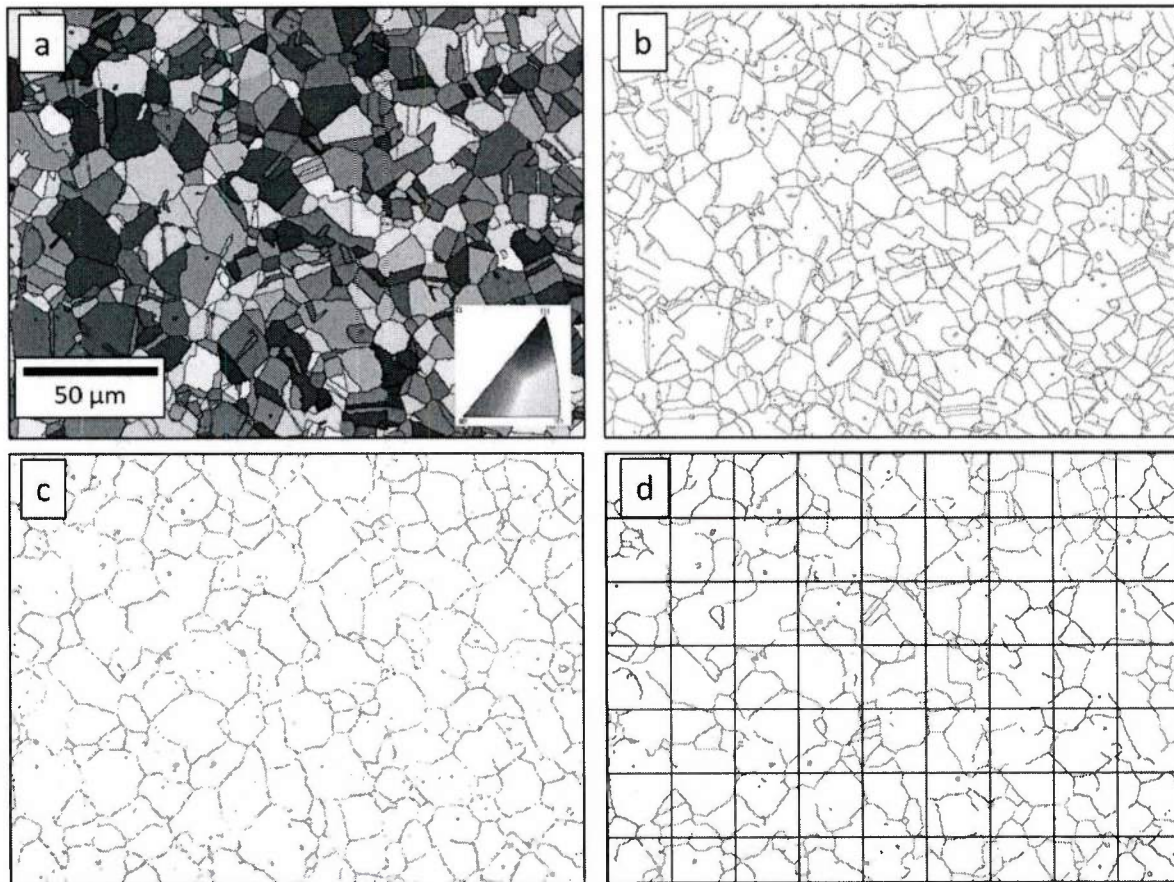


Figure 13 – The process for establishing the fractal dimension included: (a) obtaining an orientation map via electron backscatter diffraction, (b) identification of high (black lines) angle grain boundaries and low (red lines) angle grain boundaries, (c) isolating high angle grain boundaries by removing all low angle grain boundaries, (d) measuring the maximum connected network (highlighted red lines) and overlaying a square grid with a known side length.



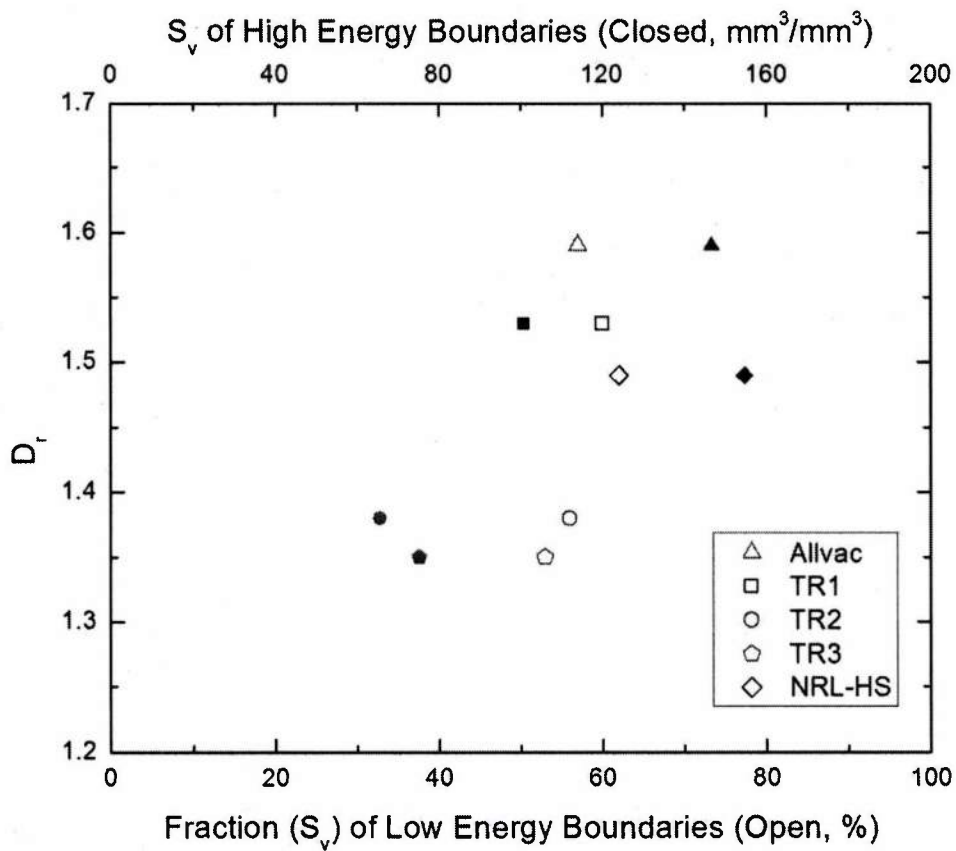


Figure 14 – Fraction of low energy boundaries (open symbols) and the  $S_v$  of high energy boundaries (closed symbols) versus the measured fractal dimension for each lot of Monel K-500.

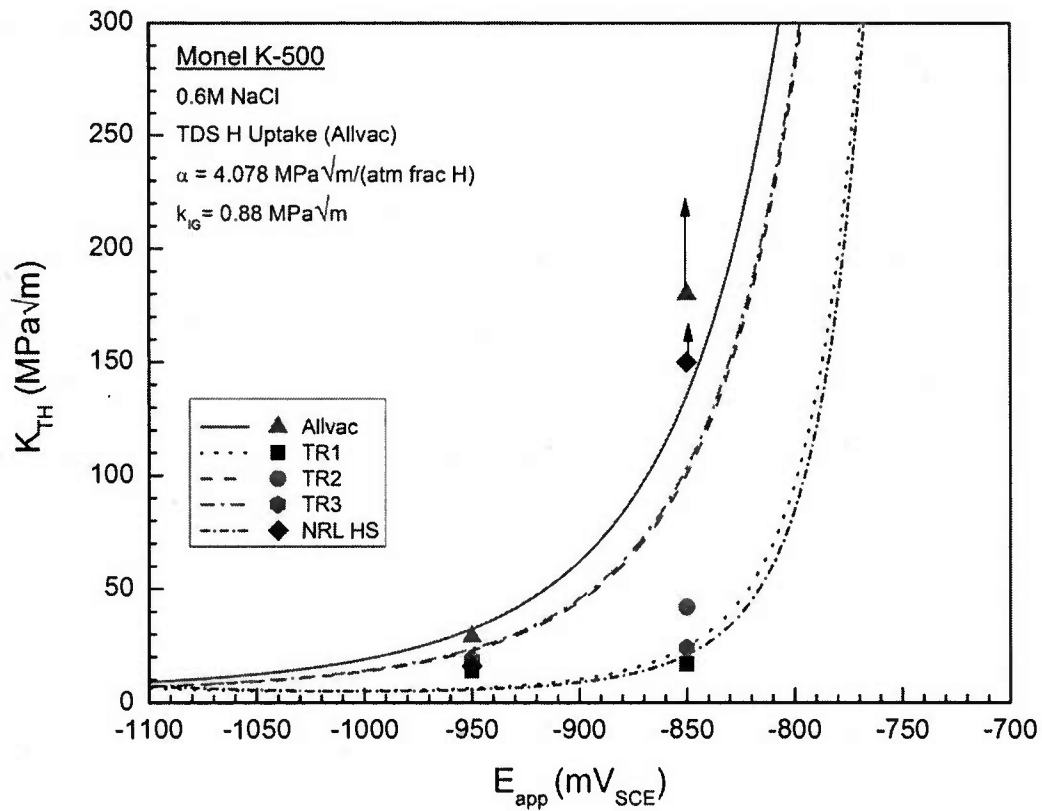


Figure 15 - Plot of the calculated threshold stress intensity versus applied potential curves for each lot of Monel K-500 using previously validated parameters with experimental data points included for -950 and -850 mV<sub>SCE</sub>. Black arrows extending upward represent experimental observations of HEAC immunity at the tested potential.

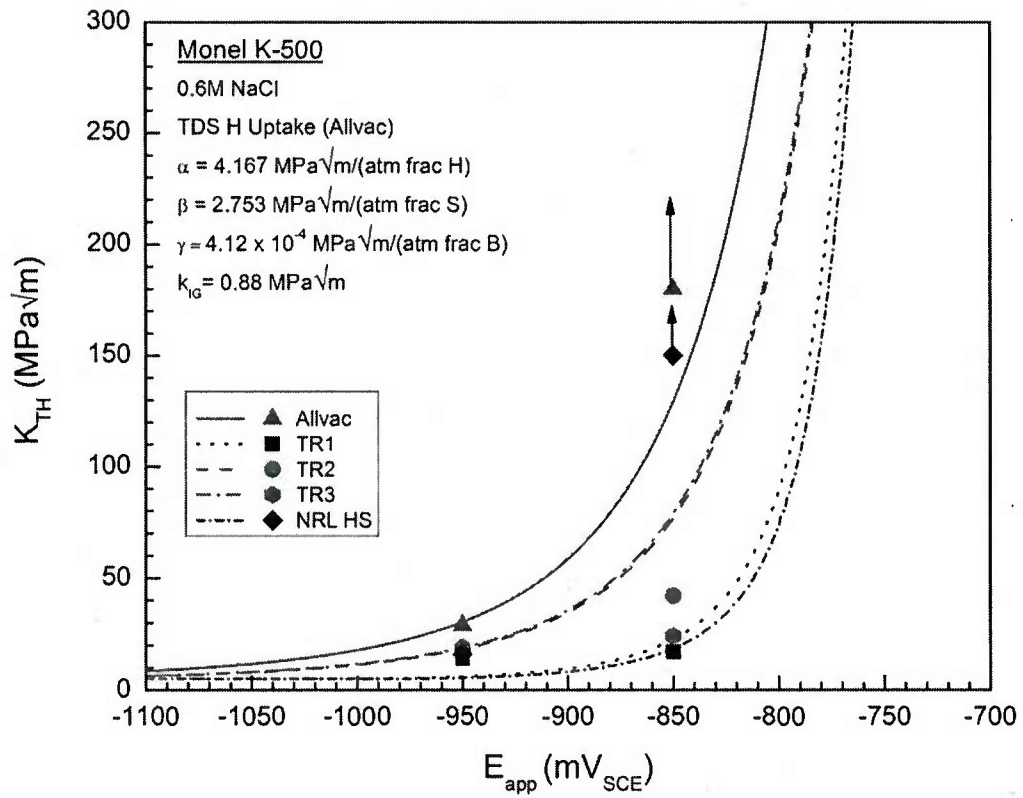


Figure 16 - Plot of the calculated threshold stress intensity versus applied potential curves for each lot of Monel K-500 using new parameters with experimental data points included for -950 and -850 mV<sub>SCE</sub>. New parameters include the effects of grain boundary impurity segregation of sulfur ( $\beta$ ) and boron ( $\gamma$ ). Black arrows extending upward represent experimental observations of HEAC immunity at the tested potential.

## **Chapter 2**

### **Effects of Heat to Heat Variations in Hydrogen Interactions on the Hydrogen Embrittlement Susceptibility of Monel K-500**

B.C. Rincon Troconis, H. Ha, Z. Harris, J. Burns and J.R. Scully

Center for Electrochemical Science and Engineering

Department of Materials Science and Engineering

University of Virginia

Charlottesville, VA 22904

#### **Abstract**

The influence of heat to heat variation on hydrogen environment-assisted cracking (HEAC) of aged hardened Monel K-500 (UNS N05500, 63 %Ni, 33 %Cu, 3.15 %Al, wt. %) was evaluated. Four peak-aged lots of material laboratory were tested under slow strain rate tensile testing (SSRT) while immersed in NaCl solution under various cathodic polarizations. All materials met a US federal specification based on mechanical properties and composition. One heat was harvested from seawater deployment where HEAC was observed after exposure at unknown levels of cathodic protection. Another heat cracked at less severe cathodic potentials in field ocean exposure when pre-cracked despite lower strength. Upon removal, hydrogen was detected by thermal desorption in both cases. In addition to SSRT, selected microstructural, compositional, as well as hydrogen-material interactions were investigated and compared. These included assessments of diffusible and total hydrogen concentrations, trap binding energies, diffusion rate, grain size, hardness, and compositional analysis including sulfur, key trace sulfur gettering elements and other beneficial elements which alter sulfur solubility. Moreover, grain boundary chemistry was assessed after aging and hydrogen fracture by Auger Electron Spectroscopy. Sulfur enrichment was observed. All materials were susceptible to hydrogen embrittlement with differences between field susceptible heats and the others. The heats identified in seawater and field testing exhibited more facile intergranular cracking, absorbed more hydrogen relative to other heats as a function of cathodic polarization, and contained unfavorable concentrations of trace detrimental grain boundary segregating elements relative to the beneficial gettering elements in combination with a low density of grain boundary trap or segregation sites per unit volume. Greater susceptibility is traced to enhance hydrogen uptake and speculated grain boundary sulfur enrichment based on alloy trace chemistry coupled with grain boundary trapping of hydrogen supplied from charging during cathodic polarization. Material hardness within the limits from Rockwell C 28 to 36 was not found to be the dominant factor.



## Introduction

Monel K-500 is a precipitation hardenable nickel based alloy with composition 63%Ni, 33 %Cu, 3.15 %Al, 1.5 %Mn, 2 %Fe, 0.85 %Ti (in wt%) [1]. This alloy is utilized for different applications such as marine service, chemical processing, pulp industry, oil and gas production and electronic components. The matrix is characterized by a Ni-Cu face centered cubic structure [2]. The peak aged materials present an uniform distribution of spherical  $\text{Ni}_3(\text{Al}, \text{X})$  precipitates known as  $\gamma'$ , where X can be Cu, Mn, Ti or Si. This alloy commonly also contains incoherent carbides in the form of TiC [2] that suffer little coarsening and shape change during aging. But, when alloyed for long period of times other carbides are also present in the chemical form of  $\text{M}_{23}\text{C}_6$  (M: Ni, Mn or Fe). Another microstructure feature that can be present in this alloy are the annealing twins [2]. These are present in solution heat treated (SHT) aged, SHT water quenched (WQ) and SHT air cooled (AC) materials. All these microstructural features can interact with H. Despite of the alloy immunity in some environments, structural failures related to hydrogen embrittlement (HE) have been reported [3-6].

The reported failures took place under sacrificial cathodic polarization in seawater. Reduction in tensile ductility and notch strength was observed for SHT aged Monel K-500 alloy coupled to zinc producing potentials from -1 to -1.1  $\text{V}_{\text{SCE}}$ <sup>13</sup> [3, 5]. Intergranular failures of bolts subjected to cathodic polarization have also been reported in age hardened Monel K-500 alloys [4, 6]. These failures were attributed to the hardening of the material through age hardening after threading, achieving a hardness Rockwell C (HRC) of approximately 39. Therefore, a modification of the heat treatment [4], involving annealing after threading followed by age hardening, was proposed to maintain the hardness bellow HRC 35. In despite of this processing modification, bolt failures continued to be reported at lower hardness levels [6]. Threaded bolts annealed at a temperature of 980-1050 °C during, water quenched (WQ) and precipitation hardened at 500-600 °C during 16 hours with a final hardness of 25 (Below limit recommended in US federal specification [3]) failed [6]. Sporadic failures occurred after 1 year exposure under sacrificial cathodic protection using Al anodes under a load representing 60% of the yield strength of the material [6]. Slow strain rate testing (SSRT) experiments performed in ASTM artificial seawater on pre-charged specimens potentiostatically or using Al and Fe anodes, (representing high and low hydrogen overpotential) resulted in intergranular cracking.

HE failures have been indicated to result from grain boundary segregation particularly in combination with hydrogen [7, 8]. Elements present in the bulk alloys in the order of ppm (trace

---

<sup>13</sup> All potentials are hereafter referenced to Saturated Calomel Electrode (+0.241 V vs. a standard hydrogen electrode)

elements) can segregate to the grain boundary, producing highly localized enriched volume of material with concentrations with orders of magnitude higher than that of the bulk concentration. That is the case of elements such as S, Pb, P, Zr, Hf, Ca and Mg [9-12]. The segregation strength will depend on different parameters such as the specific element, bulk solubility, segregation energy, grain boundary nature and the presence of other elements that can interact with the segregating element, decreasing segregation [13, 14]. Hydrogen is thought to segregate preferentially to the grain boundaries facilitating grain boundary de-cohesion, leading to HE [15]. Nickel hydriding has been detected [16-18]. But, is not believed to be the main factor controlling failure in sea water under typical cathodic protection conditions although, it is observed at extreme hydrogen uptake conditions. The process of hydrogen embrittlement proposed is in good agreement with experiments and involves crack tip hydrogen production, uptake, and diffusion into the fracture process zone and at grain boundaries where fracture occurs [15, 19-21]. This process can be enhanced by S presence in the material, which is an element known to be deleterious for Ni-based alloys [8, 22, 23]. Traces of this element can result in grain boundary concentrations that are 2000 times the bulk concentration [7, 23, 24]. It has been postulated that the electronegativity of this element interacts with the bonding strength in the grain boundary, resulting in grain boundary de-cohesion [22]. This hypothesis has been rationalized in terms of the local spin density atomic cluster [25] and quantum-mechanics cluster calculations. Another element known to segregate to grain boundary is P [23]. The literature offers information regarding the inert and even beneficial effect of this element [10, 26, 27]. Sb is another element that has been found to be deleterious for alloy performance. Sb segregates to the grain boundary and lowers the threshold stress intensity [28]. H and S have been found to act synergistically towards HE [1, 29-32]. A relationship taking into consideration the average grain boundary fracture surface coverage of segregating elements ( $C_x$ ) and their fractional relative potency with respect to S to promote hydrogen cracking has been defined empirically from straining electrode data [32]:

$$C_s^{eq} = C_s + 0.07C_p + 0.6C_{sb} \quad \text{Eq. 1}$$

Also, another equation has been formulated, in this case to explain the effect of impurity segregations on the fracture stress of a notched specimen [33],

$$\sigma_{frac} = \sigma_{frac}^{vacuum} - \alpha C_H^x - \beta C_x^y \quad \text{Eq.2}$$

where, x and y are typical fractions,  $\sigma_{frac}^{vacuum}$  is the fracture stress in vacuum and  $\alpha$  and  $\beta$  describe a weighting factor of the deleterious effect of impurities on fracture stress.

S is known to interact with hydrogen and enhance HE. However, there are certain elements, called getter elements, that can be intentionally added to the alloy to react with S and avoid its segregation to the grain boundary. These elements can form sulfo-carbides (Zr, Hf) [12, 34] and sulfides (Mg, Ca, Zr) [23]. Yamaguchi developed a model to evaluate the S gettering power of these elements based an empirical analysis considering experiments related to hot workability and chemical characterization of grain boundary through Auger electron spectroscopy [35]. A modified expression is available considering the addition of Hf effect with a similar weight as Zr (similar solubility product) and neglecting the gettering power of Ca as it is considered to be present mainly as stable CaO [36].

$$C_{\text{Get}} = 0.3\text{Mg} + 0.1\text{Zr} + 0.1\text{Hf} \quad \text{Eq. 3}$$

Hardness has been explored as a parameter that could affect the HE of Ni-based alloys [37, 38]. The hardness of an Inconel material was reduced using laser driven surface modification. The laser treatment modified the surface layer of the material, up to 1 mm in thickness, dissolving  $\gamma'$  precipitates and enhancing the material ductility of the alloy under  $\text{H}_2$  environment when compared to a non-treated material exposed to the same conditions [37]. Hardness is a key parameter in decohesion models applied to Monel K-500. It can be shown that hardness alone can produce a drop in  $K_{\text{th}}$  and rise in stage II crack growth with hydrogen; but significantly, has a strong effect on the cathodic potential threshold [15, 36].

A relationship between the critical stress for cracking,  $\sigma^*$ , and material dependent variables such as the uniaxial tensile yield strength,  $\sigma_y$ , in the presence of gaseous hydrogen for steel has been established [38],

$$\sigma^* = \sigma_o^* - A(P_{\text{H}_2})^{1/2} \exp \left[ \frac{\bar{V}_H(2.6\sigma_{11} - 1.3\sigma_y)}{3RT} \right] \quad \text{Eq. 4}$$

where  $\sigma_o^*$ ,  $A$ ,  $\bar{V}_H$  are materials variables and represent the material-dependent constants ( $\sigma_o^*$  and  $A$ ) and the partial molar volume of hydrogen inside the metal,  $P_{\text{H}_2}$  is the hydrogen pressure,  $\sigma_{11}$  is the principle local stress perpendicular to the crack,  $R$  is the gas constant and  $T$  is temperature. Modelling of the threshold stress intensity utilizing Eq. 4 shows that for the same  $P_{\text{H}_2}$  an increase on  $\sigma_y$  represents a decrease in the threshold stress. However, it is important to point out that  $\sigma_y$  cannot be varied independently and that the values  $\sigma_o^*$  and  $A$  cannot be measured, which makes impossible the comparison of Eq. 4 with real data. Another study [39] based on the effect of aging temperature and therefore hardness on hydrogen permeation parameters elucidates the increase in absorbed hydrogen with hardness for 18Ni(250) steel, which can result in a decrease in critical stress intensity [40] and the threshold stress intensity for cracking [41]. In addition, the diffusivity was found [39] to decrease with hardness and then

achieve steady state for over aged materials, which can result in slow crack growth rates for diffusion controlled cracking [40]. In a secondary hardened martensitic steel greater hardness brought about by  $M_2C$  carbides provided traps sites for hydrogen which could repartition to crack tips [42].

Hydrogen uptake, diffusivity and trap binding energy were determined [43] for single phase solid solution, aged, and cold worked then aged Monel K-500 alloy. The total hydrogen concentration,  $C_{H,tot}$  in alkaline 3.5 % NaCl was found to be in the range 0-132 ppm, while the diffusible hydrogen concentration,  $C_{H,diff}$ , was lower and in the range 0-36 ppm, approximately [43]. Both hydrogen concentrations were found to be dependent on hydrogen overpotential. The diffusible hydrogen concentration was found to be dominated by the hydrogen in the lattice and to a lesser extent some hydrogen in reversible traps, excluding the  $\gamma'$  precipitates, while the total hydrogen concentration included the diffusible hydrogen, the hydrogen present in the reversible  $\gamma'$  precipitate traps and the hydrogen in irreversible trap sites [43]. The reversible traps could involve microstructural features such as copper solute in the solid solution matrix, dislocations, twin boundaries, low energy grain boundaries and some sites on  $\gamma'$  precipitates [44, 45]. Grain boundaries and dislocations have been reported as hydrogen trap sites [46]; however they have a low site density in the order of  $10^{17}$  sites/cm<sup>3</sup>, except in ultra-fine grain size microstructures [47, 48]. The room temperature hydrogen diffusion coefficient was found to range from 0.9 to  $3.9 \times 10^{-14}$  m<sup>2</sup>/s [43]. The apparent activation energy for diffusion was found to be approximately  $29-41 \pm 1.5$  kJ/mol. The trap binding energy for  $\gamma'$  precipitates ( $10.2 \pm 4.6$  kJ/mol) was found to agree with previous studies [44, 46] and lower than the activation energy of perfect lattice diffusion ( $25.6 \pm 0.5$  kJ/mol) [43]. Despite all of the work performed previously [43, 44], pertaining to hydrogen interaction in Monel K-500 alloys, there is a heat to heat variation that needs to be addressed since it affects the HE susceptibility of this alloy.

This manuscript aims to address some of the possible effects of heat to heat variations on the susceptibility of Monel K-500 to HEAC with emphasis on hydrogen material interactions. A previous study addressed possible origins of differences from a fracture mechanics perspective [36]. In this study, slow strain rate tests (SSRT) of notched samples pre-charged with hydrogen during 48 h in 0.6 M NaCl solution at different hydrogen overpotentials elucidated differences in terms of fractography morphology, local breaking stress and time to failure (TTF) among the heats. In air and at a hydrogen overpotential of -0.137 V the fractography was characterized by micro-void ductile fracture, while during polarization to more negative potentials the failure mode changed to a mixture of ductile/intergranular (IG) fracture at -0.237 V and finally to IG fracture at hydrogen overpotentials of -0.287 and -0.387 V. To explain this behavior, the heats were characterized in terms of mechanical properties, microstructure, bulk and grain boundary composition, and H-interactions. Parameters such as hardness, grain size, grain boundary



character, impurity segregation, hydrogen production rate, total and diffusible hydrogen concentration, hydrogen diffusion and trap binding energies were determined for the different heats and will be discussed in terms of their possible effects on hydrogen embrittlement (HE) susceptibility. The discussion presented herein will provide insightful information pertaining to the effect of heat to heat variations on the susceptibility of the Monel K-500 alloy to HE.

## **Methods**

### *Materials and Hardness*

Four different Monel K-500 alloy (UNS N05500) heats with compositions shown on Table 1 were tested. One of them was supplied by Allegheny Technologies Incorporated. This Monel K-500 material was hot-finished and aged, specifically, it was aged at 593 °C (1100 F) for 16 hours, then furnace cooled at 25 F/hour to 482 °C (900 F) followed by air cooling. This condition is labeled as Allvac. Another heat was harvested from the field after exposure to a marine environment. There is no information about exact heat treatment nor exposure time but the material was aged. This heat is labeled as TR 2. Two other heats were supplied by the U.S. National Research Laboratory. These heats were heat treated [49] to obtain upper and lower bounds of QQ-N-286G federal specification [3]. These heats were labeled as low strength, NRL LS (Special Metals heat M5437KG12), and high strength, NRL HS (Special Metals heat M60N4KG14), specimens. The heat treated specimens were of 4 inch and 4.5 inch diameter bars for NRL LS and NRL HS, respectively. NRL LS was hot rolled, continuously annealed at 982 °C (1800 F) followed by water quench, rotatory straightened, rough turned (0.250 inch from diameter) then 3-point straightened and aged. The aging procedure corresponds to 593 °C (1100 F) during 2 h, furnace cooled to 482 °C (900 F) at 100 F/h and then air cooled. The NRL HS was direct-aged. The aging procedure was carried at 593 °C (1100 F) during 16 h, furnace cooled at 25 F/h up to 538 °C (1000F) during 6 hours then furnace cooled at 25 F/h to 900F for 9 h and air cooled. All NRL specimens were initially exposed as 0.750 inch (1.905 cm) thick compact tension discs to seawater under cathodic polarization from -0.750 to -1.1 V vs Ag/AgCl before retrieval. Specimens were baked for 48 hours at 450 °C prior to laboratory tests presented herein. The hardness of each heat was measured at least 5 times on Rockwell C or B Scale, the average value is reported on Table 2.

### *Microstructure*

The microstructure, grain boundary nature and texture were evaluated using a FEI Quanta 650 scanning electron microscope, SEM, based electron backscattered diffraction, EBSD with a beam accelerating voltage of 30 kV and a probe current of 5 nA. These settings allow an angular resolution less than  $1^\circ$  and a spatial resolution less than 30 nm in any direction and less than 10 nm axially. The maximum theoretical error in any measured feature size is less than 10%. This error was calculated using the SEM parameters. Representative areas of each heat were chosen to acquire the Orientation imaging maps (OIM). For this purpose, specimens were cut and grinded with SiC paper up to 1200 grit, then polished using 3 and 1  $\mu\text{m}$  glycerol polycrystalline diamond suspensions, followed by vibratory polishing in propylene glycol alumina suspension of 0.05  $\mu\text{m}$  to reduce surface deformation. The surfaces were cleaned using cotton balls soaked with ivory soap to remove alumina residue and then rinsed with d.i. water followed by ethanol. The samples were dried with compressed air. EBSD results are reported elsewhere [36]. The average grain size is reported in Table 2.

#### *Slow Strain Rate Tensile, SSRT, Test*

SSRT tests were performed on all the Monel K-500 heats using a Cortest, Inc frame at a cross-head speed on the order of  $10^{-6}$  mm/s until failure. The SSRT specimens were machined into a notched cylinder geometry with dimensions shown on Figure 17. The tests were performed in deaerated 0.6 M NaCl at 25  $^\circ\text{C}$ . Prior SSRT testing the specimen was baked at 450  $^\circ\text{C}$  during 48 h to desorb the hydrogen present inside the material. Then, it was charged using a three electrode electrochemical cell setting with a Pt mesh as counter electrode and a Saturated Calomel Electrode, SCE, as reference electrode. This cell was designed to allow charging in situ prior and during SSRT testing. The grips were masked utilizing Micro Super XP-2000 Stop-off Lacquer to avoid galvanic coupling with the specimen. The potential was controlled using a research grade Gamry Reference 600 potentiostat during 48 hours at -1.1  $V_{\text{SCE}}$  prior and during SSRT testing. After specimen fracture, both fracture surfaces were thoroughly rinsed with tap water, ultrasonically cleaned in D.I. water for 20 minutes, followed by ultrasonic cleaning in ethanol for 20 mins and dried with compressed air. One fracture surface was analyzed using the SEM, while the pair was send for surface analysis of the grain boundary chemistry using Auger Electron Spectroscopy, AES.

#### *AES*

AES depth profile analyses were carried on using a Physical Electronics USA, Inc. (PHI) model 680 scanning auger microprobe, with a Schottky field emission electron source and a Cylindrical Mirror Analyzer (CMA). Auger spectra were collected using a 10 kV and 20 nA primary electron beam. The depth profile on the grain boundary was achieved thru calibrated sputtering the specimen surface in a

localized grain boundary with a rastered (3mm x 3mm) argon beam at 3kV. The atomic fraction of each element  $x$ ,  $AF_x$ , was calculated according to,

$$AF_x = \frac{I_x/S_x}{\sum(I_n/S_n)} \quad \text{Eq. 5}$$

where  $I_x$  is the intensity measured for element  $x$  in the counts per second versus kinetic energy spectrum and  $S_x$  is the sensitivity factor of element  $x$ .

#### *Electrochemical Techniques*

A three electrode cell setting with a Pt mesh as counter electrode and a SCE as reference electrode was used for all electrochemical tests. The potential was controlled using a potentiostat. The electrolyte used for all the experiments was 0.6 M NaCl pH 8.0 by adjustment with NaOH. Cathodic potentiodynamic polarizations were performed on all the Monel K-500 heats at a scan rate of 0.167 mV/s.

#### *Electrochemical Hydrogen Charging*

To evaluate the hydrogen uptake of the different Monel K-500 heats,  $120 \pm 10 \mu\text{m}$  planar thick specimens were ground to 600 grit surface finish, rinsed with D.I. water, degreased with ethanol ultrasonically, dried with compressed air and charged with hydrogen via cathodic potentiostatic polarization at different potentials (-0.850, -0.950, -1.0 and -1.1  $V_{\text{SCE}}$ ) in 0.6 M NaCl (pH 8.0 by adjustment with NaOH) during 7 days. In the case of determination of binding energies a potential of -1.0  $V_{\text{SCE}}$  was used during charging. The charging time and specimen thickness to achieve approximately 90% hydrogen saturation of the specimen were chosen based on diffusion calculations assuming that surface concentration and hydrogen diffusion coefficient ( $0.9 - 3.9 \times 10^{-14} \text{ m}^2/\text{s}$  [43]) were constants, semi-infinite solid and slab geometry [50]. Prior hydrogen charging, specimens were grinded to 600 grit, followed by ultrasonic cleaning in ethanol for one minute and finally dried with compressed air.

#### *Determination of Diffusible and Total Hydrogen Concentration through Electrochemical Extraction and LECO, respectively*

The diffusive hydrogen concentration,  $C_{\text{H,Diff}}$ , was determined using an electrochemical extraction method [43, 51]. This technique is based on the electrochemical method of hydrogen permeation developed by Devanathan et al. [52] After charging, the specimen was slightly abraded with 600 grit SiC paper and then rinsed with D.I. Water and ethanol followed by drying with compressed air. The hydrogen diffusing out from the specimen was oxidized at -0.85  $V_{\text{MMSE}}$  in de-aerated Borate Buffer (pH: 10) during

one hour, even though only the first half hour of the data was used for calculations ( $-0.85 V_{MMSE}$  is more positive than  $-1.21 V_{MMSE}$ , which is the Nernst potential for hydrogen at pH: 10). The Barnacle Cell test was performed at least three times on each Monel K-500 heat.  $C_{H,Diff}$  was calculated following [51],

$$C_{H,Diff} = \frac{J_t}{zF} \left( \frac{D_{eff}}{\pi t} \right)^{-1/2} \quad \text{Eq.6}$$

where  $J_t$  is the hydrogen oxidation current density at time  $t$  ( $A/cm^2$ );  $z$  is the number of electrons involved in the reaction ( $z$ : 1 equivalent per mole for hydrogen evolution reaction);  $F$  is the Faraday constant (96,498 C/ equivalent) and  $D_{eff}$  is the effective hydrogen diffusivity (a value of  $1.3 \times 10^{-14} m^2/s$  was utilized according to those found in the literature for Monel K-500 alloys [43]). Equation 6 is only valid when  $L^2/Dt \geq 4$  [51], where  $L$  is the depth from which the hydrogen is extracted. In addition,  $D_{eff}$  was assumed to be independent of  $C_{H,Diff}$ , fact that was verified previously [43]. The  $C_{H,Total}$  was determined from LECO hydrogen measurements heating to a maximum temperature of 650 °C according to ASTM Standard E1447-09/CTP 3008-1/IG [53].

#### *Determination of Total Hydrogen Concentration and Binding Energy through Thermal Desorption Spectroscopy*

A Thermal Desorption Spectroscopy system described previously [54, 55] was utilized to determine the trap binding energy,  $E_B$ , and the effective hydrogen diffusivity,  $D_{eff}$ . Desorbed hydrogen was measured, under high vacuum, as hydrogen partial pressure,  $P_{H_2}$ , during programmed ramped heat experiments to calculate the parameters previously mentioned. Backgrounds were measured using the residual gas in the system without any specimen at different heating rates.

The  $D_{eff}$  was calculated taking into consideration the dependence of the increase in integrated-absorbed hydrogen level in a plate of known thickness,  $2l$ , on the  $D_{eff}$ . The solution of the diffusion equation by a membrane under non-steady state conditions with equal surface concentrations and uniform initial concentration gives [56]:

$$\frac{M_t}{M_\infty} = 1 - \sum_{n=0}^{\infty} \frac{8}{(2n+1)^2 \pi^2} \exp\{-D(2n+1)^2 \pi^2 t / (4l^2)\} \quad \text{Eq.7}$$

where,  $M_t$  denotes the total mass of H absorbed by the membrane at time,  $t$ , and  $M_\infty$  indicates the total mass of H absorbed after infinite time. Experimental data was gathered for specimens charged at different times and tested for absorbed hydrogen content by thermal desorption using a heating rate of 10 °C/min up to a temperature of 550 °C. The data was background corrected, the hydrogen desorbed was integrated



with respect to heating time and compared to theoretical curves of  $M_t/M_\infty$  vs  $t^{1/2}$  using different  $D_{\text{eff}}$  values to choose the curve that best fitted the experimental data.

For the case of a cylinder geometry for NRL heats, the solution of the diffusion equation for non-steady state is given by [56],

$$\frac{M_t}{M_\infty} = 1 - \sum_{n=1}^{\infty} \frac{4}{a^2 \alpha_n^2} \exp(-D \alpha_n^2 t) \quad \text{Eq. 8}$$

where,  $a$  is the cylinder radius and  $\alpha$  is the positive root of  $J_0(a\alpha_n) = 0$  being  $J_0$  the Bessel function of the first kind of order zero. In this case, the NRL samples were pre-charged at different time intervals at -0.800, -0.850, -0.890 and -1.000  $V_{\text{SCE}}$  in seawater. Theoretical calculations were performed for hydrogen diffusivities of  $5 \times 10^{-10} \text{ cm}^2/\text{s}$ ,  $1 \times 10^{-10} \text{ cm}^2/\text{s}$  and  $2 \times 10^{-10} \text{ cm}^2/\text{s}$ .

Experiments at different heating rates of 3, 5, 7.5 and 10  $^\circ\text{C}/\text{min}$  were performed to determine the  $E_B$ . For this purpose,  $120 \mu\text{m} \pm 10 \mu\text{m}$  thick flat plate specimens were electrochemically charged with hydrogen in 0.6 M NaCl (pH: 8.0 by adjustment with NaOH) during 7 days at -1.0  $V_{\text{SCE}}$ . This parameter can be estimated from the H desorption energies,  $E_d$ . It is known that the  $E_d$  is equal to the sum of the activation energy for H migration from an interstitial lattice site to a trap,  $E_m$ , and the  $E_B$ . Now, assuming that  $E_m$  is equal to the activation energy for H diffusion by an interstitial jump mechanism in the trap-free or perfect lattice,  $E_m$ , then  $E_d = E_m + E_B$ . This relationship between the energies is only valid if detrapping and lattice diffusion are the dominant processes during H desorption. The  $E_d$  for a specimen with a homogenous H concentration across its thickness is defined by [57]:

$$\frac{dx}{dt} = A(1-x)^n \exp\left(\frac{-E_d}{RT}\right) \quad \text{Eq. 9}$$

where  $x$  is the fraction of the desorbed H quantity integrated from a single desorption site and therefore a single deconvoluted TDS peak,  $A$  is a constant,  $n$  is the reaction order,  $R$  is the gas constant (8.31 J/mol K) and  $T$  is the temperature in K. Equation 9 provides a reasonable approximation of  $E_d$  when the following conditions are met: fast diffusion or slow diffusion taken into account, existence of a single dominant trap, minimal retrapping and low trap occupancy [58]. When measuring the desorbed hydrogen utilizing TDS, different desorption peak temperatures  $T_m$  are measured. These values depend on the heating rate [59, 60]. These  $T_m$  and the utilized heating rate values were used to calculate  $E_d$  using the following equation [57], which is valid for detrapping and diffusion-controlled egress under certain conditions [61].

$$\frac{d\left[\ln\frac{dT/dt}{T_m^2}\right]}{d[1/T_m]} = -\frac{E_d}{R} \quad \text{Eq. 10}$$

The data was plotted as  $\ln\frac{dT/dt}{T_m^2}$  vs  $1/T_m$  and then the  $E_d$  was calculated from the slope of the linear regression fitted to the experimental data points with a confidence interval of 95%. The characteristic desorption spectra was always composed of two peaks, which were deconvoluted based on Gaussian distribution model using the *OriginPro 7.5* software to determine  $T_m$ . The lowest  $T_m$  value was associated with the hydrogen trapped in the lattice in accordance with trap theory [62].

#### *Determination of Grain Boundary Trap Binding Energy*

The calculation procedure, in the case of limited experiments, for the  $E_d$  was performed utilizing the following equation [63],

$$E_d = RT_{max}(BT_{max} - 1) \quad \text{Eq. 11}$$

where,  $R$  is the gas constant,  $T_{max}$  is the maximum peak temperature, and  $B$  is a constant that is material-dependent.  $B$  was calculated from data presented in a previous publication for SHT + Aged Monel K-500 alloy [43]. Then, the subtraction of the low temperature,  $E_{dl}$ , from the high temperature desorption peak energy,  $E_{dr}$  represent the  $E_b$  for the grain boundary. However, to detect the binding energy of the grain boundary without interference from other traps, the  $\gamma'$  particles were solutionized in accordance with the Special Metals data sheet [1] at a selected temperature of 1010 °C during forty minutes and WQed to impede  $\gamma'$  precipitation. The specimen was extracted from the TR 2 heat and prepared to a thickness of 300  $\mu\text{m}$ . Heat treatments performed during shorter periods of time were tested to make sure that the hardness of the specimen decreased due to precipitate dissolution and that the grain boundaries did not grow. Then, the specimens were electrochemically charged with hydrogen in 0.6 M NaCl (pH: 8.0 by adjustment with NaOH) during 7 days applying a potential of -1.0  $V_{SCE}$ . One of these specimens was analyzed using the TDS right after charging and another one was tested after hydrogen desorption at 25 °C during 6 days.

## Results

### *Time to Failure and Maximum Remote Stress after SSRT*

Figure 18 displays the time to failure (TTF) and the maximum remote stress of the different heats during concurrent charging/SSRT test after electrochemical H charging in deaerated 0.6 M NaCl (pH: 8.0 by adjustment with NaOH) during 48 hours at -0.850, -0.950, -1.0 and -1.1  $V_{SCE}$ . The average TTF ranged between 14.30 and 34.14 h. The effect of cathodic polarization on TTF was evaluated testing TR 2 and Allvac heats. TTF was found to decrease as the cathodic polarization potential decreases for both heats, which is consistent with the expectation of intergranular HEAC at high hydrogen overpotentials. In addition, analysis of this parameter shows a higher susceptibility of TR 2 to HEAC than Allvac at every potential tested, except at -0.850  $V_{SCE}$ . At this potential the TTF is the same for both heats. The TTF values for the four heats are displayed in Figure 2 after the test was performed at -1.1  $V_{SCE}$ . The results elucidate the following order in terms of TTF, TR2 < Allvac ~ NRL LS < NRL HS. This order represents the hydrogen embrittlement assisted cracking (HEAC) resistance.

In terms of the maximum stress, this parameter was calculated taking into consideration the cross sectional area at the ends of the specimen next to the thread, to yield the maximum remote stress. The calculated values were in the order of 129.50 to 387.07 MPa. The Allvac lot was always found to fail at a higher maximum remote stress than TR 2 under cathodic polarization, while the opposite was found under benign conditions (in air). All lots were tested at an applied potential of -1.0  $V_{SCE}$  and it was found that the HEAC most resistant alloy was NRL HS followed by Allvac, NRL LS and TR 2, which correlates well with the TTF results at the same applied potential. It is interesting to note that the TTF did not trend with hardness as discussed below.

### *SSRT Fractography*

The fractography of the edge of the notched cylindrical specimens subjected to SSRT for the Allvac and TR 2 lots is presented in Figure 19. The failure modes for the benign (in air) and less aggressive wet conditions (-0.850  $V_{SCE}$ ) are characterized as micro-void dimple fracture for both lots, while under the most aggressive condition (-1.1  $V_{SCE}$ ) the failure mode is characterized as inter-granular (IG) fracture at the edge of the sample with a ductile stress overload in the center of the specimen for both lots. However, the failure mode becomes distinctive at an applied potential of -0.950  $V_{SCE}$ . Under this condition the fractography is represented as micro-void dimple fracture for Allvac lot, while it is characterized by a mixed micro-void dimple/IG fracture for the TR 2 lot. This observation confirms the

TTF and maximum remote stress results that indicate a higher HEAC susceptibility for TR 2 when compared to Allvac.

The fractography for NRL LS and HS is displayed in Figure 20. The fractography revealed differences in the fracture behavior of these lots. The failure mode was characterized by IG cracking for NRL LS lot, while it consisted of a mixed IG/trans-granular (TG) failure mode for NRL HS lot.

*Local Chemistry Characterization of Grain Boundaries via AES after SSRT at -1.1 V<sub>SCE</sub> and Trace Elements present in the Bulk*

After SSRT test at an applied potential of -1.1 V<sub>SCE</sub> at least two grain boundaries from each heat were chemically characterized using AES. Figure 21a presents an example of the spectra taken for at least two grain boundaries on the fracture surface of the different heats after the test, the concentration profile characterization as atomic percent and the normalized concentration profile characterization with respect to a depth of 21 nm (near the bulk value) to address the fluctuation of the elemental concentration at the grain boundary. Figure 21a-d display the normalized concentration profiles for the different heats. All the grain boundaries' surfaces presented a superficial layer composed of O, C and S. The oxygen and carbon peaks are the result of the C deposition from the atmosphere that the fracture surfaces experience as soon as the SSRT setup is de-assembled and handled. In terms of the oxygen, this element is present as result of the formation of an air oxide as soon as the new surfaces are depolarized and are in contact with the air or solution. All heats indicated sulfur enrichment represented by a S peak at depths between 0.93 and 2 nm as shown in Figure 21a-d and Table 3. The S concentration was also evaluated as a raw and normalized S/Ni ratio to obtain a more representative level when analyzing the sulfur level on grain boundaries where different elements were measured. The sulfur composition at the grain boundary for the different heats was found to be in between 1.71 and 4.12 at%. The maximum value was found on the Allvac heat, which does not correlate with HEAC resistance results. When the S composition was normalized to a depth of 21 nm, the maximum level of sulfur was found on NRL LS, which it is not the most HEAC susceptible heat. Another approach to interpret the data is to use the ratio of the element with respect to the base element to avoid any variations attributed to the presence of small amounts of different elements among the heats. In this case, the maximum S/Ni values did not correspond, in some instances, to the maximum S concentration depth. However, the maximum S/Ni level agreed with the maximum S concentration and was found on the Allvac grain boundary, but did not correlate with the HEAC susceptibility. This lack of correlation of S segregation with HEAC susceptibility was also confirmed with observation of the S/Ni ratio normalized to a depth of 21 nm.



**Error! Reference source not found.** presents the values of surface area of grain boundary to volume ratio [36]; trace elements content as expressed above [36] pertaining to the deleterious or enhanced effect of these elements with respect to HE susceptibility. The deleterious and gettering effects of the trace elements were evaluated utilizing Equations 1 and 3. The equilibrium sulfur concentration as described elsewhere was found to be in the range 5.2 to 20 ppm, being the most HEAC resistant heat, NRL HS, the material with the highest equilibrium sulfur concentration. In terms of the gettering factor, a higher value represents an enhanced circumstance where the available sulfur in the microstructure would have a higher probability of being gettered and therefore can not segregate to grain boundaries. The gettering factor was found within 49 and 86.3 ppm, which represent the values for Allvac and NRL LS heats, respectively. These results alone do not correlate well with HEAC susceptibility evaluated through SSRT metrics. Therefore, taking into consideration the deleterious or beneficial effects of certain trace elements, an equation was formulated to try to explain the effect of trace elements on the segregation and gettering of elements and its interaction with HEAC susceptibility. The equation used gives the same weight to S, Sb, Sn, as detrimental elements, and to Hf as beneficial element in combination with a third of the weight of Zr (also a beneficial element). The sum of the deleterious elements was given by (+) while beneficial elements were subtracted (-). This yielded a single bulk compositional parameter in an attempt to shed light on the combined effect of trace elements on HE susceptibility. The  $S+Sn+Sb-Hf-Zr/3$  values were TR-2 -97.0; NRL LS - 76.7; Allvac -121.3; and NRL HS -197.9 when expressed in ppm concentrations given as a sum. Here the maximum value of this parameter was obtained for the heat more susceptible to HE. The use of this factor for the different heats evaluated provided the following order, NRL HS < Allvac < NRL LS < TR 2, which correlates exactly with the HE susceptibility trend found previously by SSRT (Figures 2 and 3). In addition, the surface area of grain boundary and hence trap and segregation site density on boundaries compared to the volume ratio followed the trend TR 2 < NRL LS < Allvac < NRL HS, which also agreed with the HE susceptibility order assessed by TTF metric from SSRT experiments. Hence, the segregation parameter in combination with the density of grain boundary trap or segregation sites per unit volume appears to indicate the susceptibility.

#### *Electrochemically driven Hydrogen Production on Heats Surfaces*

The hydrogen evolution reaction kinetic was addressed by calculation of the Tafel slope from potentiodynamic polarizations performed in the cathodic regime in deaerated 0.6 M NaCl at pH 8.0 by adjustment with NaOH (Figure 23a). The cathodic polarization presented two distinct kinetic behaviors. At the higher potentials mass transfer control prevails until a potential of  $-0.8 V_{SCE}$ , approximately, where there is a transition to charge transfer control. This critical potential is below the Nernst potential for

hydrogen evolution at the electrolyte pH (-0.713 V<sub>SCE</sub>). The Tafel slope was calculated from the charge transfer control portion of the curve as shown in Figure 23b. The experimental hydrogen production rates were found to be similar among the different heats and between -0.233 and -0.222 V/decade. The heat to heat variations did not affect this parameter.

#### *Diffusible and Total Hydrogen Concentration via Barnacle Cell and LECO, respectively*

Regarding the hydrogen concentrations and trapping, Figure 24 displays the effect of hydrogen overpotential on diffusible and total hydrogen concentration for the different heats after electrochemically charging with hydrogen during 7 days in 0.6 M NaCl (pH:8.0 by adjustment with NaOH). Both concentration parameters were found to increase with hydrogen overpotential. The Allvac heat was observed to exhibit lower total and diffusible hydrogen concentrations over a range of cathodic potentials. As expected, the total hydrogen concentration  $C_{H,Total}$  was larger than  $C_{H,Diff}$  as typically observed [43]. This behavior is related to the fact that hydrogen not only interacts with the crystal lattice, but also with low and high binding traps, such as: dislocations [44, 45], grain boundaries, carbides [42], microvoids, age hardening precipitates like  $\gamma'$  [43, 44, 64], among others. In terms of the heat to heat variation, for both,  $C_{H,Total}$  and  $C_{H,Diff}$  there is limited difference, except for the Allvac heat. This heat consistently exhibited hydrogen concentration values near the lower bound of all other heats or statistically lower hydrogen levels based on repeated measurements at some overpotentials.

#### *Trap Binding States and Desorption and Binding Energies*

The total, lattice, as well as the  $\gamma'$  trap binding energy of the different heats were determined from ramped TDS experiments executed at different heating rates (3, 5, 7.5 and 10 °C/min). Figure 25 displays the normalized hydrogen pressure versus time for as-received and baked TR2 specimens. Hydrogen is indicated by peaks with one or more maxima observed. In this case, the experiment elucidates the intake of hydrogen by the TR 2 heat while it was exposed in seawater under cathodic polarization, while the TR 2 specimen baked at 450 °C indicates no peak. This baking procedure was performed in all the samples during 48 hours prior electrochemical charging for all the H-interaction tests mentioned in this manuscript, except for the experiments pertaining to the calculation of the hydrogen production rate.

The hydrogen desorption rate data for the Allvac (Figure 26a), TR 2 (Figure 27a), NRL LS (Figure 28a) and NRL HS heats (Figure 29a) presented the same characteristic behavior for all the heats, that is, a curve with two maxima, which represent two hydrogen states or trap states. The peaks identified on each heat for the hydrogen desorption rate as function of temperature experimental data were deconvoluted using OriginPro 7.5 software. The presence of these two states in the Monel K-500 heats

tested is in agreement with previous information reported on solution heat treated (SHT), aged and SHT, cold worked, aged Monel K-500 materials [43]. These peaks are also present for samples pre-charged at all the different potentials, mentioned previously, as shown in Figure 30 for example when all the heats were pre-charged at a potential of  $-1.1 V_{SCE}$ . The peak at higher temperature was previously identified as the  $\gamma'$  interface trap and it was found to be smaller than the area under the left peak at lower temperatures attributed to lattice hydrogen and low energy reversible traps [43]. The area under both peaks for this plot of hydrogen desorption rate vs temperature represents the total hydrogen concentration for each heat, which follows this order, Allvac < NRL HS < NRL LS < TR 2. This technique corroborates the finding that Allvac was the heat with less diffusible hydrogen concentration, with respect to the other heats, after pre-charging at the same condition in electrochemical extraction (Figure 24). The desorption peak temperatures measured with TDS at the different heating rates after pre-charging at  $-1.0 V_{SCE}$  were found to increase with the heating rate, which is the expected behavior for a thermally controlled desorption process [65, 66]. This behavior has been reported previously [43]. The different  $E_d$  values were calculated from the slope of the linear regression of the heating rate - desorption peak temperatures pairs for Allvac (Figure 26b), TR 2 (Figure 27b), NRL LS (Figure 28b) and NRL HS heats (Figure 29b) and were reported at the 95 % confidence interval for each heat. The left and right  $E_d$  values are presented in Table 4 and show that  $E_{d,l}$  average values range in between 23 and 34 kJ/mol and follow Allvac < TR 2 ~ NRL-LS < NRL-HS. The value range presented in this investigation approximately overlaps with that reported previously for Monel K-500 alloys [43]. The  $\gamma'$  binding energy was calculated from the subtraction of  $E_{d,l}$  from  $E_{d,r}$ . The average values for the binding energies for  $\gamma'$  were found in the range 7.75 to 19.1 kJ/mol in the following ascending order: NRL HS < TR 2 < Allvac < NRL LS (See Table 4).

Additional experiments focused on elucidation of grain boundary trap binding energy. The results and a comparison with the original TR 2 heat are presented in Figure 31. The resolutionized materials present two trap binding states, one at approximately 200 °C, which agrees with the left peak assigned to lattice sites for the non-resolutionized material and another one at 350 °C, which should correspond to the grain boundary trap sites since the peak representing the  $\gamma'$  trap sites is no longer present as result of the SHT + WQ heat treatment at 1010 °C during 40 mins. The  $E_d$  for the 350 °C peak was found to be 55.0 kJ/mol while the  $E_d$  for the 200 °C peak was 30.7 kJ/mol, both were calculated using Eq. 11 and the B constant (0.01863) calculated from data presented in a previous publication for SHT + Aged Monel K-500 alloy [43]. Therefore, subtraction of the high temperature  $E_d$  from the low temperature  $E_d$  results in a  $E_b$  of approximately 24.3 kJ/mol for trap sites assigned to grain boundaries, which is above the  $E_b$  for the  $\gamma'$  trap for the TR 2 heat (Table 4).

### *Effective Hydrogen Diffusivity Calculation via Saturation Curve Analysis utilizing TDS*

Saturation curves were constructed measuring the total mass of hydrogen in pre-charged NRL heats in seawater at an applied potential of -0.800, -0.850, -0.890 and -1.000  $V_{SCE}$  during different time intervals ( $M_t$ ) until saturation ( $M_\infty$ ). The  $M_t/M_\infty$  ratios are plotted against time in Figure 32. The time needed for saturation was approximated utilizing diffusion models for semi-infinite cylindrical geometry for a saturation of 90% and a  $D_{H,eff}$  of  $1.3 \times 10^{-10} \text{ cm}^2/\text{s}$  [56]. In addition, theoretical curves were calculated using Eq. 8 and are presented in Figure 32. The experimental data was found to oscillate between the theoretical saturation curves for a hydrogen diffusivity of  $5 \times 10^{-11}$  and  $2 \times 10^{-10} \text{ cm}^2/\text{s}$ , except for one data point, and presents the best fit for a hydrogen diffusivity of  $1 \times 10^{-10} \text{ cm}^2/\text{s}$ . A few additional experiments were performed for the TR 2 and Allvac heats on a plane sheet geometry (not shown in the plot). The data points suggest that the hydrogen diffusivity of these heats does not exceed the one for NRL materials. Hence, differences in hydrogen diffusion rate are not likely the factors accounting for differences in HE susceptibility

## **Discussion**

### *Factors effecting hydrogen embrittlement susceptibility*

The susceptibility of Monel K-500 to HEAC is controlled by hydrogen [15]. Hydrogen embrittlement is clearly exacerbated by cathodic potentials which increase the hydrogen overpotential and in turn hydrogen uptake as discussed below [43]. Large increases in trapped and lattice H as a function of hydrogen overpotential were indicated in 0.6 M NaCl in previous TDS investigations [43]. Moreover, prior publications predicted significant effects of hydrogen on  $K_{th}$  and stage II crack velocity,  $[da/dt]_{II}$  [15, 36]. There is a threshold based on  $C_{H,crit}$  above which stage II crack velocity increases markedly.  $K_{Th}$  decreases monotonically at potentials negative to about -0.800 to -0.900  $V_{SCE}$  depending on hydrogen concentration, Griffith fracture toughness and yield strength [15, 36] .

Recall that TR 2 material was harvested from seawater deployment where HEAC was observed and hydrogen was detected upon retrieval from service (Figure 25). It is clear from the data indicated herein that TR 2 and NRL LS exhibit greater susceptibility to hydrogen embrittlement as evidenced by lower breaking stresses, times to failure in SSRT (Figure 18) as well as by fractography (Figure 19c and d and Figure 20) which indicates a greater extent of intergranular fracture even at less severe cathodic potentials. Allvac exhibits slightly less embrittlement susceptibility but is clearly embrittled for instance



at -1.1 V<sub>SCE</sub> while remaining somewhat more resistant at -0.95 and -0.85 V<sub>SCE</sub> (Figure 18 and Figure 19b and c). This susceptibility trend and lot-based difference was also seen in fracture mechanics based environment assisted cracking under identical conditions [36]. The purpose of this paper is to attempt to identify factors controlling these lot-to-lot differences based on metallurgical factors. These issues are more relevant at intermediate potentials<sup>14</sup> as clearly all Monel K-500 lots tested are embrittled at -1.1 V<sub>SCE</sub> and this is consistently observed in past studies [4, 21, 67]. More rapid time to failure and lower breaking stress for TR 2 and NRL LS does not appear to correlate with hardness as indicated in Figure 33.

Concerning hydrogen parameters, all materials exhibited similar hydrogen production rates as indicated by Figure 23. However, TR 2 and NRL LS exhibited enhanced C<sub>H,diff</sub> and C<sub>H,total</sub> relative to the Allvac material but not NRL HS (Figure 24). The trend in C<sub>H,diff</sub> follows the lot-to-lot hardness data shown in Figure 33 with the exception of the Allvac material which is harder than NRL LS but absorbed markedly less hydrogen. The trend towards an increase in C<sub>H,diff</sub> with hardness could correspond with a higher density of reversible trap sites in the harder material. The  $\gamma'$  trap binding energy decreases with increasing hardness (Figure 35) suggesting some H interchange with lattice sites and participation in C<sub>H,diff</sub> for these weaker sites [43]. The decrease in  $\gamma'$  binding energy with hardness could be explained by slight change in precipitate-lattice coherency or in the density of strongly bound sites on these particles [45]. Other parameters in hydrogen analysis are similar such as hydrogen diffusion coefficient. A difference between hydrogen diffusion in NRL heats, Allvac and TR 2 materials was not detected.

This trend in susceptibility is also supported by near-grain boundary sulfur analysis from Auger Electron Spectroscopy and bulk chemistry. First, it should be noted that all materials contain sulfur (Table 1) at concentrations above the reported solubility limits for S in Ni at aging temperatures [67, 68]. Also, all alloys exhibit near surface enhancements in sulfur content to various extents which falls rapidly with depth as seen previously for Ni (Figure 21a-d) [68, 69]. What is interesting to note, though is that the alloys tested have drastically different ratios of grain boundary embrittling species like sulfur and beneficial gettering species such as Hf, Zr, Mg and Ca or Boron [12, 23, 34]. These elements may getter sulfur by forming sulfo-carbides [12, 34] and sulfides [23]. It is interesting to note that a combination of a lower S+Sb+Sn-Hf-Zr/3 parameter with a low ratio of surface area of grain boundary to the volume is found for the less susceptible materials such as Allvac (**Error! Reference source not found.**). However, it should be noted that grain-to-grain differences in near grain boundary surface peak sulfur, S/Ni ratio

---

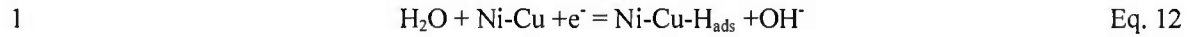
<sup>14</sup> Low voltage anodes are sought to provide adequate levels of cathodic protection for steel structures yet not be too severe so as to embrittle MK500 fasteners in seawater.

and normalized quantities do not indicate a clear trend in sulfur segregation (Table 3). This is likely due to carbon contamination confounding analysis and the fact that sulfur content varies by grain.

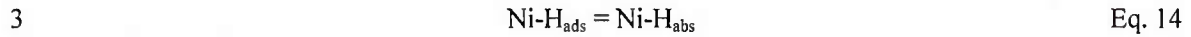
Each of these three factors including sulfur segregation, hydrogen uptake and grain boundary trapping as well as hardness are discussed in more detail below.

### *H Interactions and Uptake*

Given similar HER rates on planar electrodes as a function of hydrogen over potential, a difference in the hydrogen production rate is not likely the cause of differences in hydrogen susceptibility. The hydrogen evolution reaction on Ni in alkaline environments during cathodic polarization has been extensively investigated [70-73]. The mechanism involves rate determining slow discharge from a water molecule followed by rapid Tafel (chemical) recombination at low currents as shown through the following steps often regarded as the Volmer-Tafel mechanism of the hydrogen evolution reaction mechanism [72]. At high current densities, reaction (2) may be too slow [72] so the reaction mechanism may be coupled. Here, Ni-Cu is taken to represent the Ni-Cu fcc lattice containing the elements listed in Table 1 and is abbreviated as the solvent Ni.



Of course, hydrogen absorption and uptake can occur via a third step. This third step is regarding to be fast relative to slow diffusion in the Ni-Cu fcc lattice and as such is regarded to be at equilibrium:



Hence, the relationship between cathodic potential and hydrogen surface coverage as well as absorbed hydrogen concentration and potential are given as:

$$1 \quad i_1 = k_1 F (1 - \theta_{\text{Ni-H}}) \exp\left(\frac{-\beta \eta F}{RT}\right) \quad \text{Eq. 15}$$

$$2 \quad i_2 = k_2 F (\theta_{\text{Ni-H}})^2 \quad \text{Eq. 16}$$

The Tafel slope of (1) is rate controlling and  $\beta=0.5$  exceeds 118 mV/dec but is non-linear with coverage. Figure 23 is consistent with this prediction. At low coverage and for coupled rates or similar rate determining reaction rates for 1 and 2, it may be shown that the coverage of hydrogen Ni-H<sub>ads</sub> is given by the following reaction and the uptake of hydrogen may be combined to yield the lattice

hydrogen content [74]:

$$(\theta_{Ni-H}) = \left(\frac{k_1}{k_2}\right)^{1/2} \exp\left(\frac{-\beta\eta F}{2RT}\right) \quad \text{Eq. 17}$$

$$C_{H,lattice} = \frac{k_{abs}}{k_{des}} \theta_{Ni-H} \quad \text{Eq. 18}$$

$$C_{H,lattice} = \theta_{H-lattice} N_{lattice} = \frac{k_{abs}}{k_{des}} \left(\frac{k_1}{k_2}\right)^{1/2} \exp\left(\frac{-\beta\eta F}{2RT}\right) \quad \text{Eq. 19}$$

where,  $k_{abs}$ ,  $k_{des}$ ,  $k_1$ , and  $k_2$  are all rate constants,  $\eta$  is the hydrogen overpotential while  $R$ ,  $T$ , and  $F$  have their usual meanings. From this equation it can be seen that  $C_{H,lattice}$  is a strong function of hydrogen overpotential, and four rate constants. One or more of these rate constants are most likely altered by heat to heat variations.  $C_{H,lattice}$  is related to  $C_{H,diff}$  taking into consideration weak energy reversible traps such as dislocations, copper solute, twin boundaries, low energy grain boundaries and some weak sites on  $\gamma'$  particles. Finally,  $C_{H,tot}$  represents the sum of the lattice hydrogen and all traps (reversible, irreversible and otherwise) as discussed extensively elsewhere [43].

These factors can all produce further differences due to heat-to-heat variations in the parameters effecting these equations.

$$\theta_{Trap} = \left[ \frac{\theta_{lattice} \exp\left(\frac{E_B}{RT}\right)}{1 + \theta_{lattice} \exp\left(\frac{E_B}{RT}\right)} \right] \quad \text{Eq. 20}$$

$$C_{H,diff} = C_{H,lattice} + \sum_1^N C_{Hrevtrap} \quad \text{Eq. 21}$$

$$C_{HDiff} = C_{H,lattice} + \theta_{dislocations}(N_{dislocations}) + \theta_{weak\gamma'}(N_{weak\gamma'}) + \theta_{weakgb}(N_{weakgb}) \quad \text{Eq. 22}$$

where  $\theta$  is the fractional trap site coverage and  $N$  is the trap site density,  $\theta_{lattice}$  is given by  $C_L/N_L$ , expressed as atoms/interstitial site or as a fractional coverage. In these equations, it can be seen that the combination of reversible trap site density and coverage dictated by binding energies,  $E_B$ , of each specific “weak” trap site where hydrogen is mobile and in equilibrium with lattice sites determines  $C_{H,rev trap}$  from each weak trap. The  $\gamma'$  binding energy was calculated from the subtraction of  $E_{d,l}$  from  $E_{d,r}$ . The average values for the binding energies for  $\gamma'$  ranged from 7.8 to 19.1 kJ/mol in the order: NRL HS < TR 2 < Allvac < NRL LS. The ~8 kJ/mole value may be regarded as reversibly trapped hydrogen [75] at  $\gamma'$  precipitates while the trapping near ~19 kJ/mole may be irreversible at short times. This weakly trapped

hydrogen in combination with  $C_{H,lattice}$  determine  $C_{H,diff}$ . The status of grain boundaries as traps is unclear since when  $E_B$  is high such as might be seen on high angle boundaries; grain boundary traps may be irreversible but likely represent a combination of reversible and irreversible sites depending on boundary angle, segregation and degree of misfit. It should be noted that previous work detected no difference in the fraction of low angle boundaries amongst the heats examined [36] suggesting that grain boundary engineering considerations may not explain susceptibility differences [13].

Given a likely  $\beta$  value of 0.5, then the  $C_{H,lattice}$ ,  $C_{H,diff}$ , and  $C_{H,tot}$  of hydrogen may be predicted as a function of hydrogen overpotential  $\eta$  as seen in Figure 24. Based on previous comparison of lattice and diffusible hydrogen determinations [43], the lattice and diffusible hydrogen concentration are similar because of the high lattice solubility for hydrogen in fcc nickel copper and given by the lower curve of Figure 24 (and left hand peaks in Figures 10-14) assuming low energy traps are in equilibrium with lattice interstitial sites. It can be seen that  $C_{H,diff}$  and  $C_{H,Total}$  are indeed exponentially related to hydrogen overpotential (Figure 24). In the case of Allvac, it is likely based on theoretical grounds established above that the pre-exponential factor in Equation 19 is lower while it is higher for TR2 for reasons presently uncertain.

Moreover, the hydrogen coverage at grain boundaries  $\theta_{gb}$  in the fracture process zone for a heat invariant grain boundary trap binding energy would then be decreased owing to the lower  $C_{H,lattice}$  present in Allvac (Figure 24) and this is shown in Figure 36 where for a given grain boundary trap binding energy,  $\theta_{gb}$  is lower when  $C_{H,lattice}$  and equivalently  $C_{H,diff}$  are lowered. This would be the case for Allvac as an example. Also shown in Figure 36 is the effect of grain boundary trap binding energy on  $\theta_{gb}$ . Figure 31 was obtained by resolutionizing to eliminate  $\gamma'$  traps. Recall that a value of approximately 24.3 kJ/mole was determined in resolutionized TR2 Monel K-500 from Figure 31. A reasonable theoretical range from 10-30 kJ/mole is considered in Figure 36.<sup>15</sup> A higher grain boundary trap binding energy results in a higher coverage. Previous results by EBSD show a similar fraction of low and high angle grain boundaries across all heats [36]. Therefore, an argument cannot be made that  $E_B$  is greater in any particular heat based on differences in grain misorientations. The potential for low S segregation, high sulfur gettering element content, and high grain boundary surface to volume ratio could indeed lower the grain boundary trapping and/or hydrogen activity in the Allvac heat rendering it more difficult to reach

<sup>15</sup> It should be noted that the possibility exists that any given high angle boundary traps hydrogen with a greater trap binding energy that is undetected by TDS of polycrystalline material. This is because any single boundary type represents too low of a number of trap sites for detection by TDS and only a large number of traps sites with a binding energy above the lattice desorption energy can be detected.



high  $\theta_{gb}$  in Allvac and comparatively easier in TR2 and NRL LS. The sulfur issue is complex and should be discussed in further detail below.

#### *Grain boundary Segregation of Sulfur and Hydrogen - Trace Elements Effects*

Sulfur is observed to segregate to grain boundaries in nickel and nickel based alloys [1, 8, 9, 14, 23, 24, 32, 68, 69, 76, 77]. Auger compositional analysis is difficult on grain boundaries owing to carbon contamination, differences in grain boundary inclination relative to incident electron beam and auger electron take off angle, machine specific sensitivity factors for elements, and many other factors [68, 69]. However, the equilibrium sulfur coverage at boundaries may be estimated in Ni as a function of the sulfur solubility [22, 68]. Here we estimate the sulfur grain boundary atomic fraction based on McLean theory [78]. Use of this theory is supported by Auger data which shows narrow surface enhancements of S which fall rapidly with sputter depth. The sulfur solubility can be estimated for equilibrium sulfur segregation with an activation energy  $E_s$  of 72.8 kJ/mole and at the aging temperature of 866 K [68].

$$C_{gb}^S = \left[ \frac{C_{bulk}^S \exp\left(\frac{E_s}{RT}\right)}{1 + C_{bulk}^S \exp\left(\frac{E_s}{RT}\right)} \right] \quad \text{Eq. 23}$$

where,  $C_{bulk}^S$  is the bulk equilibrium sulfur concentration expressed as an atomic fraction and  $C_{gb}^S$  is the sulfur content of grain boundaries. The bulk sulfur concentration in Ni and similarly Ni-10Cu are both about  $30 \times 10^{-6}$  at fraction at 866 K which is lower than the sulfur contents of all alloys tested (Table 1) [68]. Use of the equilibrium concentration at 866 K, e.g., the aging temperature, yields an equilibrium sulfur segregation atomic fraction of 0.42.<sup>16</sup> This implies that every heat of Monel K-500 would be expected to exhibit equal sulfur segregation not accounting for crystallographic effects on  $E_s$ . However, Hf concentration as well as Al in Ni lower the S bulk solubility such that the bulk content may only be  $30 \times 10^{-6}$  at fraction at 866 K [68]. This produces a dramatic decrease in  $C_{gb}^S$  to only 0.069 atomic fraction. It is interesting to note that this estimation is in some agreement with experimental data. Thus the joint effect a of high gettering elements that also effect S solubility such as Hf and to a lesser extent Zr, Ca, and Mg, may exert a substantial effect on equilibrium segregation tendency explaining the great resistance of Allvac and NRL HS Monel K-500.

<sup>16</sup> Mujlford reports that equilibrium segregation at the aging temperatures for Monel K-500 in <40 hours. It should also be noted that peak equilibrium segregation of sulfur is both predicted and measured in the aging range [68] R.A. Mulford, Grain-Boundary Segregation in Ni and Binary Ni-Alloys Doped with Sulfur, Metall Trans A, 14 (1983) 865-870..

### *Prediction of Breaking Stress and Influence of Parameters discussed above*

The breaking stress can be calculated as a function of the hydrogen content and based on the lower hydrogen levels in Allvac and possibility lower segregated sulfur levels predict the trend seen in Figures 2, 3 and 4. An unresolved issue concerns whether or not co-segregation of atomic hydrogen is required [1], and whether co-segregation of hydrogen and sulfur act in an additive manner [32, 79-81] or synergistically [1, 8, 82] to embrittle boundaries. The atomistic process by which interface strength is reduced by a foreign atom is debated. The decohesion model proposes that a sufficient enrichment of hydrogen or sulfur at boundaries causes a discernible weakening of bonds between adjacent atoms [83]. If hydrogen and sulfur accumulate at a planar defect, then the decohesive strength is lowered [26] selectively along that interface. This can lead to preferential breakage of bonds given sufficient applied stress [84, 85]. Embedded atom calculations show that a  $\Sigma 9$  (221) tilt boundary in nickel experiences a decrease in cohesive strength from 18 to 8 GPa when the segregated monolayer coverage increases from  $1 \times 10^{-17}$  to  $6 \times 10^{-16}$  H atoms/cm<sup>2</sup> [85]. Various expressions have been used to describe how grain boundary fracture stresses are each reduced by such impurity segregation. The general form of these expressions, as first described by Akhurst [38] and Briant [16] gives a linear relationship between fracture stress and hydrogen, Enos reported a logarithmic relationship [86, 87]. Herein the following relationship describes the behavior seen in Figure 2 using the exponential uptake law given in Eq. 19 and the fracture criterion expressed below.

$$\sigma_{fracture} = \sigma_0 - \alpha_H \log\left(\frac{C_{H,diff}}{C_{H,diffo}}\right) - \beta_S \log\left(\frac{C_{sulfur}}{C_{sulfuro}}\right) \quad \text{Eq. 24}$$

$$\sigma_{fracture} = \sigma_{applied} \quad \text{Eq. 25}$$

where  $\alpha_H$  is a potency factor for hydrogen,  $\beta_S$  is a potency factor for sulfur along the lines of elsewhere [15, 36],  $\sigma_0$  is the notch breaking stress in air or at minimal  $C_{H,diffo}$  and  $C_{sulfuro}$  below the levels for intergranular cracking.  $\sigma_{fracture}$  is the fracture stress which causes intergranular cracking when equaled by the applied stress. This expression may be modified for the stress field of the notch as follows; the  $C_{H,diff}$  could be modified by the tensile triaxial stress field, the sulfur content could be modified by the boundary content, and the applied stress could be given by the local stress concentration instead of remote stress. The local applied stress can be raised to  $\sigma_{fracture}$  as a function of the geometric stress concentration (e.g., notch or crack tip radius), plastic flow characteristics of the material, as well as global and local plastic constraint. Equation 24 does not predict a critical impurity or hydrogen concentration threshold, yet one may still be observed. This is because it is reasonable to assume that some grain

boundary hydrogen concentration will decrease  $\sigma_{fracture}$  below some other critical stress or strain associated with the criteria for intergranular fracture, otherwise a transition from ductile to intergranular cracking seen in Figure 3 is not seen. Another issue is whether the mean or the extreme value of local concentrations determined from the distribution of measured values should be used. The distribution is expected due to various crystallographic grain boundary mis-orientations that alter segregation tendencies on certain grain boundaries

Moreover, all of the factors discussed above reflected in heat-to-heat variations are either incorporated in Eq. 24-25, including hydrogen sulfur segregation and yield strength, or captured above in the relationships for sulfur segregation and hydrogen absorption that are inputs to this equation. As absorbed hydrogen and equilibrium sulfur content increase then the H and S trapped on boundaries increases, subsequently  $\sigma_{fracture}$  decreases. Yield strength increases the local value of the applied stress,  $\sigma_{applied}$  at any given applied remote stress. It can be seen by exercising this relationship that Allvac and NRL HS are more resistant while TR2 and NRL LS are less resistant. It can also be seen that yield strength is not necessarily a dominant factor in this case although usually an important factor in hydrogen embrittlement.

## Conclusions

Monel K-500 (63%Ni, 33 %Cu, 3.15 %Al, wt. %) was susceptible to hydrogen embrittlement under severe cathodic polarization (e.g., -1.1 V<sub>SCE</sub>) in seawater in all heats of aged material that were within a federal specification. Differences between field susceptible heats and others explored and compared. Monel K-500 harvested from field failures cracked intergranularly more readily at modest levels of cathodic applied potentials. Moreover, the extent of intergranular fracture increased with more negative applied potentials. More facile intergranular fracture correlated with sulfur segregation and extent of applied cathodic potential. H absorption increased strongly with hydrogen overpotential and was not a simple function of hardness for material within the specification. Various assessments of hydrogen concentration, by three investigators all show that Allvac (high HEAC resistance at -0.850 and -.950 V<sub>SCE</sub>) absorbs less hydrogen than harvested materials from field failures and does not crack intergranularly at -.950 V vs. SCE.. Moreover, grain boundary chemistry was assessed after aging and hydrogen fracture by Auger Electron Spectroscopy. Some degree of sulfur enrichment was observed in all heats. The heats observed to crack in seawater and field testing contained unfavorable concentrations of trace detrimental grain boundary segregating elements relative to beneficial sulfur gettering elements in combination with a low density of grain boundary trap or segregation sites per unit volume. Other

hydrogen metal interactions such as trapping and diffusion rate could were not key metrics indicting susceptibility. Greater susceptibility is traced to enhanced hydrogen uptake and speculated grain boundary sulfur enrichment based on a balance of alloy trace chemistries coupled with grain boundary trapping of hydrogen supplied from the lattice and possibly lower energy  $\gamma'$  trap sites which absorbed hydrogen. Material hardness within the limits from Rockwell C 28 to 36 were not found to be the dominant factors in HE susceptibility.

### **Acknowledgements**

This research was sponsored by ONR Grant N00014-12-1-0506 with Dr. Airan Perez as Scientific Officer. Jennifer Gaies and Derek Horton are thanked for the supply of materials. Helpful discussions with Prof. Richard Gangloff, Jiahe Ai, Justin Dolph and testing by Ms. Cary Wingo and MacKenzie Jones are gratefully acknowledged.



## REFERENCES

- [1] D.H. Lassila, H.K. Birnbaum, INTERGRANULAR FRACTURE OF NICKEL - THE EFFECT OF HYDROGEN-SULFUR CO-SEGREGATION, *Acta Metallurgica*, 35 (1987) 1815-1822.
- [2] G.K. Dey, P. Mukhopadhyay, PRECIPITATION IN THE NI-CU-BASE ALLOY MONEL K-500, *Materials Science and Engineering*, 84 (1986) 177-189.
- [3] J.A. Harris, C.D. Stephens, Scarberr.Rc, EFFECTS OF HYDROGEN ON ENGINEERING PROPERTIES OF MONEL NICKEL-COPPER ALLOY K-500, *Corrosion*, 28 (1972) 57-&.
- [4] K.D. Efrid, Failure of Monel Ni-Cu-Al Alloy K-500 Bolts in Seawater, *Mater Performance*, 24 (1985) 37-40.
- [5] C.E. Price, R.S. Fredell, A Comparative-Study of the Embrittlement of Monel-400 at Room-Temperature by Hydrogen and by Mercury, *Metall Trans A*, 17 (1986) 889-898.
- [6] L.H. Wolfe, M.W. Joosten, Failures of nickel/copper bolts in subsea application, *SPE production engineering*, 3 (1988) 382-386.
- [7] W.C. Johnson, J.E. Doherty, B.H. Kear, A.F. Giamei, Confirmation of sulfur embrittlement in nickel alloys, *Scripta Metallurgica*, 8 (1974) 971-974.
- [8] R.M. Latanision, H. Opperhauser, The intergranular embrittlement of nickel by hydrogen: the effect of grain boundary segregation, *Metall Trans A*, 5 (1974) 483-492.
- [9] E.S. Huron, K.R. Bain, D.P. Mourer, J.J. Schirra, P.L. Reynolds, E.E. Montero, The influence of grain boundary elements on properties and microstructures of P/M nickel base superalloys, 2004.
- [10] B. Geddes, Alloying and Performance, in: B. Geddes, H. Leon, H. Huang (Eds.) *Superalloys*, ASTM International, West Conshohocken, PA, 2010, pp. 59-109.
- [11] E.S. Huron, K.R. Bain, D.P. Mourer, J.J. Schirra, P.L. Reynolds, E.E. Montero, in: K.A. Green, T.M. Pollock, H. Harada, T.E. Howson, R.C. Reed, J.J. Shirra, S. Walston (Eds.) *Superalloys*, TMS, 2004.
- [12] J.M. Walshe, K.P. Gumz, N.P. Anderson, in: N.S. McIntyre (Ed.) *Quantitative Surface Analysis of Materials*, ASTM STP 643, 1978, pp. 72-82.
- [13] T. Watanabe, Grain boundary engineering: historical perspective and future prospects, *Journal of Materials Science*, 46 (2011) 4095-4115.
- [14] W. Swiatnicki, S. Lartigue, M. Biscondi, D. Bouchet, Intergranular sulfur segregation and grain boundary plane in a nickel bicrysta, *Le Journal de Physique Colloques*, 51 (1990) 341-346.
- [15] R.P. Gangloff, H.M. Ha, J.T. Burns, J.R. Scully, Measurement and Modeling of Hydrogen Environment-Assisted Cracking in Monel K-500, *Metall Mater Trans A*, 45A (2014) 3814-3834.
- [16] R. Otsuka, T. Maruno, H. Tsuji, Correlation Between Hydrogen Embrittlement and Hydride Formation in Ni--Cu and Pd--Ag Alloys, in: *International Congress on Metallic Corrosion*, 1984, pp. 270-277.
- [17] Y.D. Park, D.L. Olson, A. Landau, M. Pinkas, Assessment of hydrogen-induced precipitation in a nickel-copper alloy using thermoelectric power, *Corrosion*, 62 (2006) 395-402.
- [18] M.L. Wayman, G.C. Smith, EFFECTS OF HYDROGEN ON DEFORMATION AND FRACTURE OF NICKEL-IRON ALLOYS, *Acta Metallurgica*, 19 (1971) 227-&.
- [19] R.P. Gangloff, Hydrogen Assisted Cracking of High Strength Alloys, in: J.P.a.P. Scott (Ed.) *Comprehensive Structural Integrity*, (New York: Elsevier Science, Elsevier Science, New York, 2003, pp. 31-101.
- [20] R.P. Gangloff, Diffusion Control of Hydrogen Environment Embrittlement in High Strength Alloys, in: A.W.T. N. R. Moody, R. E. Ricker, G. S. Was and R. H. Jones (Ed.) *Hydrogen Effects on Material Behavior and Corrosion Deformation Interactions*, The Minerals, Metals & Materials Society, Warrendale, PA, 2003, pp. 477-497.
- [21] J.R. Scully, M.G. Vassilaros, in: DTNSRDC SME 84-69, 1984, pp. 1-28.
- [22] P. Lejcek, in: P. Lejcek (Ed.) *Grain Boundary Segregation in Metals*, Springer, Berlin, 2010.
- [23] R.T. Holt, W. Wallace, Impurities and trace elements in nickel-base superalloys, *International Metals Reviews*, 21 (1976) 1-24.

- [24] T. Miyahara, K. Stolt, D.A. Reed, H.K. Birnbaum, Sulfur segregation on nickel, *Scripta Metallurgica*, 19 (1985) 117-121.
- [25] G.S. Painter, F.W. Averill, Effects of segregation on grain-boundary cohesion: A density-functional cluster model of boron and sulfur in nickel, *Physical review letters*, 58 (1987) 234.
- [26] R.P. Messmer, C.L. Briant, The Role of Chemical Bonding in Grain-Boundary Embrittlement, *Acta Metallurgica*, 30 (1982) 457-467.
- [27] X. Xie, X. Liu, J. Dong, Y. Hu, Z. Xu, Y. Zhu, W. Luo, Z. Zhang, R.G. Thompson, Segregation Behavior of Phosphorus and its Effect on Microstructure and Mechanical Properties in Alloy System Ni-Cr-Fe-Mo-Nb-Ti-Al in: E.A. Loria (Ed.) *Superalloys 718, 625, 706 and Various Derivatives The Minerals, Metals & Materials Society*, 1997, pp. 531-543.
- [28] M.L. Jokl, J. Kameda, C.J. McMahon, V. Vitek, SOLUTE SEGREGATION AND INTERGRANULAR BRITTLE-FRACTURE IN STEELS, *Metal Science*, 14 (1980) 375-384.
- [29] A. Kimura, H.K. Birnbaum, Hydrogen Induced Grain-Boundary Fracture in High-Purity Nickel and Its Alloys - Enhanced Hydrogen Diffusion Along Grain-Boundaries, *Acta Metallurgica*, 36 (1988) 757-766.
- [30] R.H. Jones, in: R.M.a. Latanision, T.E. Fischer (Eds.) *Advances in the Mechanics and Physics of Surfaces*, Hardwood Academic Publishers, Chur, Switzerland, 1986, pp. 1-70.
- [31] C.D. Taylor, M. Neurock, J.R. Scully, A First-Principles Model for Hydrogen Uptake Promoted by Sulfur on Ni(111), *Journal of the Electrochemical Society*, 158 (2011) F36-F44.
- [32] S.M. Bruemmer, R.H. Jones, M.T. Thomas, D.R. Baer, INFLUENCE OF SULFUR, PHOSPHORUS, AND ANTIMONY SEGREGATION ON THE INTERGRANULAR HYDROGEN EMBRITTLEMENT OF NICKEL, *Metall Trans A*, 14 (1983) 223-232.
- [33] C.L. Briant, H.C. Feng, C.J. McMahon, EMBRITTLEMENT OF A 5 PCT NICKEL HIGH-STRENGTH STEEL BY IMPURITIES AND THEIR EFFECTS ON HYDROGEN-INDUCED CRACKING, *Metall Trans A*, 9 (1978) 625-633.
- [34] H.E. Huang, C.H. Koo, Effect of zirconium on microstructure and mechanical properties of cast fine-grain CM 247 LC superalloy, *Materials Transactions*, 45 (2004) 554-561.
- [35] S. Yamaguchi, H. Kobayashi, T. Matsumiya, S. Hayami, EFFECT OF MINOR ELEMENTS ON HOT WORKABILITY OF NICKEL-BASE SUPER-ALLOYS, *Metals Technology*, 6 (1979) 170-175.
- [36] Z. Harris, J. Dolph, G. Pioszak, B.C. Rincon Troconis, J.R. Scully, J. Burns, The Effect of Microstructure Variation on the Hydrogen Environment-Assisted Cracking of Monel K-500, *Metallurgical and Materials Transactions A*, submitted (2015).
- [37] A. Hirose, Y. Arita, Y. Nakanishi, K.F. Kobayashi, Decrease in hydrogen embrittlement sensitivity of INCONEL 718 by laser surface softening, *Materials Science and Engineering a-Structural Materials Properties Microstructure and Processing*, 219 (1996) 71-79.
- [38] K.N. Akhurst, T.J. Baker, THE THRESHOLD STRESS INTENSITY FOR HYDROGEN-INDUCED CRACK-GROWTH, *Metall Trans A*, 12 (1981) 1059-1070.
- [39] M.T. Wang, Technical Rept. AFML 72-102 Part I in, 1972.
- [40] D.P. Dautovich, S. Floreen, The Stress Corrosion and Hydrogen Embrittlement Behavior of Maraging Steels, in: S.a.o. editors (Ed.) *Stress Cor. Cracking and Hyd. Embrit. of Iron Base Alloys*, NACE 5, Suffern, New York, 1977, pp. 798-815.
- [41] B.A. Kehler, J.R. Scully, Predicting the effect of applied potential on crack tip hydrogen concentration in low-alloy martensitic steels (Reprinted from *Proceedings of the CORROSION/2007 research topical symposium "Advances in Environmentally Assisted Cracking"*, 2007), *Corrosion*, 64 (2008) 465-477.
- [42] D.M. Li, R.P. Gangloff, J.R. Scully, Hydrogen trap states in ultrahigh-strength AERMET 100 steel, *Metall Mater Trans A*, 35A (2004) 849-864.
- [43] J.H. Ai, H.M. Ha, R.P. Gangloff, J.R. Scully, Hydrogen diffusion and trapping in a precipitation-hardened nickel-copper-aluminum alloy Monel K-500 (UNS N05500), *Acta Mater*, 61 (2013) 3186-3199.

- [44] A. Turnbull, R.G. Ballinger, I.S. Hwang, M.M. Morra, M. Psailadombrowski, R.M. Gates, HYDROGEN TRANSPORT IN NICKEL-BASE ALLOYS, *Metall Trans A*, 23 (1992) 3231-3244.
- [45] J.P. Hirth, 1980 INSTITUTE OF METALS LECTURE THE METALLURGICAL-SOCIETY-OF-AIME - EFFECTS OF HYDROGEN ON THE PROPERTIES OF IRON AND STEEL, *Metall Trans A*, 11 (1980) 861-890.
- [46] N.R. Moody, S.L. Robinson, S.M. Myers, F.A. Greulich, DEUTERIUM CONCENTRATION PROFILES IN FE-NI-CO ALLOYS ELECTROCHEMICALLY CHARGED AT ROOM-TEMPERATURE, *Acta Metallurgica*, 37 (1989) 281-290.
- [47] R. Kirchheim, I. Kownacka, S.M. Filipek, Hydrogen Segregation at Grain-Boundaries in Nanocrystalline Nickel, *Scripta Metall Mater*, 28 (1993) 1229-1234.
- [48] R. Kirchheim, Revisiting hydrogen embrittlement models and hydrogen-induced homogeneous nucleation of dislocations, *Scripta Materialia*, 62 (2010) 67-70.
- [49] R. Bayles, T. Lemieux, F. Martin, D. Lysogorski, T. Newbauer, W. Hyland, B.A. Green, E. Hogan, T. Longazel, P. Stencel, Monel K-500 Hydrogen Embrittlement, in, Naval Research Laboratory, 2011.
- [50] W.D. Kingery, H.K. Bowen, D.R. Uhlmann, Atom Mobility, in: *Introduction to Ceramics*, John Wiley & Sons, 1976, pp. 226.
- [51] J.J. DeLuccia, D.A. Berman, An Electrochemical Technique to Measure Diffusible Hydrogen in Metals (Barnacle Cell), in: F. Mansfeld, U. Bertocci (Eds.) *Electrochemical Corrosion Testing*, ASTM STP 727, American Society for Testing and Materials, 1981, pp. 256-273.
- [52] M. Devanathan, Z. Stachurski, The adsorption and diffusion of electrolytic hydrogen in palladium, in: *Proceedings of the Royal Society of London A: Mathematical, Physical and Engineering Sciences*, The Royal Society, 1962, pp. 90-102.
- [53] ASTM E1447-09: Determination of Hydrogen in Titanium and Titanium Alloys by Inert Gas Fusion Thermal Conductivity/Infrared Detection Method, in, ASTM International, 2009.
- [54] S.W. Smith, J.R. Scully, The identification of hydrogen trapping states in an Al-Li-Cu-Zr alloy using thermal desorption spectroscopy, *Metall Mater Trans A*, 31 (2000) 179-193.
- [55] S. Smith, in, University of Virginia, 1995.
- [56] J. Crank, *THE MATHEMATICS OF DIFFUSION*, Second ed., Clarendon Press, 1975.
- [57] H.E. Kissinger, Reaction Kinetics in Differential Thermal Analysis, *Analytical Chemistry*, 29 (1957) 1702-1706.
- [58] A. Turnbull, in: R.P. Gangloff, B.P. Sommerday (Eds.) *Gaseous Hydrogen Embrittlement of Materials in Energy Technologies: The Problem, Its Characterisation and Effects on Particular Alloy Classes*, Woodhead Publishing Materials, Oxford, 2012, pp. 89.
- [59] W.Y. Choo, J.Y. Lee, Thermal-Analysis of Trapped Hydrogen in Pure Iron, *Metall Trans A*, 13 (1982) 135-140.
- [60] W.Y. Choo, J.Y. Lee, Hydrogen Trapping Phenomena in Carbon-Steel, *Journal of Materials Science*, 17 (1982) 1930-1938.
- [61] F.G. Wei, M. Enomoto, K. Tsuzaki, Applicability of the Kissinger's formula and comparison with the McNabb-Foster model in simulation of thermal desorption spectrum, *Comp Mater Sci*, 51 (2012) 322-330.
- [62] H.H. Johnson, N. Quick, A.J. Kumnick, Hydrogen trapping mechanisms by permeation techniques, *Scripta Metallurgica*, 13 (1979) 67-72.
- [63] K.Y. Lee, J.Y. Lee, D.R. Kim, A STUDY OF HYDROGEN-TRAPPING PHENOMENA IN AISI-5160 SPRING STEEL, *Materials Science and Engineering*, 67 (1984) 213-220.
- [64] J.E. Angelo, N.R. Moody, M.I. Baskes, TRAPPING OF HYDROGEN TO LATTICE-DEFECTS IN NICKEL, *Modelling and Simulation in Materials Science and Engineering*, 3 (1995) 289-307.
- [65] K. Ono, M. Meshii, HYDROGEN DETRAPPING FROM GRAIN-BOUNDARIES AND DISLOCATIONS IN HIGH-PURITY IRON, *Acta Metallurgica Et Materialia*, 40 (1992) 1357-1364.



- [66] A. Turnbull, R.B. Hutchings, ANALYSIS OF HYDROGEN-ATOM TRANSPORT IN A 2-PHASE ALLOY, *Materials Science and Engineering a-Structural Materials Properties Microstructure and Processing*, 177 (1994) 161-171.
- [67] R.J. Brigham, H. Neumayer, J.S. Kirkaldy, Solubility Limit for Sulphur in Nickel between 637 Degrees C and 1400 Degrees C, *Can Metall Quart*, 9 (1970) 525-&.
- [68] R.A. Mulford, Grain-Boundary Segregation in Ni and Binary Ni-Alloys Doped with Sulfur, *Metall Trans A*, 14 (1983) 865-870.
- [69] B. Ladna, H.K. Birnbaum, Surface and Grain-Boundary Segregation of Sulfur and Boron in Nickel, *Acta Metallurgica*, 36 (1988) 745-755.
- [70] A. Lasia, A. Rami, Kinetics of Hydrogen Evolution on Nickel Electrodes, *J Electroanal Chem*, 294 (1990) 123-141.
- [71] N. Krstajic, M. Popovic, B. Grgur, M. Vojnovic, D. Sepa, On the kinetics of the hydrogen evolution reaction on nickel in alkaline solution - Part I. The mechanism, *J Electroanal Chem*, 512 (2001) 16-26.
- [72] M.A.V. Devanathan, M. Selvaratham, Mechanism of Hydrogen Evolution Reaction on Nickel in Alkaline Solutions by the Determination of Surface Coverage, *Faraday Discussions*, (1960) 1820-1831.
- [73] J.O. Bockris, E.C. Potter, The Mechanism of Hydrogen Evolution at Nickel Cathodes in Aqueous Solutions, *The Journal of Chemical Physics*, 20 (1952).
- [74] B.A. Kehler, J.R. Scully, Predicting the Effect of Applied Potential on Crack Tip Hydrogen Concentration in Low-Alloy Martensitic Steels, *Corrosion*, 64 (2008) 465-477.
- [75] G.M. Pressouyre, Trap Theory of Hydrogen Embrittlement, *Acta Metallurgica*, 28 (1980) 895-911.
- [76] B. Ladna, H.K. Birnbaum, Unusual Segregation Behavior of Boron and Its Effect on Segregation of Sulfur in Nickel, *Jom-J Min Met Mat S*, 39 (1987) A53-A53.
- [77] B. Ladna, H.K. Birnbaum, Unusual Segregation Behavior of Boron and Its Effect on Segregation of Sulfur in Nickel, *J Phys-Paris*, 49 (1988) 441-446.
- [78] D. McLean, Grain boundaries in metals, Clarendon Press, 1957.
- [79] R.H. Jones, S.M. Bruemmer, M.T. Thomas, D.R. Baer, Impurity Segregation and Hydrogen Embrittlement of Fe and Ni, *Jom-J Min Met Mat S*, 34 (1982) 40-40.
- [80] R.H. Jones, S.M. Bruemmer, M.T. Thomas, D.R. Baer, Hydrogen Pressure-Dependence of the Fracture Mode Transition in Nickel, *Metall Trans A*, 14 (1983) 1729-1736.
- [81] R.H. Jones, M.J. Danielson, S.M. Bruemmer, D.R. Baer, M.T. Thomas, Electrochemical and Mechanical Contributions of Segregated Phosphorus to the Igsc of Nickel, *Jom-J Min Met Mat S*, 35 (1983) A61-A61.
- [82] H. Fukushima, H.K. Birnbaum, Surface and Grain-Boundary Segregation of Deuterium in Nickel, *Acta Metallurgica*, 32 (1984) 851-859.
- [83] R.A. Oriani, P.H. Josephic, Equilibrium Aspects of Hydrogen-Induced Cracking of Steels, *Acta Metallurgica*, 22 (1974) 1065-1074.
- [84] N.R. Moody, S.M. Foiles, An Atomistic Study of the Equilibrium Segregation of Hydrogen to Tilt Boundaries in Nickel, *Mater Res Soc Symp P*, 229 (1991) 179-184.
- [85] N.R. Moody, S.M. Foiles, An Atomistic Study of Hydrogen Effects on the Fracture of Tilt Boundaries in Nickel, *Structure and Properties of Interfaces in Materials*, 238 (1992) 381-396.
- [86] D.G. Enos, J.R. Scully, A critical-strain criterion for hydrogen embrittlement of cold-drawn, ultrafine pearlitic steel, *Metall Mater Trans A*, 33 (2002) 1151-1166.
- [87] D.G. Enos, A.J. Williams, Jr., J.R. Scully, Long-Term effects of cathodic protection on prestressed concrete structures: hydrogen embrittlement of prestressing steel, *Corrosion*, 53 (1997) 891-908.
- [88] ASTM, ASTM E2594. Standard Test Method for Analysis of Nickel Alloys by Inductively Coupled Plasma Atomic Emission Spectrometry (Performance-Based Method) in, 2014.



Table 1. Chemical composition in wt% or ppm for Monel K-500 heats (UNS N05500) measured in accordance with ASTM E2594 (ICP-OES) [88], unless otherwise indicated.

Element (wt%)	Ni	Cu	Al	Fe	Mn	Si	Ti	C	Co	Nb	Cr	Mo	W	Sb* (ppm)	Zr* (ppm)	Hf* (ppm)	Mg* (ppm)	S* (ppm)	P* (ppm)	Sn* (ppm)	Pb* (ppm)
Allvac	66.12	28.57	2.89	0.80	0.81	0.08	0.45	0.166	<0.01	-	0.04	<0.01	<0.01	0.64	370	2.6	39	1.6	92	2.4	2.1
TR 2	64.66	30.15	2.73	0.69	0.73	0.094	0.45	0.20	0.044	-	0.062	0.059	<0.005	0.67	330	5.6	130	11	71	6.9	2.5
NRL LS	63.06	30.67	3.45/ 3.47	1.27	0.78	0.075	0.47	0.137	0.026	0.03	-	-	-	0.54	230	2.8	210	0.92	56	1.4	4.8
NRL HS	63.44	30.74	3.20/ 3.20	0.91	0.85	0.096	0.57	0.135	0.015	0.03	-	-	-	0.34	650	0.8	40	17	40	2.2	3.5

\*Trace analysis performed using Glow Discharge Mass Spectrometry.

Table 2. Hardness and grain size values for Monel K-500 heats (UNS N05500) measured in accordance with ASTM E2594 (ICP-OES) [88] and determined from EBSD data and published previously [36].

Heats	HRC	Grain size ( $\mu\text{m}$ )
Allvac	31	13.8
TR 2	$34.1 \pm 0.6$	35.3
NRL-LS	$28.50 \pm 1.63$	22.5
NRL-HS	$36.65 \pm 0.27$	11.2

Table 3. S, normalized S, S/Ni and normalized S/Ni in at % or at%/at% on Monel K-500 obtained via AES analysis on the grain boundaries of the intergranular fracture surfaces resulting from SSRT at -1.1  $V_{\text{SCE}}$  in deaerated 0.6 M NaCl (pH: 8.0 by adjustment with NaOH).

at% or at%/at%	TR2 A1	TR2 A3	Allvac A1	Allvac A2	NRLHS A2	NRLHS A3	NRLLS A1	NRLLS A2	NRL-LS A3
Highest S (at%) Depth (nm)	2.7 1.5 nm	1.7 1.5 nm	3.3 2 nm	4.1 1 nm	3.1 1 nm	3.1 1 nm	1.7 1.85 nm	3.8 0.93 nm	1.9 1.85 nm
S Normalized at 21 nm	3.3	4.0	3.5	11.4	2.2	2.4	2.6	14.6	3.1
S/Ni (max value and location)	0.1 (0.1, 0 nm)	0.0 (0.1, 0 nm)	0.2 (0.2, 1 nm)	0.1	0.2	0.1	0.1 (0.1, 0.9 nm)	0.11	0.1 (0.1, 0.9 nm)
S/Ni Normalized at 21 nm	5.7 (7.7, 0 nm)	4.1 (14.3, 0 nm)	11.4 (12.6, 1 nm)	24.6	6.3	6.7	6.71 (7.6, 0.9 nm)	28.97	4.9 (6.1, 0.9 nm)

Table 4. Measured hydrogen desorption and binding energies for the aged Monel K-500 heats.

	$E_d$ (kJ/mol)		SD (kJ/mol)		$E_B$ (kJ/mol)
	left	right	left	right	
Allvac	23.0	40.6	1.4	0.5	17.7
TR 2	26.4	38.8	0.7	0.7	12.4
NRL LS	26.0	45.0	0.2	0.4	19.1
NRL HS	33.6	41.3	1.6	0.9	7.7

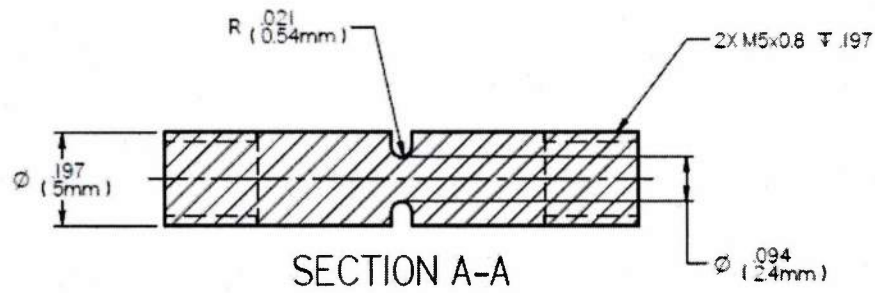


Figure 17. SSRT notched specimen drawing.

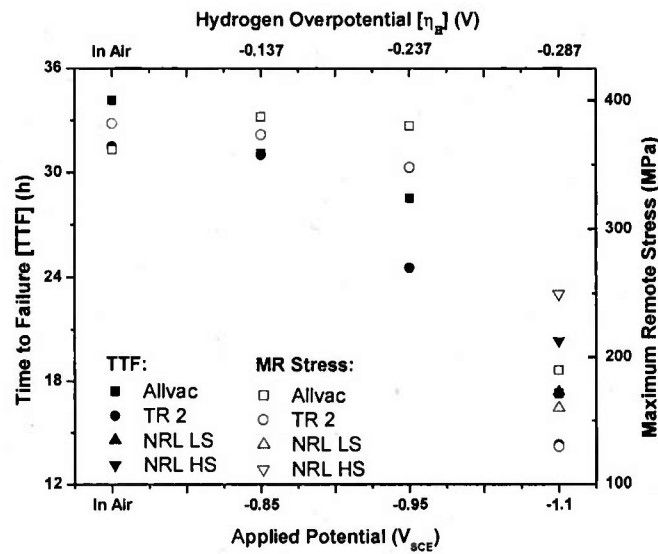
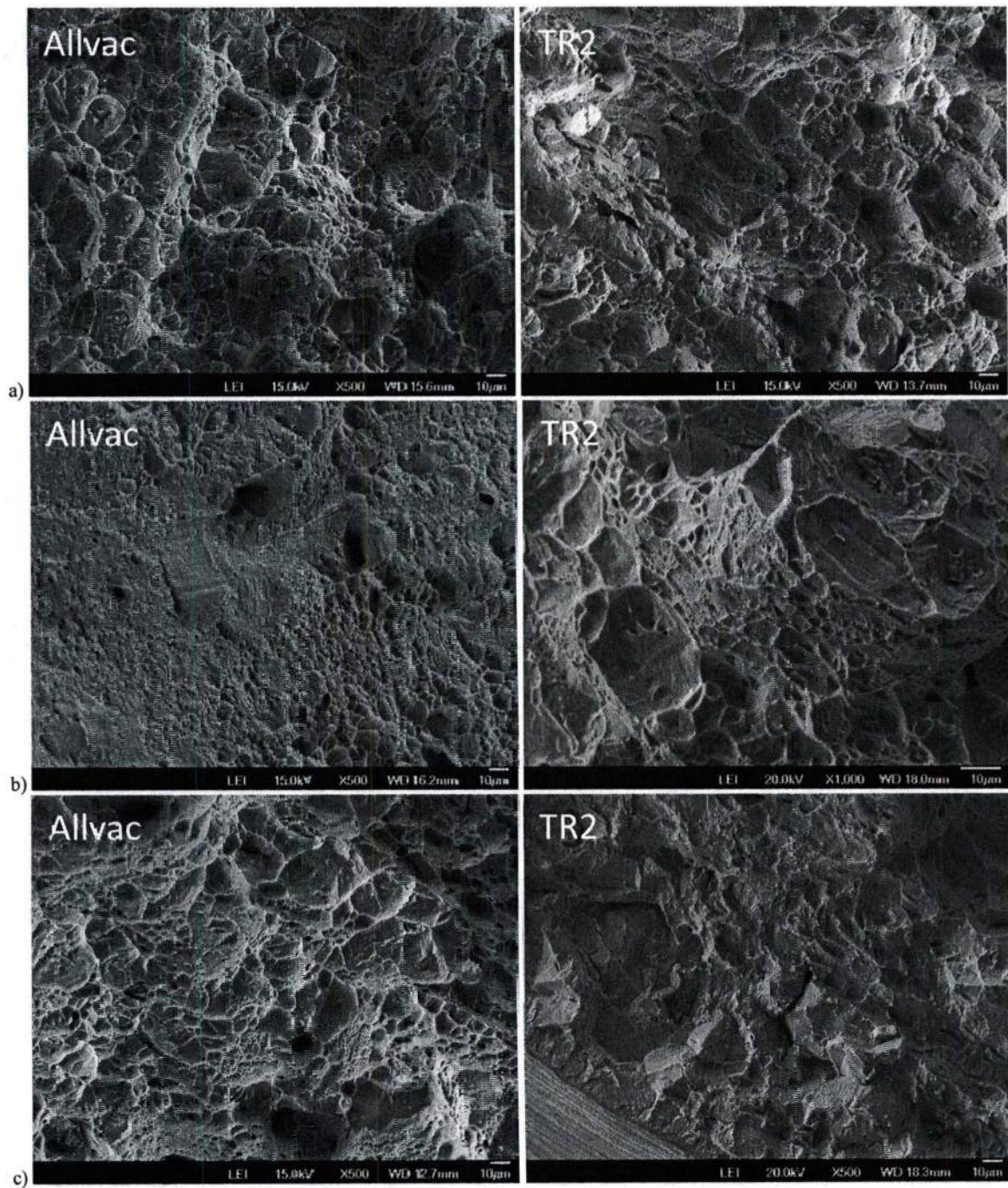


Figure 18. Time to failure of TR2, Allvac, NRL-LS and NRL-HS heats of Monel K-500 during concurrent charging/SSRT test after electrochemical H pre-charging in deaerated 0.6 M NaCl during 48 hours at a constant potential of  $-0.850$ ,  $-0.950$ ,  $-1.0$  and  $-1.1 V_{SCE}$ .





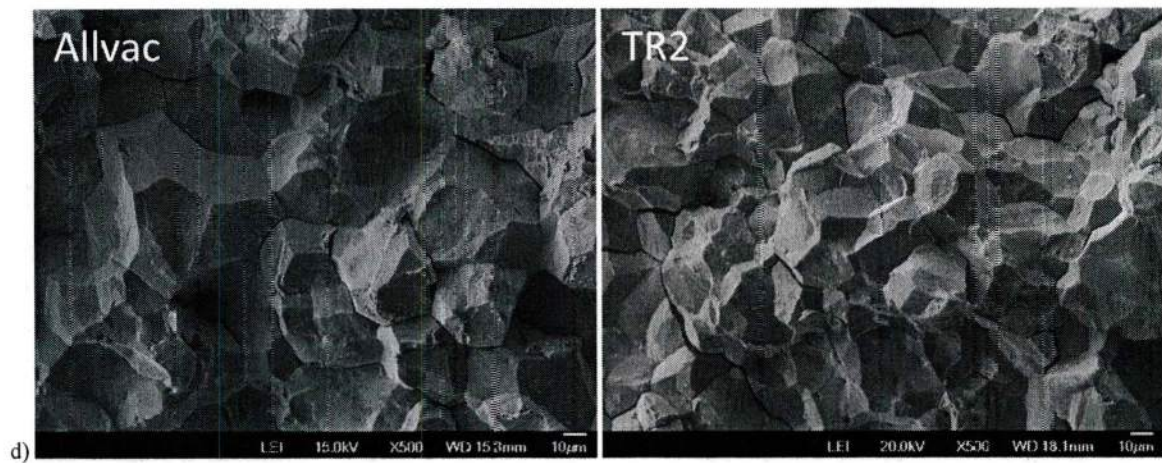


Figure 19. Fractography of TR 2 and Allvac heats of Monel K-500 after concurrent charging/SSRT test running the experiment a) in air and precharging/charging at a constant potential of b)  $-0.850$ , c)  $-0.950$  and d)  $-1.1$   $V_{SCE}$  in deaerated  $0.6$  M NaCl (pH:  $8.0$  by adjustment with NaOH).

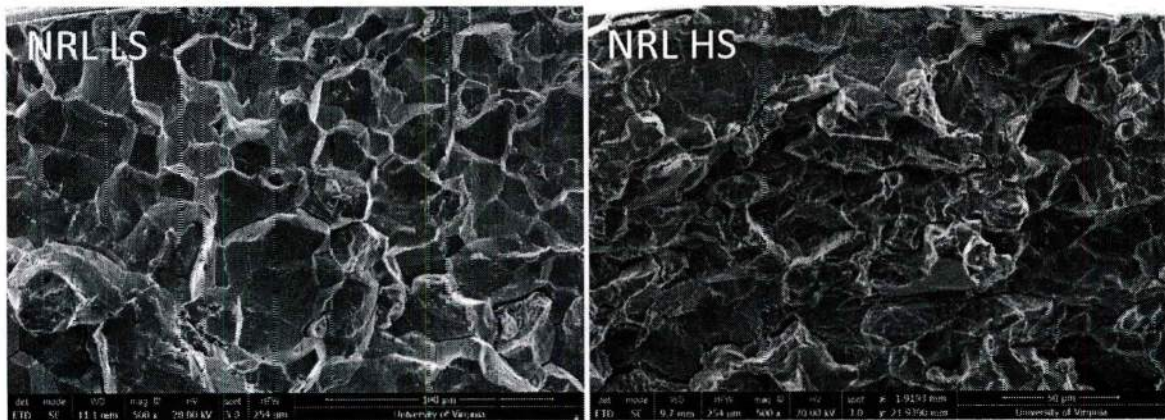
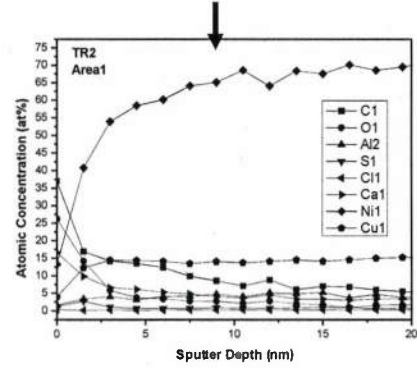
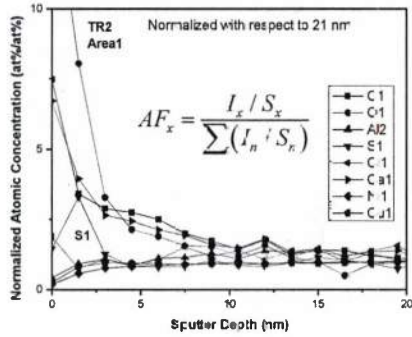
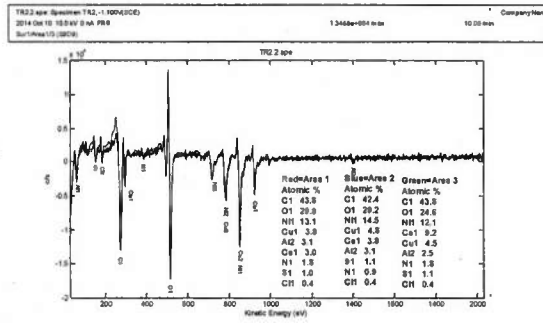
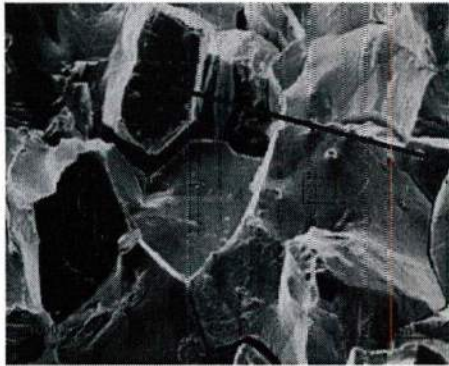
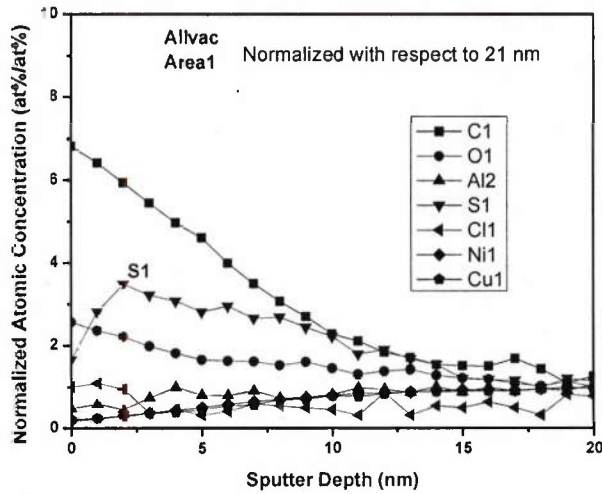


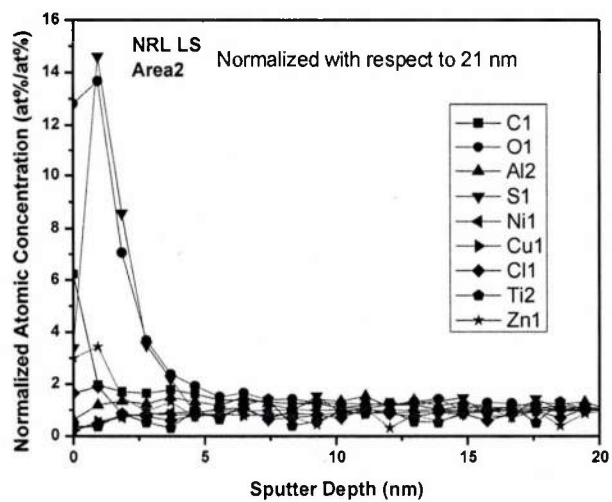
Figure 20. Fractography of NRL LS and HS lots of Monel K-500 after concurrent charging/SSRT test at  $-1.1$   $V_{SCE}$  in deaerated  $0.6$  M NaCl (pH:  $8.0$  by adjustment with NaOH).



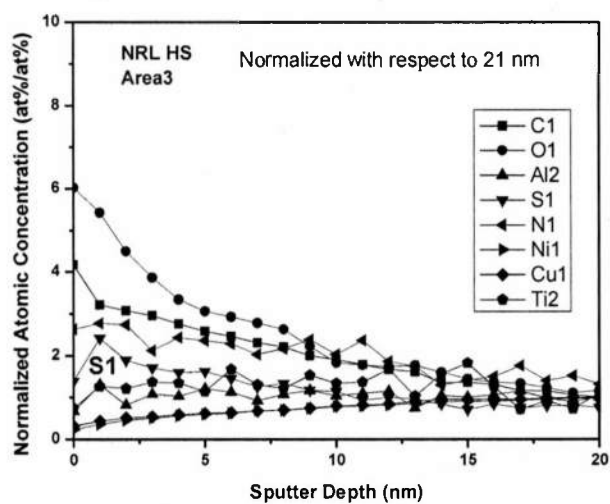
a)



b)



c)



d)

Figure 21. Normalized Auger spectrum on Monel K-500 with respect to signal at a depth of 21 nm from a grain boundary for a) TR 2, including procedure used to make the calculation, b) Allvac, c) NRL LS and d) NRL HS after SSRT performed at a applied potential of  $-1.1 V_{SCE}$  in deaerated 0.6 M NaCl (pH: 8.0 by adjustment with NaOH).

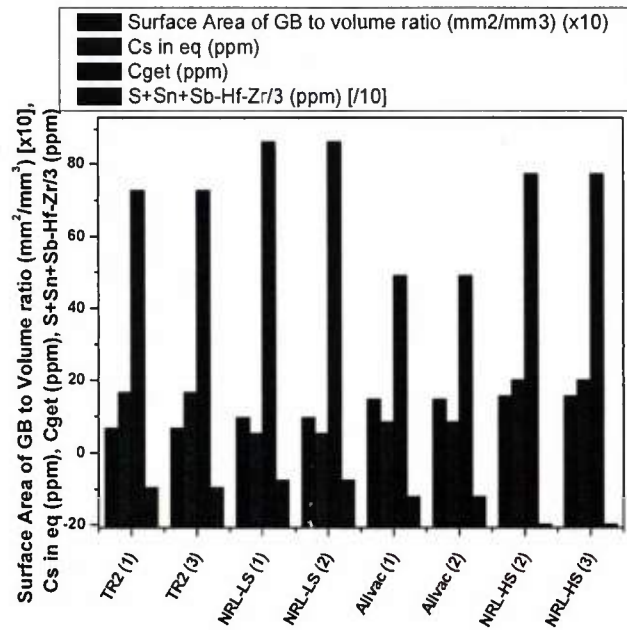
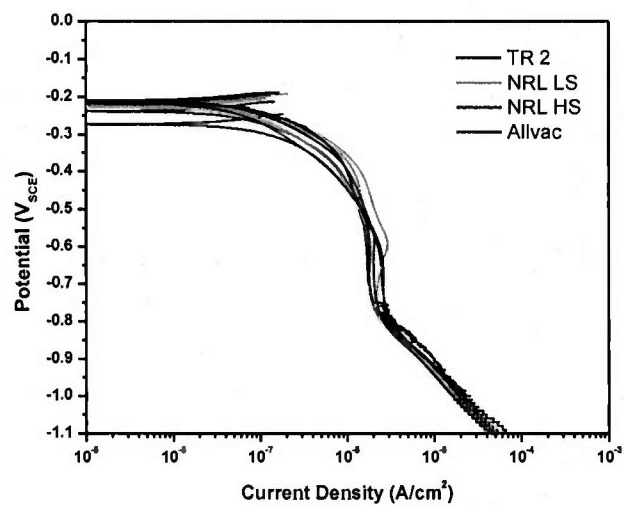
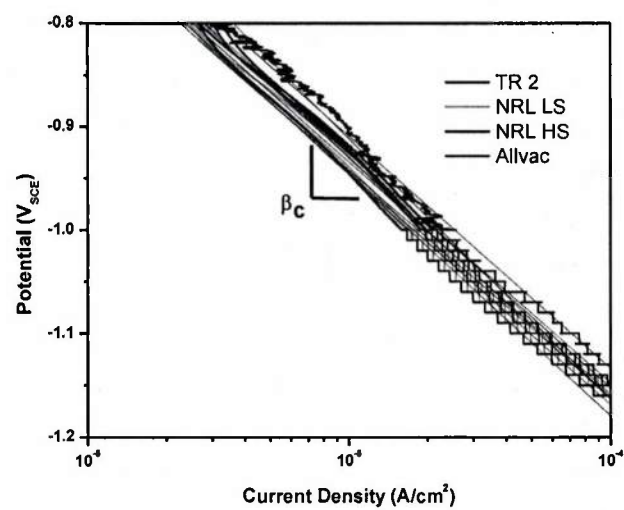


Figure 22. Chemical characterization of Monel K-500 grain boundaries described as surface area of grain boundary to volume ratio; and trace elements content pertaining to the deleterious or enhanced effect of these elements with respect to HE susceptibility. The S+Sn+Sb-Hf-Zr/3 values were TR-2 (-97.0; NRL LS - 76.7; Allvac -121.3; NRL HS -197.9 when expressed in ppm concentrations)





a)



b)

Figure 23. Evaluation of the cathodic kinetics of hydrogen evolution on TR 2 and Allvac *Monel K-500* materials in 0.6 M NaCl (pH 8.00 by adjustment with NaOH).

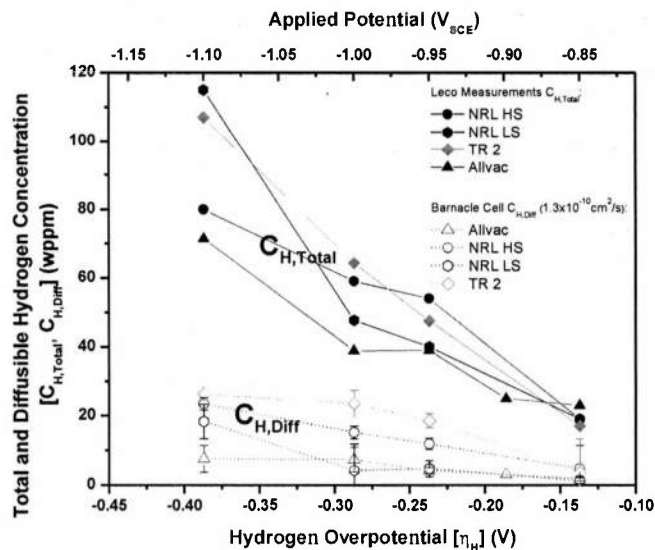


Figure 24. Diffusible and total hydrogen concentrations determined by the electrochemical method, barnacle cell, and thermal desorption spectroscopy, respectively, for the different *Monel K-500* heats after charging in  $V_{SCE}$  in deaerated 0.6 M NaCl (pH: 8.0 by adjustment with NaOH) at -0.850, -0.850, -1.0 and -1.1  $V_{SCE}$  during 7 days (the 95% confidence intervals are shown for the mean diffusible hydrogen concentration values)

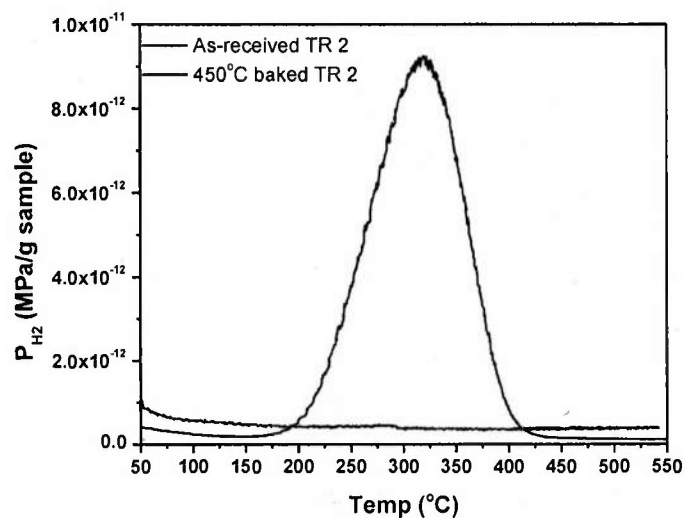
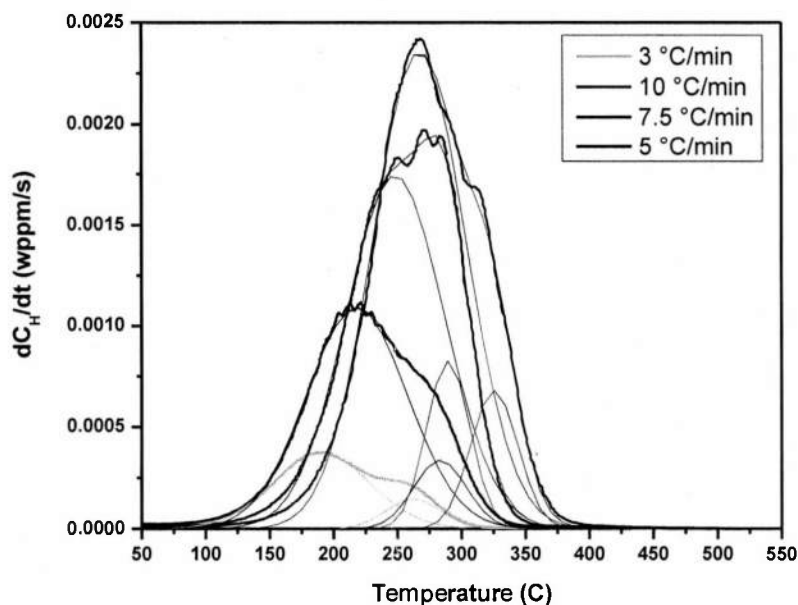
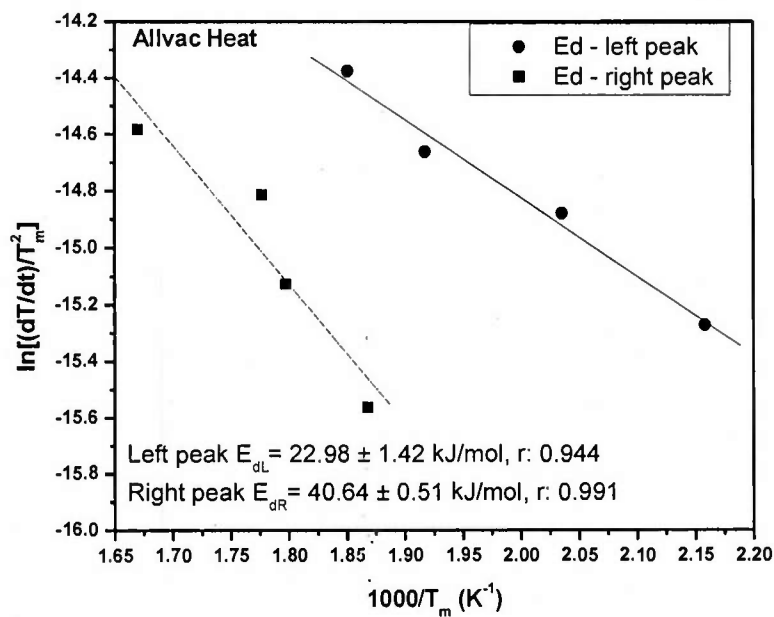


Figure 25. Normalized hydrogen pressure egress for as-received and baked TR 2 *Monel K-500* at 450  $^{\circ}C$ .

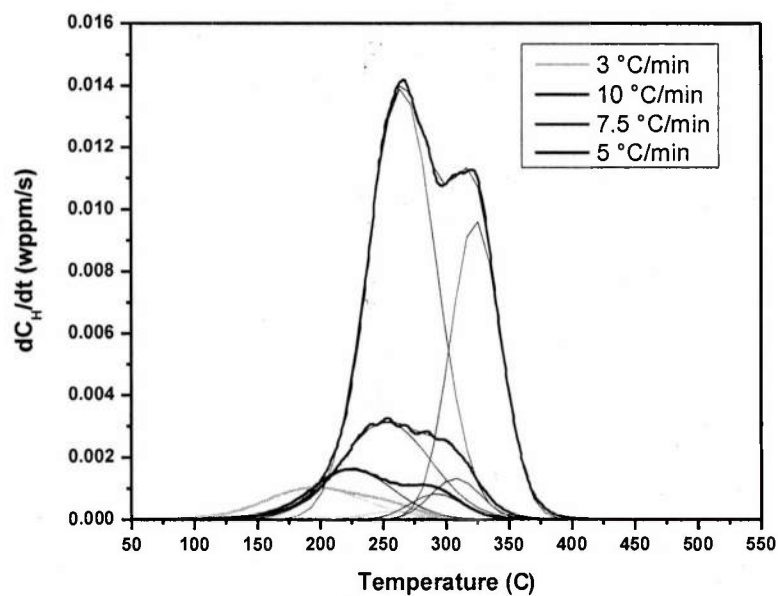


a)

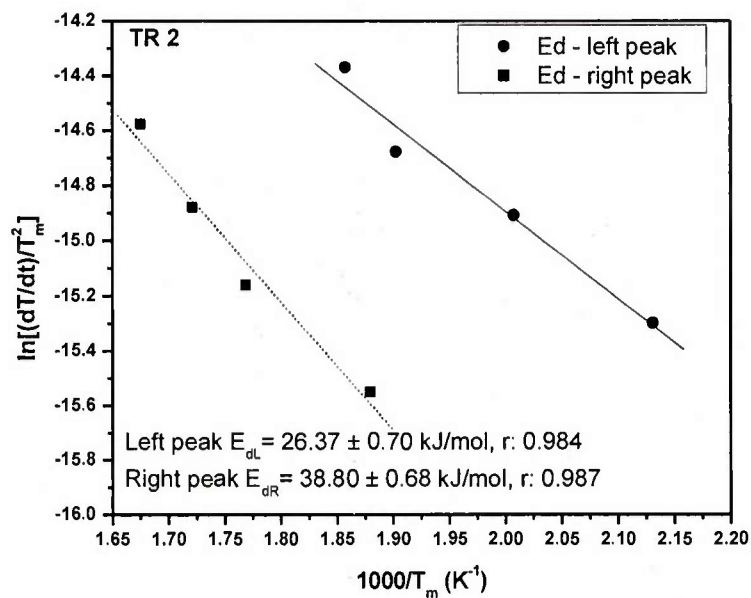


b)

Figure 26. Experimental results extracted from ramped TDS experiments performed at different heating rates on  $120 \mu\text{m} \pm 10 \mu\text{m}$  thick Allvac heat Monel K-500 electrochemically charged with hydrogen in 0.6 M NaCl (pH: 8.0 by adjustment with NaOH) during 7 days applying a potential of  $-1.0 \text{ V}_{\text{SCE}}$ . a) Hydrogen desorption rate ( $dC_H/dt$ ) as a function of temperature and b) calculation of the  $E_d$  for the identified hydrogen desorption peaks and their 95% confidence intervals.



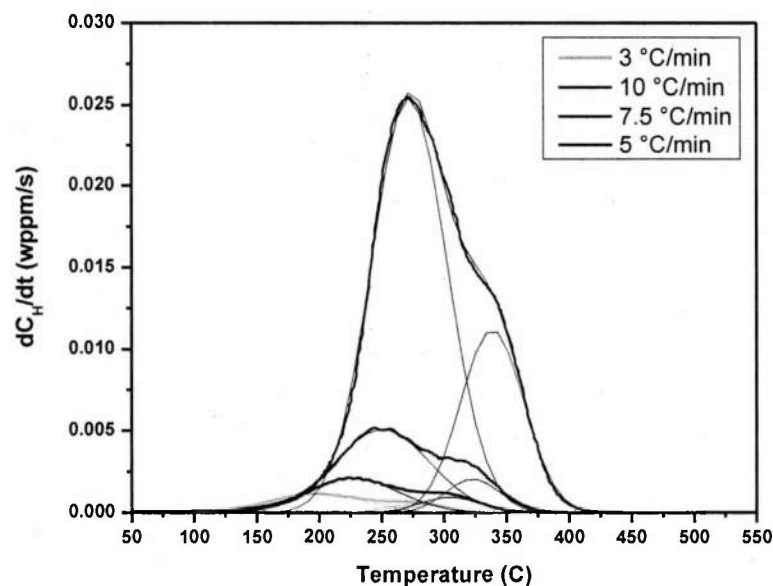
a)



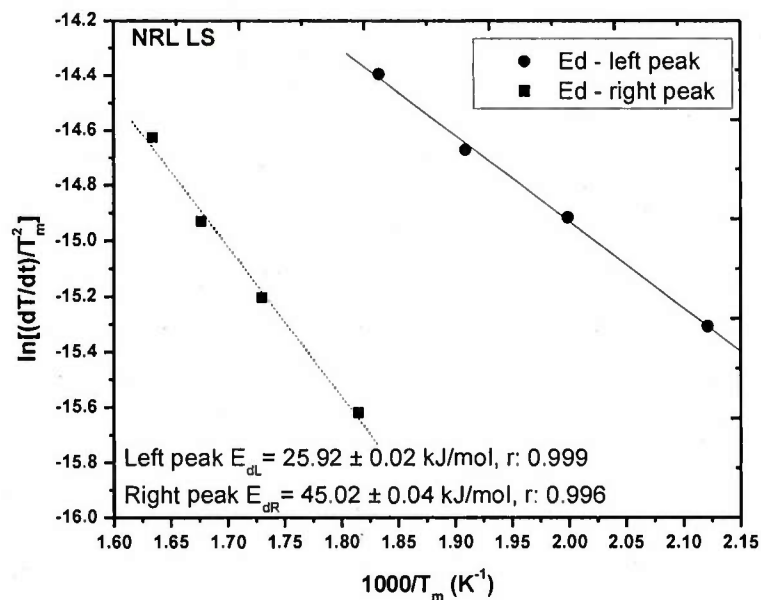
b)

Figure 27. Experimental results extracted from ramped TDS experiments performed at different heating rates on  $120 \mu\text{m} \pm 10 \mu\text{m}$  thick TR 2 heat Monel K-500 electrochemically charged with hydrogen in 0.6 M NaCl (pH: 8.0 by adjustment with NaOH) during 7 days applying a potential of  $-1.0 \text{ V}_{\text{SCE}}$ . a) Hydrogen desorption rate ( $dC_H/dt$ ) as a function of temperature and b) calculation of the  $E_d$  for the identified hydrogen desorption peaks and their 95% confidence intervals.



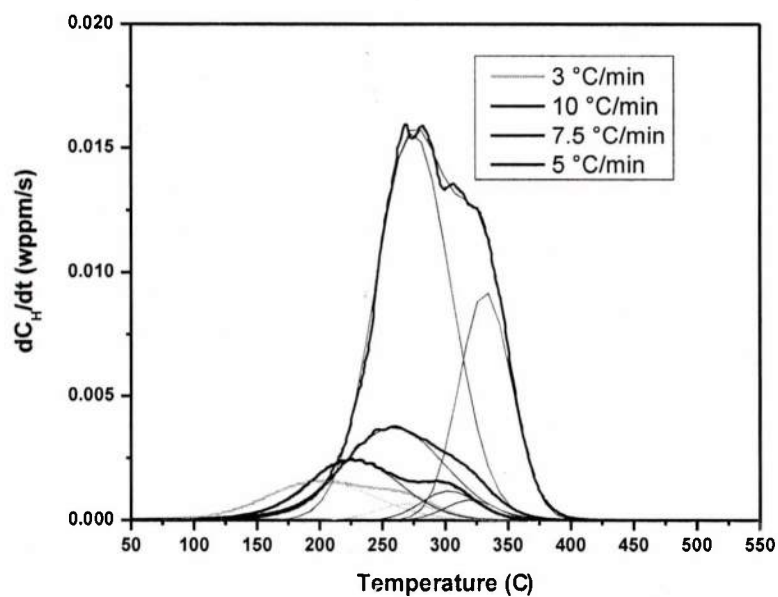


a)

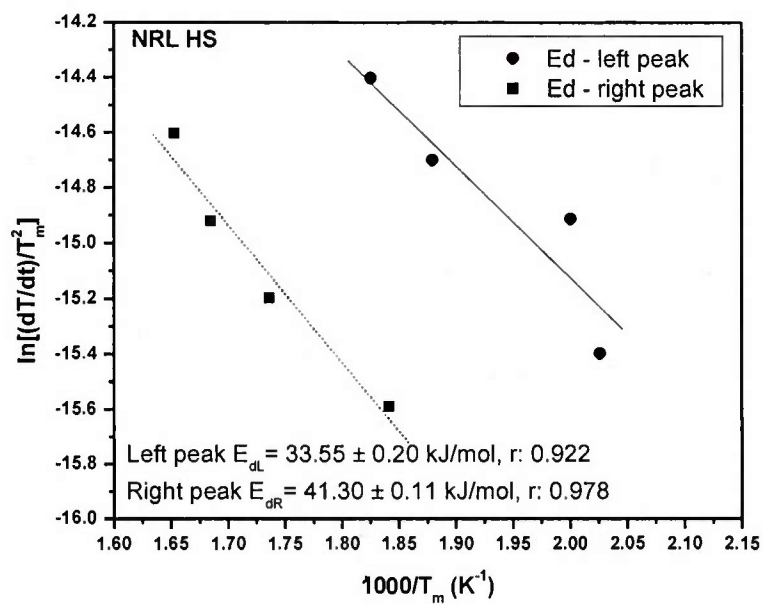


b)

Figure 28. Experimental results extracted from ramped TDS experiments performed at different heating rates on  $120 \mu\text{m} \pm 10 \mu\text{m}$  thick NRL-LS Monel K-500 electrochemically charged with hydrogen in 0.6 M NaCl (pH: 8.0 by adjustment with NaOH) during 7 days applying a potential of  $-1.0 \text{ V}_{\text{SCE}}$ . a) Hydrogen desorption rate ( $dC_{\text{H}}/dt$ ) as a function of temperature and b) calculation of the  $E_{\text{d}}$  for the identified hydrogen desorption peaks and their 95% confidence intervals.



a)



b)

Figure 29. Experimental results extracted from ramped TDS experiments performed at different heating rates on  $120 \mu\text{m} \pm 10 \mu\text{m}$  thick NRL-HS heat Monel K-500 electrochemically charged with hydrogen in 0.6 M NaCl (pH: 8.0 by adjustment with NaOH) during 7 days applying a potential of  $-1.0 \text{ V}_{\text{SCE}}$ . a) Hydrogen desorption rate ( $dC_{\text{H}}/dt$ ) as a function of temperature and b) calculation of the  $E_{\text{d}}$  for the identified hydrogen desorption peaks and their 95% confidence intervals.

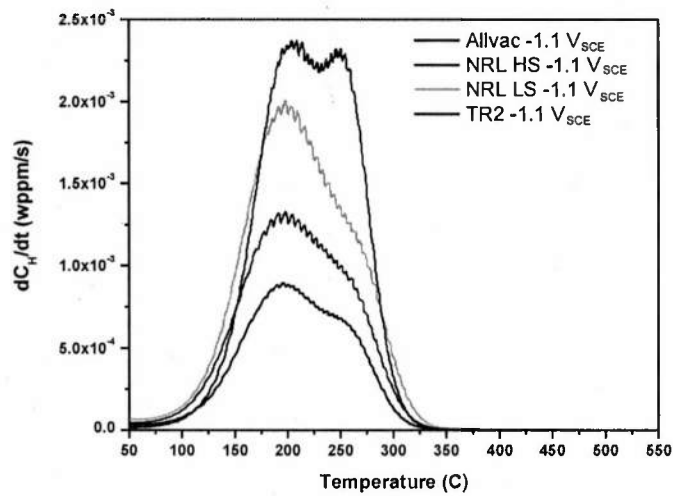


Figure 30. Hydrogen desorption rate ( $dC_H/dt$ ) with respect to temperature calculated from ramped TDS experiments performed on  $120 \mu\text{m} \pm 10 \mu\text{m}$  thick Monel K-500 for the different heats at a heating rate of  $3^\circ\text{C}/\text{min}$ . The flat specimens were electrochemically charged with hydrogen in  $0.6 \text{ M NaCl}$  (pH: 8.0 by adjustment with NaOH) during 7 days at  $-1.1 \text{ V}_{\text{SCE}}$ .

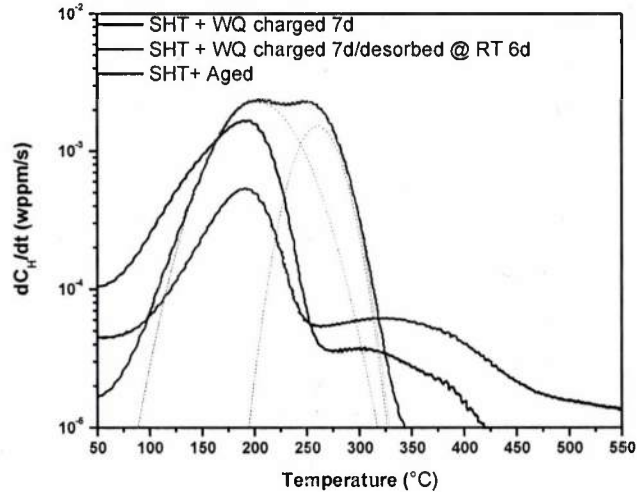


Figure 31. Desorption rate versus temperature obtained utilizing thermal desorption spectroscopy at a heating rate of  $3^\circ\text{C}/\text{min}$  for charged solution heat treated and aged Monel K-500, solution heat treated and water quenched material and solution heat treated and water quenched hydrogen desorbed material. For this last material hydrogen desorption took place at  $25^\circ\text{C}$  during 6 days. The specimens were electrochemically charged with hydrogen in  $0.6 \text{ M NaCl}$  (pH: 8.0 by adjustment with NaOH) during 7 days applying a potential of  $-1.0 \text{ V}_{\text{SCE}}$ . The heat used for these experiments was the TR 2 heat.

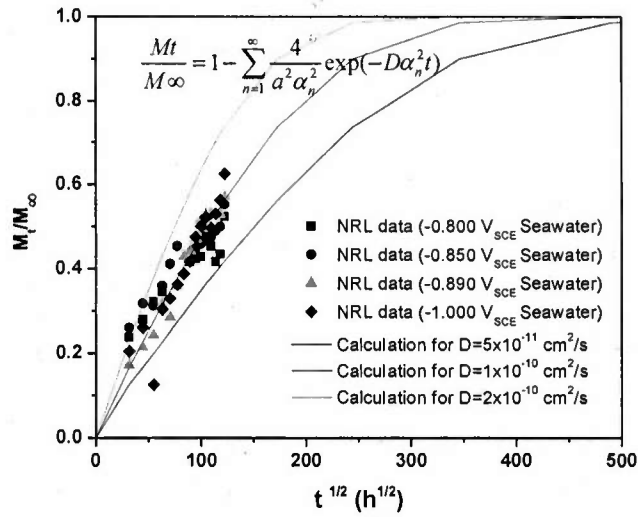


Figure 32. Saturation curve analysis represented in terms of the H mass ratio with respect to a hydrogen saturated state versus the square root of time for NRL heats of Monel K-500. Samples were pre-charged at different time intervals at -0.800, -0.850, -0.890 and -1.000  $V_{SCE}$  in seawater. Theoretical calculations using the solution for a non-steady diffusion model for a cylinder with known initial hydrogen profile was utilized to calculate the saturation curve for hydrogen diffusivities of  $5 \times 10^{-10} \text{ cm}^2/\text{s}$ ,  $1 \times 10^{-10} \text{ cm}^2/\text{s}$  and  $2 \times 10^{-10} \text{ cm}^2/\text{s}$ .

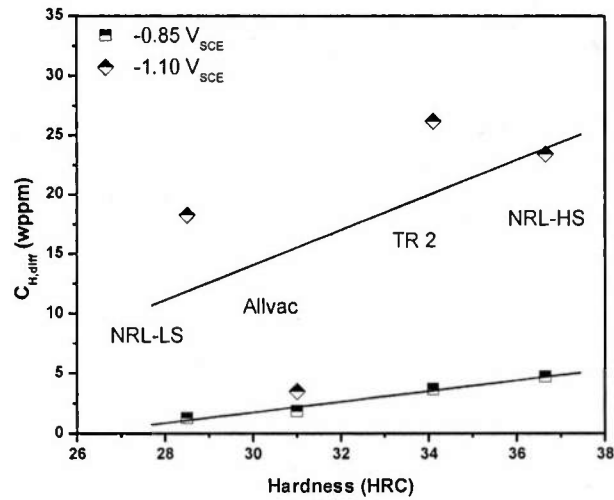


Figure 33. Comparison between diffusible hydrogen concentration of the different heats of Monel K-500 versus hardness of plane sheet specimens electrochemically charged with hydrogen in 0.6 M NaCl (pH: 8.0 by adjustment with NaOH) during 7 days applying a potential of -0.850 and -1.100  $V_{SCE}$ .



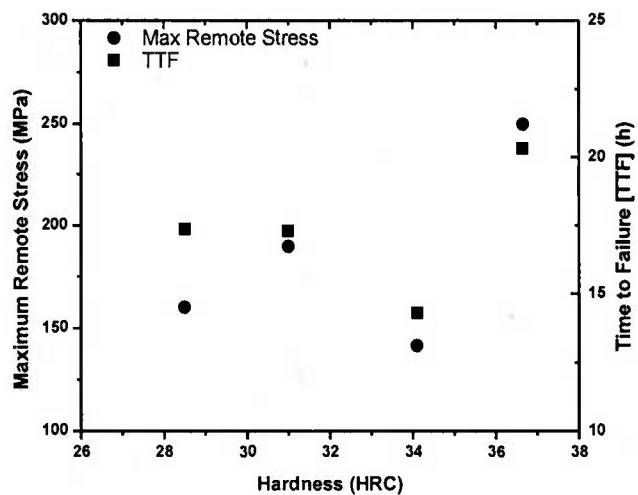


Figure 34. Effect of hardness on the maximum remote stress and time to failure of the different heats Monel K-500 tested during concurrent charging/SSRT test after electrochemical H pre-charging in deaerated 0.6 M NaCl (pH: 8.0 by adjustment with NaOH) during 48 hours at a constant potential of  $-1.1 V_{SCE}$

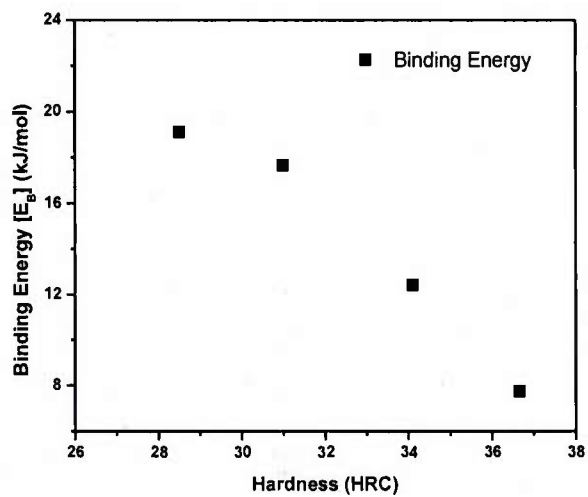


Figure 35. Effect of hardness on the  $\gamma'$  binding energy of the different heats of Monel K-500.

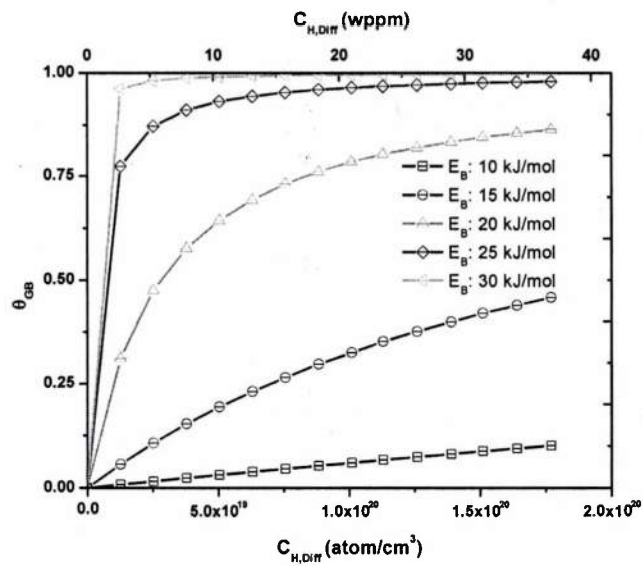


Figure 36. Effect of binding energy and diffusible hydrogen concentration on the theoretical hydrogen coverage on the grain boundaries. The following parameters were assumed for the calculations:  $\rho_{Monel\ K-500}$ : 8.44 g/cm<sup>3</sup>,  $N_{Ni3Al}$ :  $8.29 \times 10^{22}$  sites/cm<sup>3</sup>